SUPERCONDUCTING TUNNELING SPECTROSCOPY OF GRAPHENE AND GRAPHENE NANOSTRUCTURES

BY

YANJING LI

DISSERTATION

Submitted in partial fulfillment of the requirements
for the degree of Doctor of Philosophy in Physics
in the Graduate College of the
University of Illinois at Urbana-Champaign, 2014

Urbana, Illinois

Doctoral Committee:

Associate Professor Smitha Vishveshwara, Chair
Associate Professor Nadya Mason, Director of Research
Professor Stuart Shapiro
Professor Dale J. Van Harlingen

Abstract

This dissertation is concerned with superconducting tunneling spectroscopy of graphene and nanostructures in two dimensional materials. The technique of tunneling spectroscopy via a planar superconducting probe is developed based on a well-formed self-limited tunnel barrier created only between the Pb and the graphene. High magnetic field/low temperature spectroscopy is performed on graphene devices, and manifests energy-dependent features such as scattering resonances and localization behavior. This superconducting tunnel technique is also used to study graphene nanostructures, which can host quantum dot(s) and thus support Andreev bound states (ABS). The fact that ABS are observed only in the narrow (10 nm wide) nano constriction stresses the importance of coupling between the quantum dot and the contact leads for the observation of ABS. The reason why the quantum dot in the narrow constriction has a better coupling to contact leads is likely due to fact that the size of the constriction is smaller than the characteristic length of the potential disorder, which exists in the two dimensional material subject to charge impurities on the substrate. We extend the nanostructure study to another two dimensional material, molybdenum disulfide (MoS_2), where we observe the evolution of the system from a regime of Coulomb blockade to resonant transmission. Our observation could open up new possible applications using nanostructure in these low dimensional materials.

Acknowledgement

This work is supported by the National Science Foundation under DMR-0906521, the Department of Energy under DE-FG02-07ER46453 and DE-FG02-07ER46471, the Department of Physics at the University of Illinois at Urbana-Champaign and is partly carried out in the Materials Research Laboratory Central Facilities.

I would like to thank my advisor, Nadya Mason first for her direction of research. I would like to thank Prof. Norman O. Birge and Prof. Taylor Hughes for their helpful conversations in collaboration. I would like thank my colleagues in our lab: Yung-Fu Chen, Travis Dirks and Nicolas Bronn, for their guide and help when I just started in the lab; Cesar Chialvo, for his support in machining and other lab equipment; Serena Eley, for her help in running fridges. As an experimentalist working closely with the equipment and tools, I have to thank our dedicated staff in Microfab: Tony Banks, Mike Marshall, Shivakumar Bhaskaranand and Tao Shang; Center for Microanalysis of Materials: Scott McLaren, Dougl Jeffers; machine shop: Jim Brownfield and Byron Miller. I am very grateful that I have the luck to work with all these great people who have shared their wisdom and expertise with me. Last but not least, I would like to thank my family: my parents, my grandparents and my husband for their love and support.

Table of Contents

Chapter 1: Introduction

This thesis covers the topic of transport and tunneling in low-dimensional materials having unique electronic properties, specifically, graphene, nanostructures in graphene, and thin layer molybdenum disulfide. To investigate their electronic properties, we develop a technique using a planar superconducting probe to measure the tunneling spectroscopy. This technique is also used on graphene nanostructures to study the conditions under which Andreev bound states can be observed. Lastly, we extend the nanostructure study to molybdenum disulfide, where Coulomb blockade behavior is observed for the first time.

In this chapter, we provide some background information and also a motivation of the materials we have studied, the techniques we have used and developed, and the physics we have observed and will discuss in this thesis.

1.1 The material: graphene (basic electronic properties)

Electron systems in low dimensional materials, in which one or more spatial dimensions are small enough to restrict the quantum mechanical wavefunction of electrons contained inside, exhibit some of the most diverse and intriguing physical phenomena seen in all of condensed matter physics. One low-dimensional material that has received considerable interest since its discovery less than a decade ago is graphene[1-3].

Graphene is a two dimensional material made from a single atomic layer of carbon (Fig 1.1a), with unique electronic properties. It has a relativistic energy spectrum[3,

[4], which makes it a solid state system where quantum electrodynamics phenomena like Klein tunneling[5] can be probed. By applying an external gate voltage, the level of the chemical potential can be tuned to switch the charge carriers between electrons and holes (Fig 1.1b) where the transition point has zero charge carrier density and is called the Dirac point. Graphene has a high mobility and a long mean free path[1], which makes it an attractive material to the semiconducting industry. Due to its two dimensional nature, various techniques can be used to probe it. In addition, graphene nanostructures can be easily created via nano patterning[6] and these nanostructures are stable down to nanometer sizes, thereby providing a versatile platform for studying mesoscopic physics and developing applications utilizing single electrons and molecular electronics.

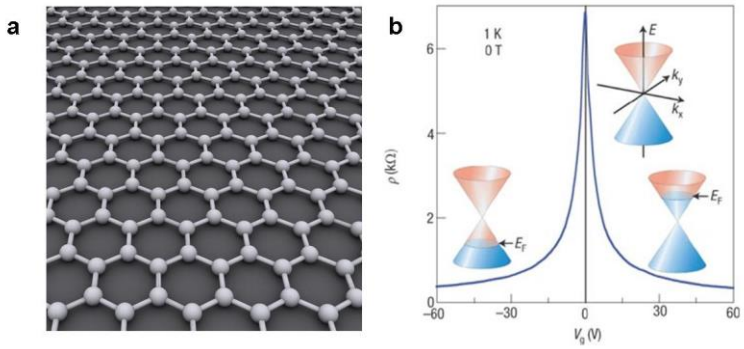

Figure 1.1 (a) A schematic view of graphene lattice structure: an atomic-scale honeycomb lattice made of carbon atoms. (b) The insets show conical low-energy spectrum $E(k)$ of graphene, indicating changes in the position of the Fermi energy E_F with changing gate voltage V_g. Positive (negative) V_g induce electrons (holes) in concentrations $n = \alpha V_g$. Where the peak in resistance (dip in the conductance) is zero carrier concentration point/the Dirac point. The rapid decrease in resistivity ρ on adding charge carriers indicates their high mobility. Adapted from reference[1, 7].

1.2 The technique: tunneling spectroscopy

Tunneling spectroscopy[8] provides a powerful tool for investigating basic electronic properties such as the density of states. Planar tunneling was first realized in

thin film metal-insulator-metal tunnel junctions. Later, scanning tunneling spectroscopy (STS), which provides spatial resolution, was developed and widely used. Compared to the transport measurements performed via Ohmic contacts, which are usually made by direct deposition of metals onto the material, tunneling spectroscopy has advantages: typical end contacts are often invasive and can have variable resistance, for example, materials like graphene can be easily doped by the contact materials. Tunneling spectroscopy is less invasive and allows a direct probe of the energy dependence of the density of states and the distribution function. This can be seen from equation (1), which shows how tunnel conductance depends on the density of states, the distribution function, and the applied bias (energy):

$$\frac{dI}{dV} \propto |T|^2 e^2 N_{M1}(0) \int_{-\infty}^{\infty} N_{M2}(E) \frac{\partial f(E-eV)}{\partial (eV)} dE \qquad (1)$$

where $|T|^2$ is the tunneling matrix element and a reflection of the transmission probability, e is the elementary charge, N_{M1} is the density of states of the metal on one side of the tunnel barrier and N_{M2} is the density of states of the metal on the other side, the Fermi function $f(E) = \frac{1}{\exp(E/k_B T)+1}$ and k_B is the Boltzmann constant.

1.2.1 Basic idea and tunneling from a superconductor

If two conductors are separated by a thin insulator, in the framework of Newtonian mechanics electrons should not able to transfer from one conductor to the other. However, a non-zero probability of charge transfer between the two conductors is possible due to the quantum-mechanical tunneling of electrons. The insulator acts as a tunnel barrier. This probability falls exponentially with the thickness of the insulator

layer and depends on the details of the tunnel barrier, but these can be absorbed in a phenomenological tunneling matrix element $|T|^2$. Electron tunneling can be used to examine the density of states or the distribution function of the material on one side of the tunnel barrier.

If we consider tunneling from a superconductor to a normal metal, the tunnel current and tunnel conductance can be expressed as the following[9]:

Tunnel current $I(V) \propto |T|^2 e^2 N_n(0) \int_{-\infty}^{\infty} N_s(E)[f(E-eV) - f(E)]dE$ (2)*

Tunnel conductance $G(V) \equiv \frac{dI}{dV} \propto |T|^2 e^2 N_n(0) \int_{-\infty}^{\infty} N_s(E) \frac{\partial f(E-eV)}{\partial(eV)} dE$ (3)

here N_n is the density of states of the normal metal and N_s is the density of states of the superconductor.

For $T = 0, \frac{\partial f(E-eV)}{\partial(eV)} = \delta(E-eV) \Rightarrow G(V) \propto N_S(eV)$

For $T > 0, G(V)$ is given as a convolution of superconducting density of states with respect to the derivative of Fermi function. In the low temperature limit, the tunneling conductance at zero temperature $G(V) \propto N_S(eV)$ gives a good estimation. This means that the conductance basically takes the form of the density of states of the superconductor, $N_S(eV)$. In energies only a few millielectronvolts (meV) from the Fermi energy, the density of states based on the Bardeen Cooper Schrieffer theory of

* Here we are only talking about the planar tunneling case. In case of point-contact tunneling where the contact area (junction size) is smaller than the electronic mean free paths, energy dependent quasiparticle scattering happens at the constriction, which will be reflected as the nonlinearities in the current-voltage characteristics. In that case, it is not valid to treat the transmission coefficient/tunneling matrix element as energy independent anymore.

superconductivity can be simply given by $\frac{N_s(E)}{N(0)} = \frac{d\varepsilon}{dE} = \begin{cases} \frac{E}{\left(E^2-\Delta^2\right)^{1/2}} & (E>\Delta) \\ 0 & (E<\Delta) \end{cases}$, where Δ is the energy gap[10].

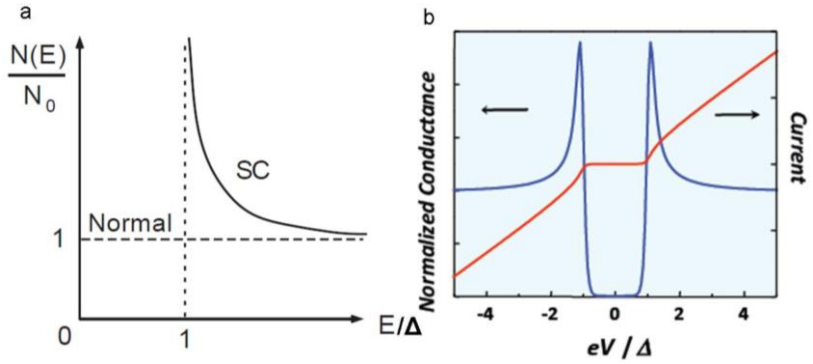

Figure 1.2 (a) Density of states in superconducting compared to normal state, all states whose energies fall in the gap in the normal metal are raised in energy above the gap in the superconducting state. (b) Tunnel current and tunnel conductance through a tunnel junction with one side of the tunnel junction being a superconductor.

A plot of such density of states is shown in Fig 1.2a and the corresponding tunnel current and tunnel conductance is shown in Fig 1.2b. Using a superconducting probe to perform spectroscopy has its advantage: due to the sharp feature in the density of states, the features in the density of `states (or the distribution function) of materials under study can be enhanced in the tunneling spectrum. Another advantage is that by introducing superconductivity, new physics could appear, which we will discuss later.

1.2.2 Experimental realization

As mentioned earlier, experimentally, tunneling spectroscopy[8] can be realized using different methods, planar tunneling and STS. A simple carton picture showing the schematics of planar tunneling and STS is shown in Fig 1.3. These two methods can complement each other. STS allows spatial resolution and causes no damage to the

surface of sample, while planar tunneling has a stable configuration which can be easily fitted into different measurement setups and allows the usage of different materials as the tunneling probe. To introduce superconductivity to the system, we use planar tunneling in our work.

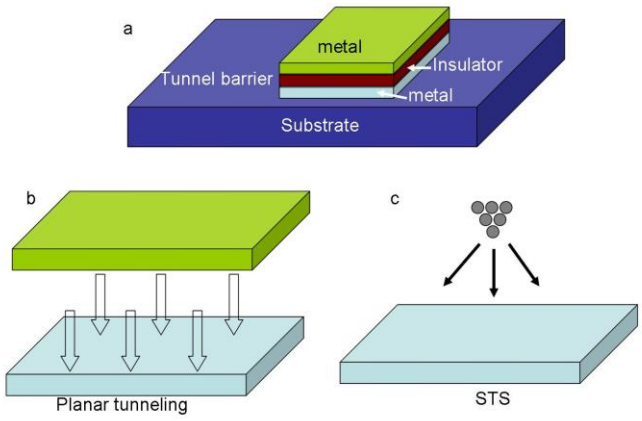

Figure 1.3 (a) Schematic of a planar tunnel junction, which consists of two metals separated by an insulator. Schematic of charge transfer in: (b) planar tunneling (c) STS. Arrows denotes the direction of charge transfer.

1.3 Tunneling spectroscopy of graphene

1.3.1 STS of graphene and the disorder potential

STS study of graphene has been very fruitful. For example, spatial charge inhomogeneity[11, 12], edge states[13, 14], and phonon induced behavior[15] have been demonstrated. The work described in this thesis is most relevant to previous STS studies which reveal how the local electronic properties of graphene[16] in zero magnetic field are affected by charged impurities and structural disorder[7, 11, 17, 18].

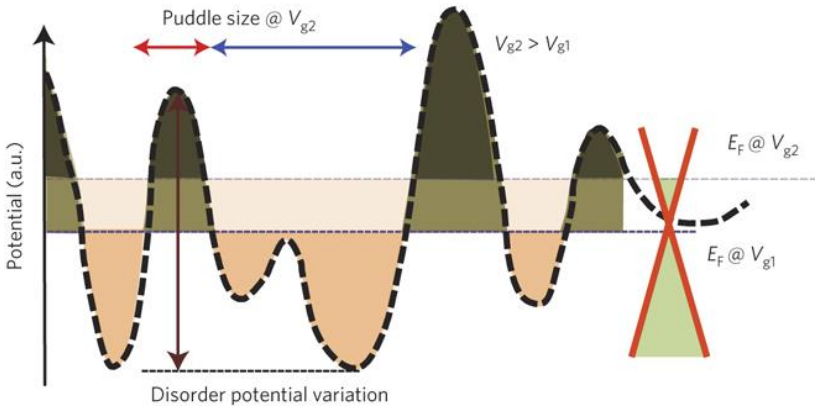

Figure 1.4 Schematic diagram of the disorder potential variation as a function of spatial location. The relative position of the Fermi energy to the Dirac point can be tuned by an electrostatic potential from a back gate. Adapted from Fig. 1c of reference[7].

In an ideal graphene layer, the carrier density can be continuously tuned from hole to electron doping through zero density (the Dirac point). However, as illustrated in Fig 1.4, the relative position of the local Dirac point with respect to the Fermi level is changed by a spatially varying electrostatic potential induced by local disorder. The dominant cause of this local disorder is charge impurities on the substrate (both intrinsic and extrinsic); this can be minimized by putting the graphene on top of a thin layer of hexagonal boron nitride[19]. However, for the results in this thesis we measured graphene on amorphous SiO_2, where the surface charges leads to strong potential variations. For these samples, if the Fermi level is close to the Dirac point, then spatially alternating patterns of electron and hole puddles are formed. These puddles, created by the variation of this local electrostatic potential, can affect many of properties of graphene; for example, it has been considered as one of the main sources of the measured minimum conductivity in macroscopic graphene devices[4]. Later we will see how this disorder potential plays an important role in studying nanostructures in both graphene and MoS_2.

1.3.2 STS of graphene in magnetic field and Landau Levels

In a two-dimensional electron system in the presence of a magnetic field, *B*, the energy for motion perpendicular to the field is quantized in a series of equally spaced Landau Levels:

$$E_n = E_{\pm} \pm \hbar\omega_c\left(n+1/2\right),\ n=0,1,2,... \quad (4)$$

where $\hbar$ is Planck's constant, $\omega_c = eB/m^*$ the cyclotron frequency and e the electron charge. Landau levels[20-27] in graphene have been observed in STS[28] studies (Fig 1.5). Instead of the usual linear dependence, due to the relativistic nature of massless Dirac fermions, the Landau level energy sequence in single layer graphene consists of a field-independent state at zero energy followed by a sequence of levels with square-root dependence in both field and level index:

$$E_n = \mathrm{sgn}\left(n\right)\sqrt{2e\hbar v_F{}^2\left|n\right|B}\ ,\ n=...-2,-1,0,1,2,... \qquad (5)$$

Here the energy is measured relative to the Dirac point energy. When two graphene layers stack to form a bilayer, the interlayer coupling leads to the appearance of band mass but it does not open a gap at the Dirac point. Here the Landau Level spectrum takes the form $E_n = \pm\hbar\omega_c\sqrt{n\left(n-1\right)},\ n=0,1,2,...$ This sequence is linear in field, similar to the standard case. An alternative form is:

$$E_n = \mathrm{sgn}\left(n\right)\hbar\omega_c\sqrt{\left|n\right|\left(\left|n\right|+1\right)},\ n=...-2,-1,0,1,2,... \qquad (6)$$

This form gives the same Landau Level spectrum, including the double degeneracy of the zero-energy level.

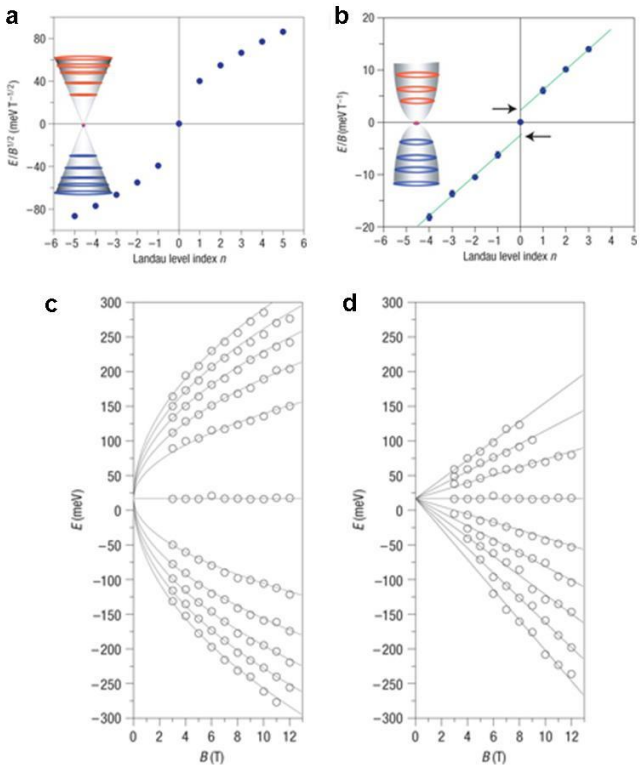

Figure 1.5 Landau levels in single layer and bilayer graphene. (a) Scaled energy of the aligned peaks plotted against Landau Level index. Inset: Landau-level energy sequence of massless Dirac Fermions superposed on the Dirac cone. (b) Scaled energy plotted against Landau Level index. Solid lines represent the Landau Level spectrum expected for normal massive fermions. The arrows show two missing n=0 levels. Inset: Landau-level energy sequence of massive Dirac Fermions superposed on the zero-field dispersion. (c) Massless Dirac Fermions. Solid lines represent fits of the spectra with equation (5). (d) Massive Dirac Fermions. Solid lines represent fits of the spectra with equation (6). Adapted from reference[28].

1.3.3 Planar tunneling into graphene via a superconductor

Planar tunneling enables the study of graphene spectroscopy at ultra-low temperatures, high magnetic fields, and high gate voltages, as well as usage of various materials as the probe. Tunneling spectroscopy of graphene at ultra-low temperature and high magnetic fields[29] has been demonstrated only rarely in STS experiments[21], and these experiments did not include a gate voltage. There have been a limited number of experiments using Cu or Al planar tunnel probes on graphene, but these probes have

generally been low-yield and/or unreliable[30]. When a superconducting planar tunnel probe is combined with graphene or graphene nanostructures, different interesting physics can emerge, such as the superconducting proximity effect[31] and Andreev bound states (ABS)[32]. These effects could be relevant for applications such as single electron transistors[33], superconducting or normal transistors[1, 34], and quantum information processing such as ABS-based qubits[35, 36]. Using a Pb planar tunnel probe to perform tunnel spectroscopy, we not only provide a new technique to study the novel electronic properties of graphene, but also introduce superconductivity into the picture and thus allow the interplay between superconductivity and graphene.

1.4 The physics: Andreev bound states

1.4.1 Andreev reflection

An interesting phenomenon introduced by superconductivity to the interface between a superconductor and a metal is Andreev reflection (Fig 1.6a). As we discussed in the previous section, there is no quasiparticle state inside the superconducting energy gap and thus single particle tunneling is not allowed in the transport through a tunnel junction between a superconductor and a normal metal. However, a process that transforms an electron into a hole that retraces the path of an incoming particle can happen and allow charge transfer within the energy gap. This process is called Andreev reflection[37, 38], which determines the conductance of the interface at voltages below the superconducting gap. A theory that is usually referred to as BTK (Blonder, Tinkham and Klapwijk)[39] gives a theoretical description of the conductance of such system using a single parameter, the effective barrier strength. This parameter plays a very important

role: if the barrier strength is strong, the probability of Andreev reflection is small and the conductance inside the superconducting gap is suppressed; if the barrier is not that strong, Andreev reflection can happen and the conductance inside the gap can be non-zero.

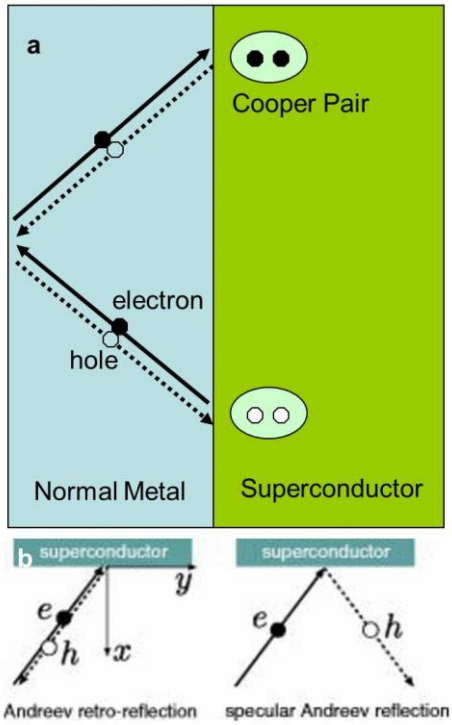

Figure 1.6 Andreev reflection and Andreev bound states. (a) An example of the quasiparticle path corresponding to the Andreev reflections, giving a bound state. The quasiparticle is trapped in the normal region because of normal reflection at the normal metal surface and the Andreev reflection at the normal metal/superconductor interface. The solid lines denote the trajectories of the electrons, and the dashed lines denote the trajectories of the holes. (b) Andreev retroreflection (left panel) at the interface between a normal metal and a superconductor. Arrows indicate the direction of the velocity, and solid or dashed lines distinguish whether the particle is a negatively charged electron *e* or a positively charged hole *h*. Specular Andreev reflection (right panel) at the interface between undoped graphene and a superconductor. Adapted from reference[5].

If the normal metal is graphene, specular Andreev reflection[40] can happen if an electron in the conduction band is converted into a hole in the valence band, where the Andreev reflected hole is not going in the opposite direction as the original incident electron. In the usual case when the electron and hole both lie in the conduction band,

Andreev reflection is still retroreflection. A schematic showing both cases is shown in Fig 1.6b.

1.4.2 Andreev bound states

Due to the Andreev reflections, according to which an incident electron is reflected back as a hole at the interface and a Cooper pair is created in superconductor, Andreev bound states[41, 42] could emerge in the normal metal/superconductor structures. These appear if the normal metal has a geometry confinement, where the electron (hole) reflected back by the Andreev reflection at the interface of superconductor-normal metal can be reflected again by the confinement barrier. In this case, the reflected electron (hole) can form bound states, which are closed trajectories composed of Andreev reflections and regular reflections. Such states are built up from a combination of electron and hole wave functions. The example of the closed quasiparticle trajectory, producing the bound state, in a normal metal/superconductor, is shown in Fig. 1.6a. It consists of an electron segment, which includes an ordinary reflection at the edge of the normal metal, and a hole one, retracing backwards the electron trajectory. ABS are interesting as a fundamental physics phenomenon but could also have application such as qubit[36] in quantum computation.

1.4.3 Observation of Andreev bound states

Geometry confinement is necessary for the observation of ABS, as discussed in the previous section. This can be realized in a Josephson junction, where ABS are formed from the multiple Andreev reflection at the two normal metal-superconductor interfaces. Quasi particles nucleate at the surface of a *d*-wave superconductors could form ABS[9].

Quantum dot systems could also provide the geometric confinement. ABS has been observed in superconductor-graphene quantum dot hybrid systems[32]. In superconductor-graphene-superconductor systems, proximity effect[31], multiple Andreev reflection[43], phase diffusion[44], and ballistic supercurrent[45] have been observed as expected for a Josephson junction while ABS have not been reported so far.

Another necessary element to observe ABS is Andreev reflection, which requires relatively good coupling between the normal metal and the superconductor (or rather, the system should not be in the strong tunneling regime, where the Andreev reflection will be suppressed). Historically, there have been technical difficulties to increase the coupling between a superconductor and conventional semiconductors for material reasons, for instance, oxidation of the interface. New materials introduced recently, such as carbon nanotubes[46, 47], semiconducting nanowires[48, 49] and self-assembled quantum dots[50] make the regimes of intermediate and strong coupling more accessible.

In our studies, we introduce graphene nanostructure which can supply the geometry confinement. We also show that the combination of graphene and the superconductor, Pb could give rise to an interface tunable from the low barrier regime to the strong tunnel regime, which allows the observation of ABS.

1.5 Beyond graphene

We extend our studies from graphene to nanostructures in graphene and in another two dimensional material, molybdenum disulfide (MoS_2). We refer to nanostructures as objects of intermediate size, between microscopic and molecular structures. As we mentioned earlier, graphene can be easily patterned into nanostructures

such as nanoribbons and nano-constrictions. In these graphene nanostructures[51, 52], quantum dot behavior has been observed[6, 33, 53-58].

1.5.1 Coulomb blockade and Fabry-Perot oscillations

A quantum dot is a nanocrystal made of semiconductor materials that are small enough to exhibit quantum mechanical properties. It constitutes a basic unit for many useful applications such as transistors, solar cells, LEDs, and diode lasers. It has also been investigated as possible qubits in quantum computing[59-61].

The quantum dot confines electrons in an isolated island where the geometry confinement can make the energy spacing between discrete energy levels significant and observable. In addition, transferring electrons from the leads to the island requires a charging energy, which depends on the capacitance of the island. A bias voltage can supply the energy needed to conquer the charging energy so that electron transfer can happen with a certain amount of bias applied across the source and drain leads coupled to the quantum dot. The substrate which supports the quantum dot serves as the backgate, which is usually Si with a SiO_2 layer as the dielectric media for the capacitor. A voltage applied on the backgate can also adjust the discrete energy levels in the quantum dot so that it can align with source/drain potential at certain point to allow electron transferring. This results in a signature behavior of a closed quantum dot, Coulomb blockade, which is evident by the periodic peaks in the backgate characteristic of the conductance and the Coulomb diamonds in the two dimensional map of conductance as a function of bias and backgate voltage (Fig 1.7d, 1.7e).

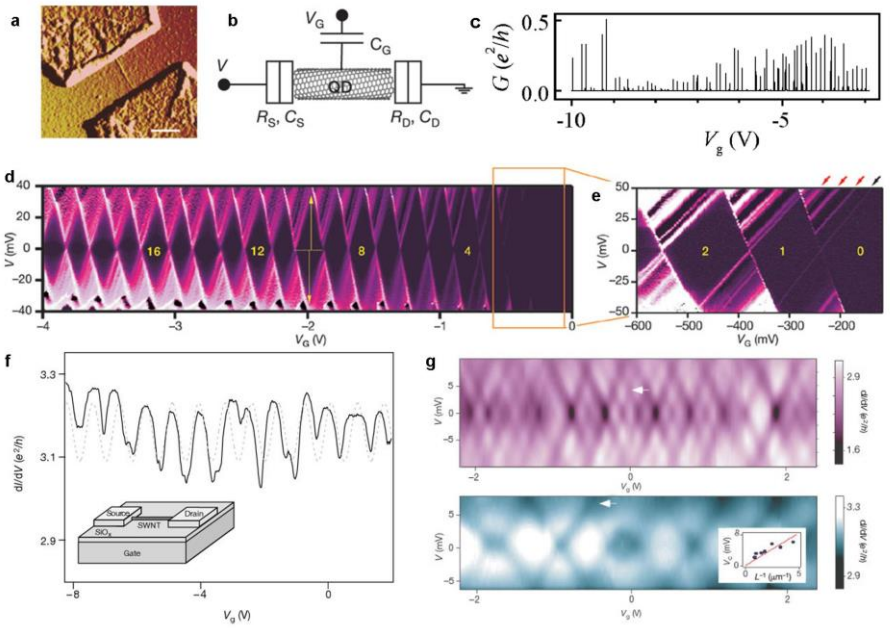

Figure 1.7 Coulomb blockade and Fabry-Perot oscillations in carbon nanotube devices. (a) Atomic force microscope (AFM) image of the device (scale bar, 200 nm). (b) Device scheme. (c) Conductance vs. gate voltage for a nanotube quantum dot (length between the contacts, L ~ 300 nm) at 0.3K. (d) Two-dimensional colour plot of the differential conductance, dI/dV, versus V and negative V_G at T = 4 K (black is zero, white is 3 μS). In the black diamond-shaped regions, the number of holes (indicated) is fixed by Coulomb blockade. (e) Zoom-in, taken at 0.3 K of the region with 0, 1 and 2 holes (white represents dI/dV > 10 nS). Lines outside the diamonds running parallel to the edges correspond to discrete energy excitations (the black arrow points at the one-electron ground state; the red arrows at the one-electron excited states). (f) The dotted curve shows a sinusoidal function with the same average period as the measured data (solid). Inset, a schematic diagram of the device. (g) Upper: data from a 530 nm nanotube device; lower: data from a 220 nm nanotube device. Both plots show a quasi-periodic pattern of crisscrossing dark lines that correspond to the dI/dV dips as V and V_g are varied. The bias voltage values (V_c) at which adjacent positively and negatively sloped lines intersect (white arrows) quantify the energy scales for dI/dV oscillations. Inset, values of V_c from seven devices plotted against the inverse nanotube length (L^{-1}). The solid curve is a line with a slope equal to $hv_F/2$ = 1,670 meV nm^{-1}, where v_F = 8.1×105 m s^{-1} is the Fermi velocity in the nanotube. Adapted from reference[62-64].

Here we use carbon nanotube as an experimental example to illustrate Coulomb blockade and Fabry-Perot oscillations. A carbon nanotube is essentially a one dimensional quantum wire and if a section of nanotube is contacted by metals, a quantum dot can form due to confinement defined by the contacts. The nanotube quantum dot is

connected to source and drain electrodes by tunnel barriers characterized by resistances R_S, R_D and capacitances C_S, C_D. The backgate is represented by a capacitor C_G (Fig 1.7 b). The source–drain current, I, (or differential conductance dI/dV) is recorded in the measurements as a function of source–drain voltage V and gate voltage V_G. When the coupling between the contacts and nanotube is nearly Ohmic as compared to the strong tunnel barrier regime, the transport behavior will be dominated by Fabry-Perot oscillations instead of Coulomb blockade (Fig 1.7g, 1.7f). The crossing oscillation characteristics come from the interfacial electron scattering coupled with ballistic electron transport within the nanotube and may be determined by quantum interference between electron waves multiply reflected between two nanotube–metal interfaces, analogous to the light transmission in an optical Fabry–Perot cavity. Besides contact transparency, ballistic transport is also necessary for Fabry-Perot oscillations to be observed.

1.5.2 Nanostructures in graphene

An example showing Coulomb diamonds observed in graphene nanoribbons can be seen in Fig 1.8b. Graphene nanostructures have been proposed to be a good candidate for transistor application[1] with the geometry induced confinement gap[65, 66]. Experimentally a transport gap is indeed observed in graphene nanoribbons and constrictions. However, it also has been found that charging energy coming from the quantum dot dominates in the transport[67, 68]. The quantum dot could come from the rough edge[67-69], created by the reactive ion etching; another possibility is that the disordered potential induced by the impurities on the substrate surface[68, 70]. A cartoon picture explaining the disorder potential mechanism is shown in Fig 1.8a. The problem of

the main contribution to quantum dot formation is still not solved, which may impede the further implementation of the quantum dot in the graphene nanostructure; however, such devices still provide a useful platform for studying disorder.

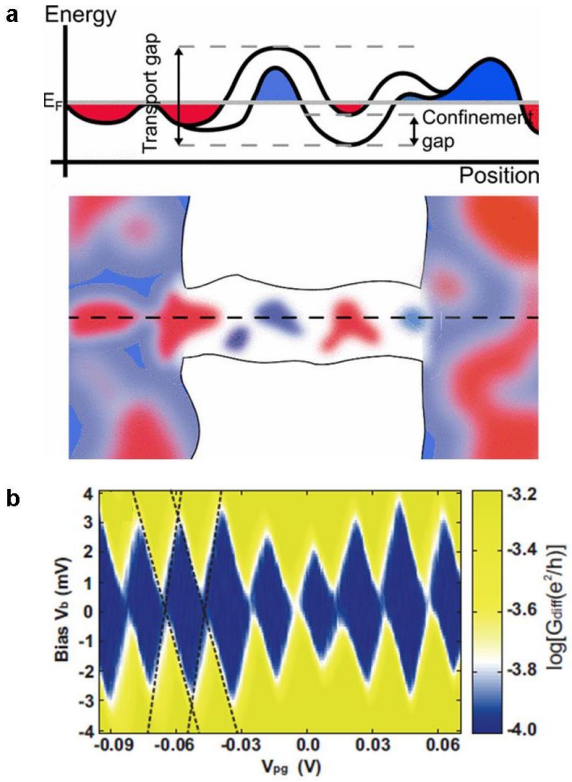

Figure 1.8 Quantum dot behavior in graphene nanostructure. (a) Cartoon of quantum dots forming along the ribbon due to potential inhomogeneities and a confinement gap. The red (dark gray) puddles indicate electrons and the blue (light gray) puddles indicate holes. The thick dark curves on the top diagram depict the energies of the bottom of the conduction band and the top of the valence band as a function of position along the dashed line on the cartoon below. The curve splits into two inside the ribbon because of the confinement gap. The transport gap can be identified as the amplitude of the disorder plus the confinement gap. (b) Differential conductance vs. backgate voltage and bias of a graphene nano-constriction about 0.06 μm^2, showing Coulomb blockade behavior suggesting the presence of a quantum dot. Adapted from reference[33, 57, 70].

1.5.3 Molybdenum disulfide

Graphene has renewed interest in other inorganic, two-dimensional materials with unique electronic and optical attributes, for example, MoS_2. Similar to graphene, MoS_2, as shown in Fig 1.9a, has a layered structure, wherein molybdenum atoms are sandwiched between layers of sulfur atoms. The weak van der Waals interactions between the sheets of sulfide atoms results in the property that it can be easily exfoliated into single layer. Bulk MoS_2 is a diamagnetic, indirect bandgap semiconductor similar to silicon, with a gap of 1.2 eV. Single layers MoS_2 has a bandgaps[71] that change from indirect to direct, allowing applications such as transistors[72], photodetectors[73] and electroluminescent devices[74]. Both monolayer and bilayer MoS_2[75, 76] have a sizable energy gap[71] as shown in Fig 1.9b. Although MoS_2 has been widely studied for decades, its role as a near-atomically thin material is new. The recent advances in nanoscale materials characterization and device fabrication facilitate the study of nanostructures in thin layers of MoS_2. Devices based on thin layers of MoS_2 have demonstrated strong photoluminescence[77], a current on/off ratio exceeding 10^8 in field-effect transistors (FETs)[78], and efficient valley and spin control by optical helicity[79]. However, little has been explored in nanostructures made from thin layer of MoS_2. It is natural to ask the question whether quantum dots exist in the MoS_2 nanostructures just like in its graphene counterparts, since nanostructures could introduce confinement effect. The transport studies of nanostructures may help answer the following questions as well: could Coulomb blockade behavior coexist with the large band gap? Could resonant transmission happen despite the short mean free path?

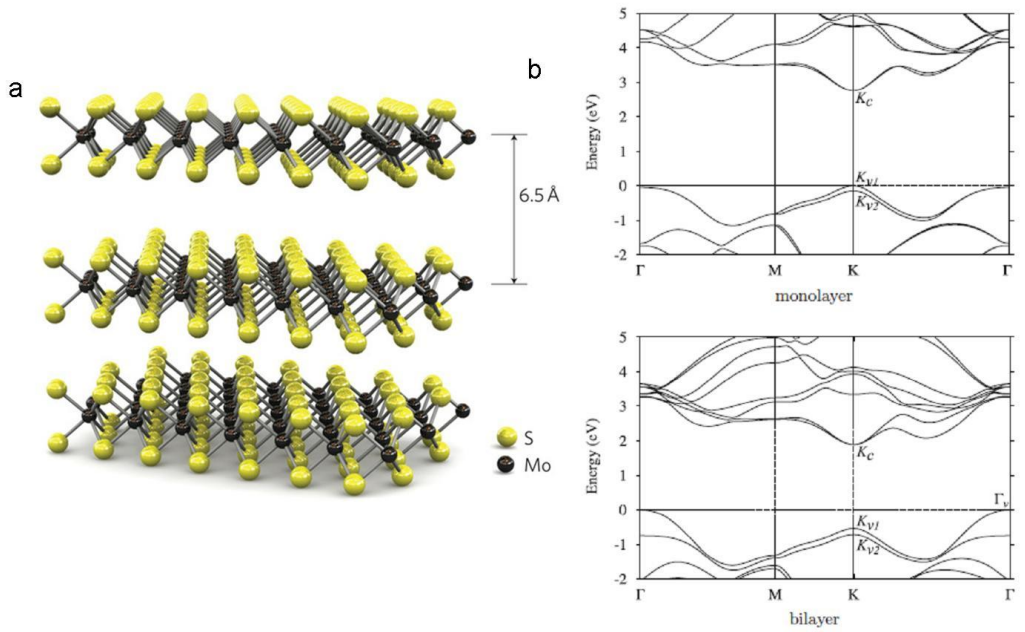

Figure 1.9 Lattice structure and band structure of thin layer MoS_2. (a) Three-dimensional representation of the structure of MoS_2. Single layers, 6.5 Å thick, can be extracted using scotch tape-based micromechanical cleavage. (b) Band structure of a single layer and bilayer MoS_2. Adapted from reference[71, 72].

1.6 Outline of this thesis

We have introduced the materials, the techniques and the physics we are interested in studying in this thesis. Next we will discuss them in details: the superconducting planar tunneling technique (chapter 2), the tunneling spectroscopy performed on graphene (chapter 3) and graphene nanostructure and the information obtained from these tunneling spectroscopy data (chapter 4) as well as the transport studies of nanostructures in MoS_2 (chapter 5).

Chapter 2: Planar Pb Tunnel Probes on Graphene[†]

2.1 Introduction

As we mentioned in the introduction, tunneling spectroscopy is an important method used to study the electronic properties of materials, as it has the capability of probing the energy dependence of the electronic density of states and energy distributions. For example, STS has been widely used to elucidate the electronic properties of graphene[80]. STS is very useful, but it typically requires specialized equipment (i.e., scanning tunneling microscopes) having limited ranges of temperature, magnetic field, sample size, and surface properties. More accessible tunneling spectroscopy can be achieved via lithographically-fabricated planar tunnel junctions[81-84], where a metal probe is separated from the material under study by a thin insulating barrier. While planar tunneling cannot provide data with spatial resolution equivalent to STS, planar tunnel probes can have similar energy resolution, and, crucially, better configurability within a standard measurement set-up (e.g., insulating substrates at ultra-low temperatures and high fields). Also, it is simple to fabricate planar tunnel probes out of various materials; for example, using a superconductor as the tunnel probe, Andreev bound states[32] and electron-electron interactions[85] can be studied. For most planar tunnel junctions, the key to obtain good tunneling properties is creating a thin barrier having no direct conduction channels ("non-leaky"). This can be achieved either by deposition and oxidation of

[†] This work is reproduced in part from: Li. Y., Mason, N. Tunneling spectroscopy of graphene using planar Pb probes. Appl. Phys. Lett. **102**, 023102 (2013)

metals such as Al, Pb, or Mg, or by direct deposition of an oxide such as Al_2O_3, HfO_2 or SiO_2[8]. The most commonly used material for tunnel junctions is aluminum, due to its ability to form a very thin (2-3nm) insulating oxide layer. However, a particular material might prefer a particular tunnel probe, e.g. Pb tunnel probes work well on $YBa_2Cu_3O_7$ because of the way the oxygen reacts with the Pb to create an insulating oxide layer[86, 87]. There has been limited use of planar tunnel junctions in graphene, likely because of the difficulty in creating the thin insulating barriers required. The common oxide insulators often do not coat graphene well; for example, aluminum oxide deposited via atomic layer deposition does not coat uniformly without extra chemical fuctionalization[88-90]. Thin SiO_2 on graphene typically has conducting pinholes, while metals which can be oxidized, such as Al, do not form thin uniform surface layers. Planar Cu has recently been used to create tunnel probes[91], but these require acid erosion and long time aging. In contrast, we find that Pb deposited directly on graphene forms robust, high quality and high yield tunnel junctions. We demonstrate that the Pb-graphene interface becomes more resistive over several days, likely due to oxidation at the interface, and that this process of oxidation is self-limiting. We also compare Pb-graphene junctions to similarly-fabricated junctions of Al-graphene and Au-graphene, and show that the Pb-graphene junctions are the most reliable for reproducible tunneling experiments. In the next chapter, we will demonstrate the flexibility of these Pb tunnel junctions by utilizing them for low-temperature, magnetic and electric field-dependent spectroscopy of the graphene, observing energy-dependent features such as scattering resonances and localization behavior[7]. This shows that Pb tunnel junctions can be a simple and useful tool for attaining high energy resolution spectroscopy in graphene under a wide range of conditions.

2.2 Device fabrication and measurement configuration

Figure 2.1 and 2.2 show a typical device, which consists of graphene having nearly Ohmic Ti/Au contacts at the ends, and two tunnel probes connected to the middle. The graphene used for this study were obtained using the exfoliation method[2] and ranged from 2-4 layers (measured via atomic force microscopy); the behavior of the probes was independent of the exact layer thickness. Standard electron-beam (e-beam) lithography and subsequent e-beam deposition were used to pattern the 4 nm Ti/700 nm Au end contacts. A second e-beam lithography step was then used to pattern the probes, which were approximately 200 nm wide and extended 100 ~ 500 nm into the graphene. Al and Ti/Au for the probes were e-beam evaporated, and the Pb was thermally evaporated. The Pb probes were covered with a 30 nm In cap to reduce oxidation at the top surface.

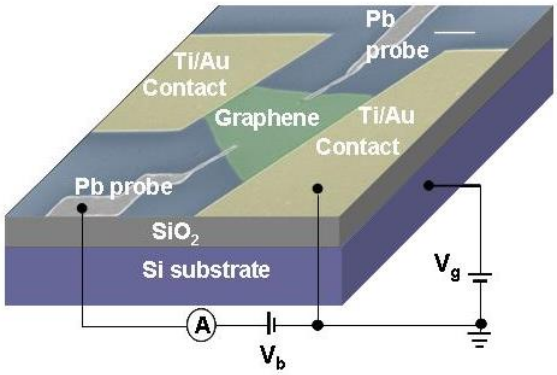

Figure 2.1. Scanning electron micrograph (SEM) of a typical device with an overlaid measurement circuit (false-colored for improved contrast). The scale bar is 2 μm.

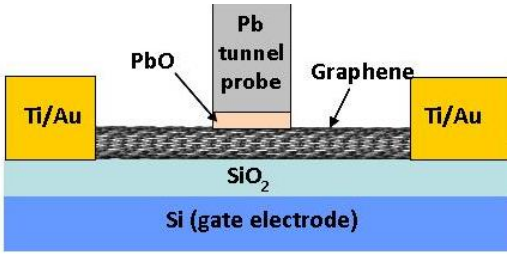

Figure 2.2. Side-view schematic diagram of the device, showing where PbO forms under ambient conditions.

2.3 Tunneling barrier formed at the graphene-Pb interface

Resistance was measured in two-probe configuration by applying a bias voltage, as shown in Figure 2.1; the doped substrate was used as a global backgate. A schematic of the finished device is shown in Figure 2.2. Although the two-probe technique included the resistance of the Ti/Au end contact, this contact resistance was typically much lower than that of the tunnel probes (compare Figure 2.3a to Figure 2.3b), and did not have significant time-dependence. Figure 2.3a characterizes the typical resistance of the graphene (here, 4-layer) through the Ti/Au end contacts, as a function of backgate voltage and time. The graphene displays a clear bipolar feature and a Dirac point; the Dirac point is initially near $V_g = 0$V and shifts toward positive voltages as time increases, likely due to oxygen doping under ambient conditions. The overall resistance of the graphene through the end contacts is relatively constant in time. This behavior can be contrasted with that of the Pb-graphene junction, as shown in Figure 2.3b. The Pb-graphene characteristics are initially nearly identical to those of the Ti/Au-graphene junctions, and the Dirac point again shifts toward positive voltages as oxidation time increases. However, the resistance of the Pb-graphene junctions flattens substantially over time, with the Dirac point and the bipolar features becoming less and less visible. Even more striking is the large, nearly 70-fold increase of the Pb-graphene junction resistance over time.

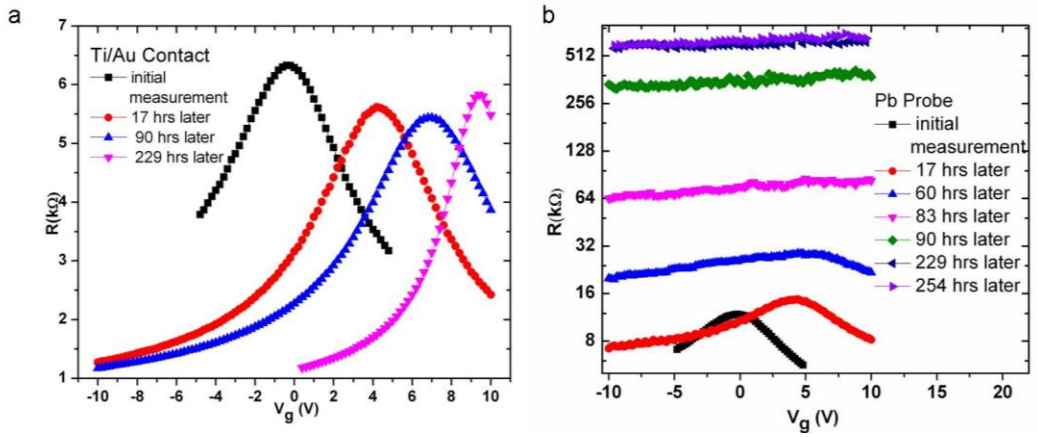

Figure 2.3. Time dependence of the backgate characterization of a tyical Pb probe on graphene. (a) Typical resistance vs. backgate voltage for Ti/Au-Ti/Au end contacts on graphene, as a function of time spent under ambient conditions. Initial measurement is performed ~1hr after the device fabrication is finished. (b) Typical resistance vs. backgate voltage for a Pb probe on graphene, as a function of time spent under ambient conditions.

We studied 14 Pb probes on graphene (on 2 substrates), 7 Al probes on graphene (1 substrate), 12 Ti/Au probes on graphene (2 substrates) and 3 Pb probes on Au (1 substrate). The resistance of these probes as a function of time left under ambient conditions (i.e., oxidation time) was monitored for about 10 days starting from immediately after the device fabrication was finished. The increase of the Pb-graphene junction resistance is characterized in Fig 2.4a, which shows resistance vs. oxidation time for 5 different junctions. All the junctions demonstrate similar behavior. When first deposited, the Pb probe resistance is comparable to that of the Ti/Au contact. Then, it increases slowly (roughly doubles every half day) during the first few (1~4) days, after which it quickly (within 10 hrs) increases dramatically—by a factor of 5-10—to hundreds of kΩ. After this point, the Pb resistance starts to saturate, and does not change significantly over the rest of our measurement time (an additional 6 days). The saturation resistance differs somewhat from probe to probe, even for probes on the same piece of graphene, and does not seem to correlate with parameters such as graphene thickness or

probe-graphene overlap area (for the constant probe width of ~ 200 nm). [However, for probes with a much larger probe-graphene overlap area (length, width ~ 1 μm), it does take a longer time to fully oxidize the Pb, and sometimes the Pb will not form a good tunneling barrier even after long oxidation times.] Similar Pb-graphene junction time evolution was observed in 11 out of 14 samples that were measured (the 3 outliers had atypical resistances for all contacts, likely due to fabrication issues). This behavior therefore seems to be highly repeatable and robust. We compare the yield of the tunnel probes made from different materials in table 2.1.

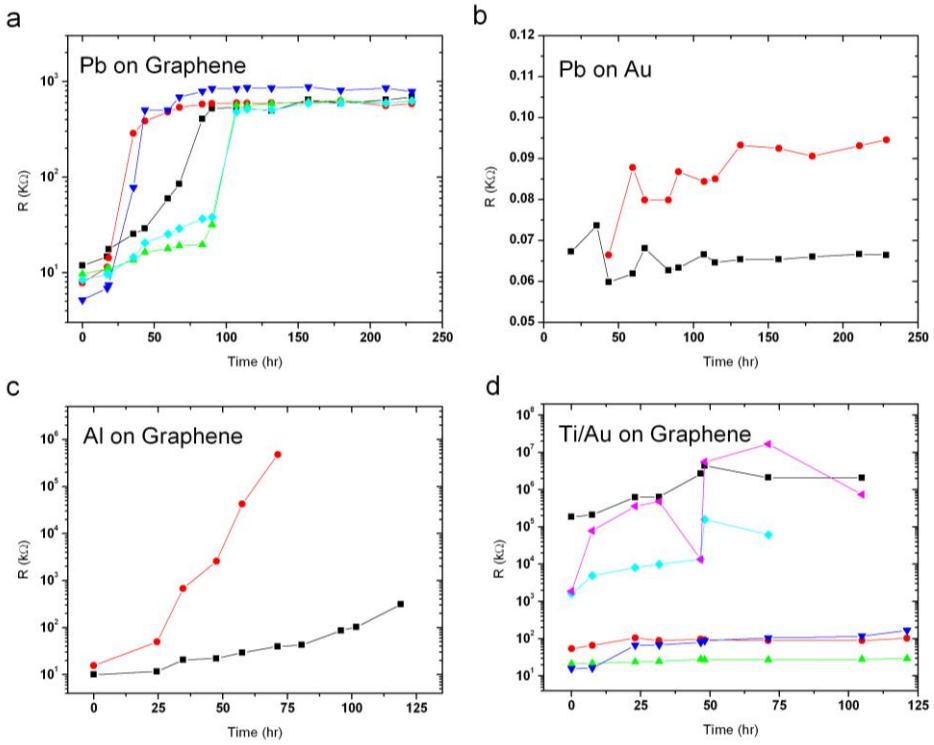

Figure 2.4. Distinct behaviors of probes made from Pb, Al and Ti/Au on graphene, and of Pb on Au. Time dependence (i.e., wait time under ambient conditions) of the probe-on-graphene resistance for different probe materials: (a) Pb, (c) Al, and (d) Ti/Au. (b) Resistance of Pb probe on Au pad as a function of time. Different colors represent data for different probes (for each material, probes were fabricated on several different graphene flakes, on multiple substrates)

The large increase in Pb-graphene junction resistance with time suggests that oxidation occurs at the interface between the graphene and the Pb, which likely causes a PbO tunnel barrier to form. While it is common for oxides to form on exposed surfaces, it is less expected for oxides to form at the interfaces between materials. In the case of Pb on graphene, the interface oxidation seems to depend on the presence of graphene: in Fig 2.4b we show that similar Pb probes fabricated on Au pads have low resistances that do not change with time. It is possible that the weak coupling between Pb and graphene allows oxygen to diffuse into the interface from the sides[92, 93], in a way similar to the capillary action which preferentially draws etchant under graphene[94, 95]. For the surface of bulk Pb, the rate of oxidation has been found to be greatly reduced once a certain oxide thickness has been reached[96], which is consistent with the saturation behavior we observe..

Probe material	Pb	Al	Ti/Au
Number of probes made	14	7	12
Number of conducting probes	11	2	5
Number of usable tunnel probe (in a week)	11	1	?

Table 2.1. Yield comparison of tunnel probes made from different materials, including Pb, Al and Ti/Au.

As a comparison for the Pb junctions, we also studied junctions of Au and Al on graphene. In contrast to the Pb probes, the Al probes are generally unreliable: out of 7 Al probes fabricated on graphene, only 2 were conducting. In addition, as can be seen from Fig 2.4c, the resistance of the surviving probes quickly increased over time without saturating. Although Al is expected to form an Al_2O_3 tunneling barrier at the interface[91], the fast-rising resistance and low yield makes it inferior to Pb probes made in the same way. The Ti/Au probes on graphene were also less reliable than the Pb ones: 5 out of 12

Ti/Au probes on graphene were not conducting. The remaining probes had highly variable contact resistance, ranging from a few tens of kΩ to MΩ. However, as can be seen in Fig 2.4d, none of the Ti/Au probes showed significant time dependence of the resistance, which implies that oxidation did not occur and a tunnel barrier was not formed at the interface.

2.4 Basic tunneling measurement using the Pb probe

The high quality of the Pb probes can be determined via transport measurements. It is particularly useful to measure below the Pb superconducting transition temperature of 7.2 K, as the low voltage-bias conductance is then dominated by the characteristic Bardeen-Cooper-Schrieffer shape of the density of states. In this case, there are no single-particle states for an energy scale of $\pm \Delta$ (the superconducting gap energy), and sharp peaks appear in the differential conductance at the gap edges. This gap feature in conductance is a typical characteristic of superconductor-normal tunneling[97], and the quality of the tunnel barrier can be determined by the quality of the gap. In particular, no conductance observed around zero bias implies that the tunnel barrier is not leaky. A lack of conduction inside the gap also implies that the tunnel barrier is fully insulating, as an overly-conducting tunnel barrier would allow quasiparticle transfer inside the superconducting gap[39] (via a process known as the Andreev reflection). Figure 2.5 shows differential conductance vs. tunnel voltage bias for Pb-graphene junctions at 250 mK. Most Pb probes that reached a minimum resistance of several hundred kΩ showed similar behavior.

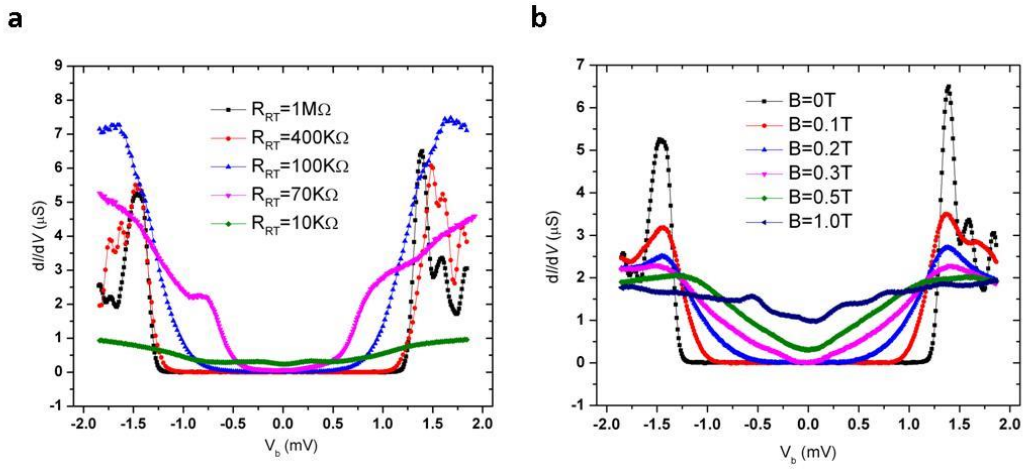

Figure 2.5. Characterization of the Pb tunneling probe at 250 mK. (a) Differential conductance vs. tunnel bias V_b for Pb probes having different resistances at room temperature (oxidized for different times). Conductance for different probes is normalized according to their room temperature resistances. The more resistive probes show a cleaner gap feature, which originates from superconducting density of states. Oscillations outside the gap edge are shown as fine oscillations which will be covered in the next chapter. (b) Magnetic field dependence of differential conductance vs. bias voltage. As magnetic field increases, the gap feature gradually disappears, confirming that the gap feature arises from superconductivity.

The measurements were performed in 2-point configuration using standard lock-in techniques in a He-3 refrigerator, using an ac excitation of 0.02 mV. In Fig 2.5a, the differential conductance for probes at different stages of oxidation is characterized. Probes that have not been fully oxidized (i.e., measured well before they reached saturation resistance) show no gap or incomplete gaps, and no or broad peaks at the gap edges. In contrast, the probe that was fully oxidized (black curve in Fig 2.5a) exhibits the full expected gap for Pb, $2\Delta = 2.6$ meV, as well as well-defined peaks at the gap edges. No sub-gap conductance is evident within the resolution of our measurements, implying that the barrier is fully insulating. It is also evident in Fig 2.5a that a range of resistances can enable good tunneling properties, as long as a minimum resistance (presumably related to oxide thickness) is reached. In Fig 2.5b we show the magnetic field dependence

of the gap, which is consistent with what is expected for superconducting tunnel junctions, where the de-pairing effect of a magnetic field lifts the gap.

2.5 Conclusion and discussion

We have found a simple, efficient and reliable way of making planar tunneling probes by directly depositing Pb on graphene. We show how Pb probes are unique, compared to Al and Au probes, and perform tunneling measurement using the probes. The oxidation of the Pb-graphene interface seems uniquely self-limiting. We have also performed basic tunneling measurement using these probes. There has been great interest in the spectroscopy of graphene, yet limited ways of obtaining this information. Our findings provide more possibilities for investigating the microscopic electronic properties of graphene via tunneling spectroscopy. The unique interface reaction (or possibly hybridization also) between graphene and Pb enables the tuning of the interface barrier from the tunnel regime to the low barrier case (when the probability of Andreev Reflection is significant) via the control of the oxidation time, as revealed by Fig 2.5b. We need to point out that a clean sharp gap in the tunnel conductance by itself is not necessarily the sign of a strong tunnel barrier but could also result from the superconducting proximity effect, where a superconducting energy gap is induced in graphene. However, as we will show in the next chapter, using these Pb planar probes, we have performed tunneling spectroscopy of graphene and observed features very similar to STS studies, which supports that the probes are working in the tunnel regime. In future work, further information about the barrier could be gained by measuring temperature dependence of the resistance of the probes.

Chapter 3: Tunneling Spectroscopy of Graphene using Planar Pb probe

3.1 Introduction

Having discussed the creation of a high-quality planar tunnel junction on graphene, we now turn to tunneling spectroscopy at low-temperatures, and finite magnetic fields and gate voltages, performed on seven different devices. We will analyze the features observed and discuss their possible origins in this chapter. Although some of the features are inter-related, we put them into three categories, based on the back gate and magnetic field dependence. First, we discuss the fine oscillations just outside the superconducting gap, which disappear when a small magnetic field is applied; an example of these is given in Fig 3.1a and 3.1b, in the region between the yellow dashed lines. Its origin could be related to phonons in graphene, or resonances through localized electron regions. Next, we discuss the sparser and broader lines, as marked by white arrows in Fig 3.1a and 3.1b, which do not go away with the magnetic field and could possibly be graphene-derived localized states, due to their similar magnetic field dependence compared to the Landau levels. Finally, we discuss the triangular features shown in Fig 3.1c and observed in two samples, which could be Coulomb blockade but do not agree with the magnetic field dependence of the etched quantum dot. We discuss how much of the data may be related to the localization behavior in the spectrum due to quantum dots formed at high magnetic field and originating from the disorder potential.

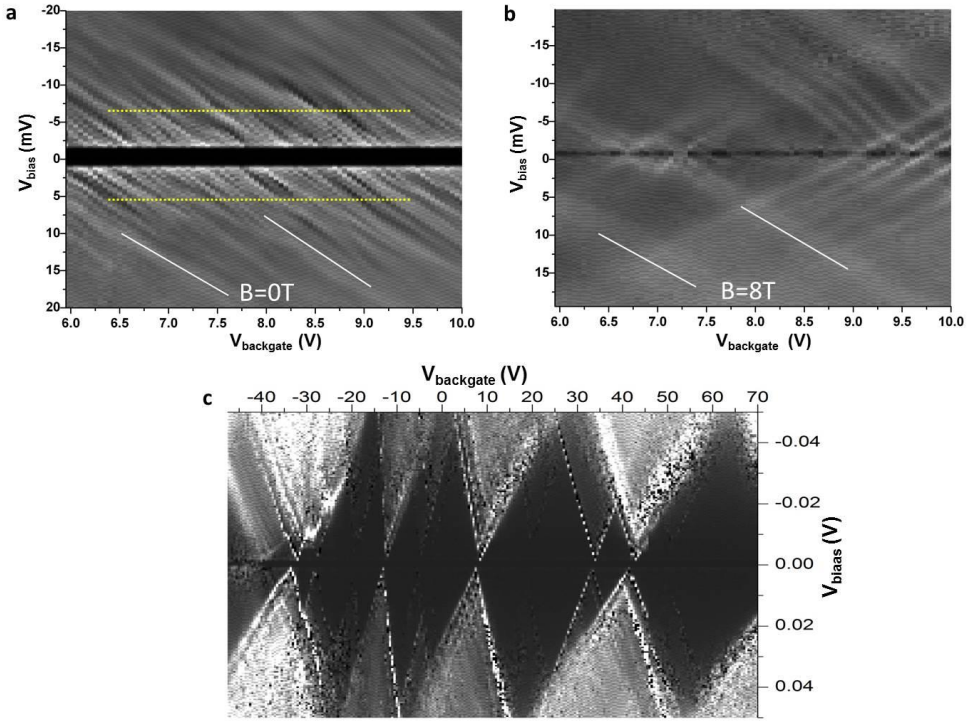

Figure 3.1. Tunneling spectra of graphene showing three characteristic features. (a) The fine oscillations show up in the bias range from zero bias up to the yellow dashed lines. (b) The broader resonances marked by the white lines, still exist when a high magnetic field is applied. (c) The 'Coulomb diamonds'.

3.2 The fine oscillations near the superconducting gap

3.2.1 General appearance and characteristics

Let us first introduce the fine oscillations by looking at the tunneling data in Fig 3.2c, which shows 2D plots of differential conductance vs. tunnel voltage bias for a bilayer graphene sample, as a function of back gate voltage. For this data, we focus on energy scales larger than the superconducting gap energy. In the data, patterns of peaks and oscillations are evident as white lines (of high differential conductance) that evolve with tunnel bias, magnetic field, and/or back gate voltage. When a magnetic field is applied, these oscillations disappear (see Fig 3.3a and 3.3b). Figure 3.3a shows their

evolution with increasing magnetic field: as pointed out by the arrows, some peaks have a slope change as the magnetic field increases. Just like in Fig 3.3a, the slope changes with the magnetic field are also visible in another sample as shown in Fig 3.14d. It is hard to extract useful information from these complex conductance patterns, which are reproducible, though. Although we do not have a good understanding of this slope change, it is worth pointing out that slope change of Coulomb blockade peaks with increasing magnetic field has been observed in graphene quantum dots[56, 98, 99] and is a sign of higher filling factor. However, those slope changes happen at much higher fields compared to our data.

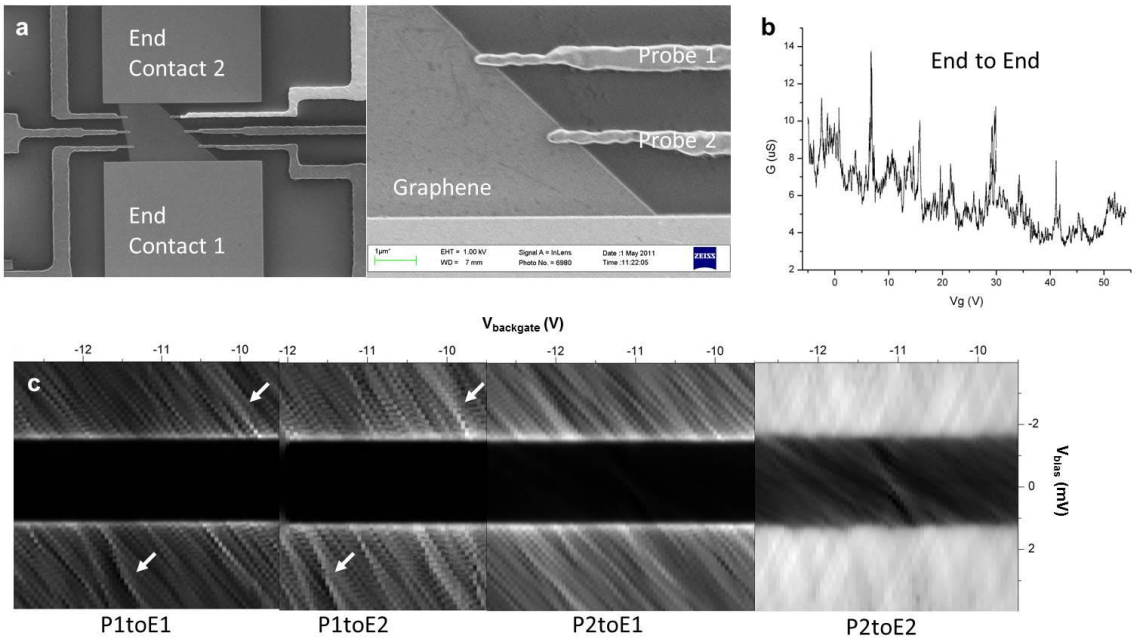

Figure 3.2. Surface characterization, back gate characterization, back gate of tunneling spectra of Sample-040410. (a) SEM image of the device. (b) Differential conductance vs. back gate voltage measured from end to end contacts. (c) 2D map of differential conductance versus dc bias voltage V_{bias} and back gate voltage $V_{backgate}$, taken on the same back gate range, from different probes to different end contacts. The dark horizontal band centered at zero bias comes from the superconducting gap. Fine oscillations appear just outside the superconducting gap. White arrows point out the similar irregularities in spectra taken from the same probe to different end contacts, which do not appear in the other probe.

The fine oscillations are observed in all devices. By comparing and analyzing the fine oscillations observed in different devices, we find they have three characteristics in common: their irregularities are related only to the particular probe; the sign of their slope depends on the coupling at the contacts; the oscillations go away with a small magnetic field (~ 0.2 T).

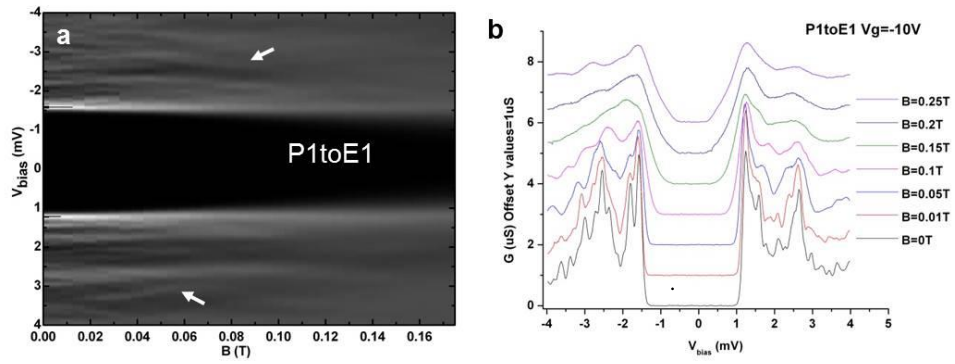

Figure 3.3. Magnetic-field dependence of tunneling spectra of Sample-040410. (a) 2D map of differential conductance versus V_{bias} and magnetic field B taken at zero back gate voltage from probe 1 to end contact 1. As the magnetic field increases, the sharp fine features become broadened and smeared. Some peaks show a change in the B-dependent slope as pointed out by the arrows. (b) Magnetic field dependence of differential conductance vs. bias voltage. As the magnetic field increases, the fine oscillations features gradually disappear.

3.2.2 Probe-dependent irregularity

In the backgate-dependent spectra of Fig 3.2c, Fig 3.4c and 3.4d, the fine oscillations that evolve diagonally away from the zero-bias gap towards higher biases can be seen in different probes. White arrows point out the similar irregularities in the spectra measured from one probe to different contacts, not in the spectra measured from the other probe to different contacts (measurement done with bias on probe A, while end contact B is grounded and the other contact C is floated is referred to as from probe A to end B, similar for end to end, probe to probe, etc.).

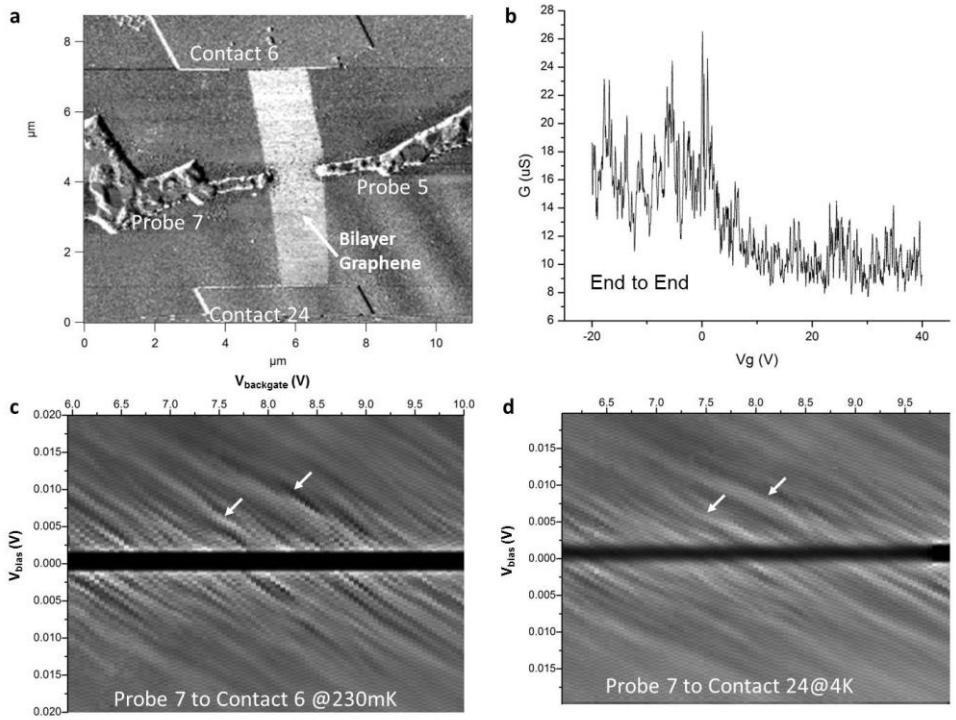

Figure 3.4. Surface characterization, back gate characterization and tunneling spectra of Sample-081212 Device A. (a) AFM image of the device. (b) Differential conductance vs. back gate voltage measured from one end contact to the other. (c) (d) 2D map of differential conductance versus dc bias voltage V_{bias} and back gate voltage $V_{backgate}$, taken on the same back gate range, from different probes to different end contacts. The fine oscillation features from the same probe to different contacts are very similar (as pointed out by the arrows, the irregularities appear at the same position in the 2D map, the difference in the sharpness is very likely due to the temperature difference). Fine oscillations from different probes do not look identical but are similar (in terms of the slope and period of the oscillations).

This seems to lead to a conclusion that the oscillations could depend on the probe 'itself'. However, since the probe is made of Pb, it should not have any back gate dependence as the oscillations do.

3.2.3 The slope sign and contact asymmetry

Another characteristic of the fine oscillations is that the sign of the slope is negative in all the spectra measured from probe to end contact. This consistency of slope sign comes from that fact that coupling at the graphene-Pb probe interface, which can

form a tunnel barrier, is usually weak compared to the normal metal contact-graphene interface, which is Ohmic most times. If the coupling at the two contact interfaces is the same, the spectra should be symmetric, i.e. these oscillations features should have components with both positive and negative slopes. The weak coupling at the Pb tunneling probe prevents the appearance of the oscillations with a positive slope. This point is supported by the fact that when the contact coupling at one of Pb probes is not weak compared to the end contact (such a probe is P2 in Fig 3.2c, P2toE2), the oscillations have shown slope with both signs. Similar support can be found in the 2D map measured from probe to probe, where the slope of the oscillations flips the sign when bias polarity is switched as shown in Fig 3.5.

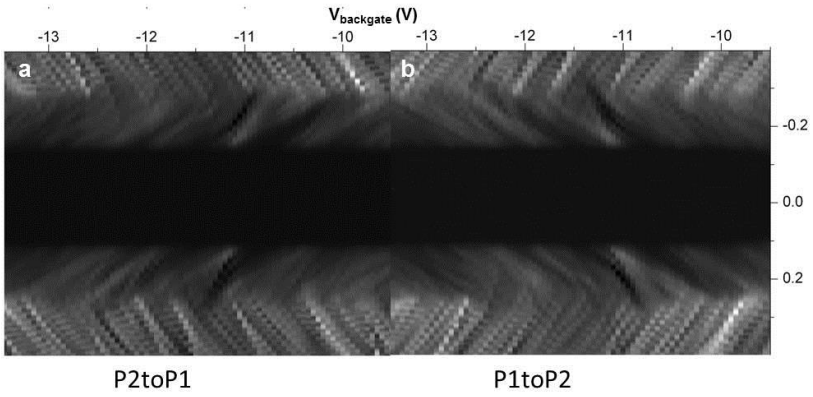

Figure 3.5. Back gate dependence of tunneling spectra of Sample-040410. 2D map of differential conductance versus dc bias voltage V_{bias} and back gate voltage $V_{backgate}$, taken from one probe to the other.

A crossing pattern which resembles Fabry-Perot oscillations is observed in the end to end 2D map as shown in Fig 3.6b. However, these are unlikely to be caused by ballistic transport, based on the following two observations: the overall conductance is small compared to the conductance quantum (G_{max} ~ 14 μS compared to $2e^2/h$ = 77.5 μS); the length of sample is much larger than the mean free path (~ 100 nm)[100, 101]. In most other samples, the end to end 2D conductance map usually does not show crossing

pattern like the one in Fig 3.6b but is relatively flat like the one in Fig 3.6a. Whether this crossing pattern is related to the fine oscillations observed in the tunneling data remains an open question. However, we find that weak coupling could have something to do with the appearance of crossing pattern in the end to end 2D map. Evidence is the asymmetry in the tunneling spectra with respect to the bias as can be seen in Fig 3.6b, which indicates one of the two end contacts is not as good as the other.

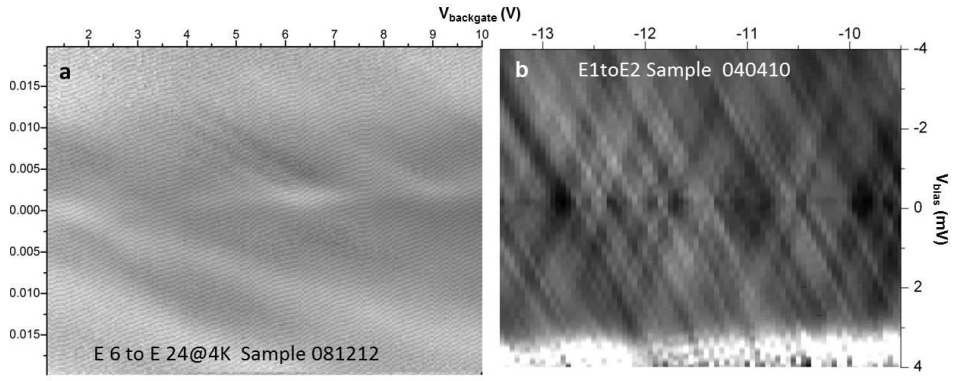

Figure 3.6. Comparison of the end to end transport of Sample-040410 and Sample 081212. 2D map of differential conductance versus dc bias voltage V_{bias} and back gate voltage $V_{backgate}$, taken from one end contact to the other for (a) Sample-081212 and (b) Sample-040410. The crossing pattern is Fabry-Perot like; however, ballistic transport is unlikely to happen in a sample of this length.

3.2.4 Magnetic field dependence and discussion of the origin

Finally, the fact that the fine oscillations go away with a small magnetic field leads to the possibility that they originate from superconductivity. Another guess is that these features may be McMillan-Rowell oscillations, which are due to interference between quasiparticles reflected from superconductor-normal interfaces[102], and are evident via tunneling measurements. Such oscillations can be used to extract parameters such as the Fermi velocity v_F, as they are predicted to have bias spacing of $\Delta V_b = hv_F/(4ed_N)$, where d_N is the length scale of the normal metal[103]; for our experiments,

although d_N varies in the 2D graphene, the predicted $\Delta V_b \sim 0.5$mV is comparable to the typical peak spacing we observed.

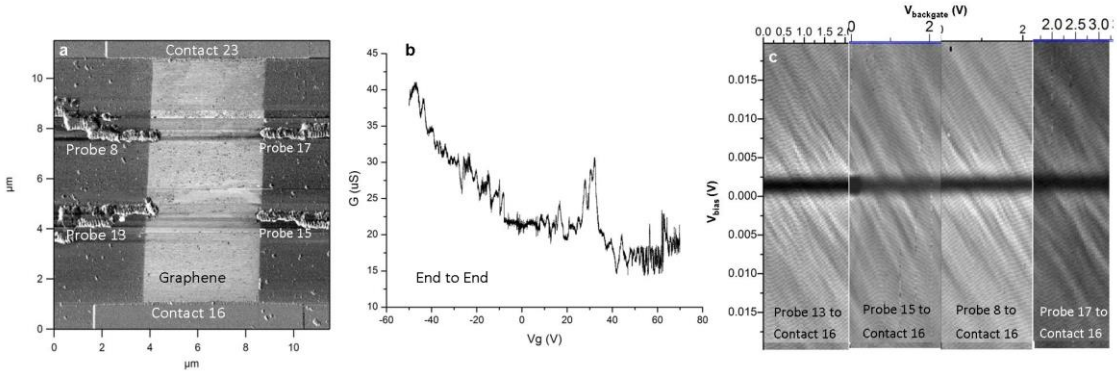

Figure 3.7. Surface characterization, back gate characterization and tunneling spectra of sample-081212 Device B. (a) AFM image of the device. (b) Differential conductance vs. back gate voltage measured from end to end contacts. (c) 2D map of differential conductance versus dc bias voltage V_{bias} and back gate voltage $V_{backgate}$, taken on the same back gate range, from different probes to different end contacts. Consistent with what is observed in sample-081212 Device A: the fine oscillation features from the same probe to different contacts are very similar (again, many irregularities exist in oscillations appear at the same position in the 2D map but are not the same in different probes); Fine oscillations from different probes do not look identical but are similar (in terms of the slope and period of the oscillations).

However, as we compare the tunnel spectra taken on probes at different distances from the normal contacts, we find the fine oscillations are very similar in period/spacing (as can be seen in Fig 3.7c), which indicates that mechanism other than McMillan-Rowell oscillations is needed. Resonances due to electron-phonon coupling are another possibility. Temperature dependence of these oscillations could help towards a better understanding of their origin.

Actually the fine oscillations have a very similar slope to the broader resonance that we will show and discuss in the next section (in some samples, it is even hard to distinguish one from the other except for the period and magnetic field dependence). The fact that these fine oscillations disappear with a small magnetic field lead us to think that

they have the same origin as the broader resonances and are sharper due to the enhancement by the superconductivity.

3.3 The broader resonances

A set of broader resonances is marked in Fig 3.8a and 3.8b by white lines; these peaks are broader, more separated, and do not disappear with applied magnetic field compared with the fine oscillations discussed in the previous section. Yet, in some samples (Fig 3.9c, 3.9d and Fig 3.11), the two sets of resonances are very similar to each other, indicating their close relationship. More such broader resonance features are observed in different samples and another example can be seen in Fig 3.12c and 3.12d.

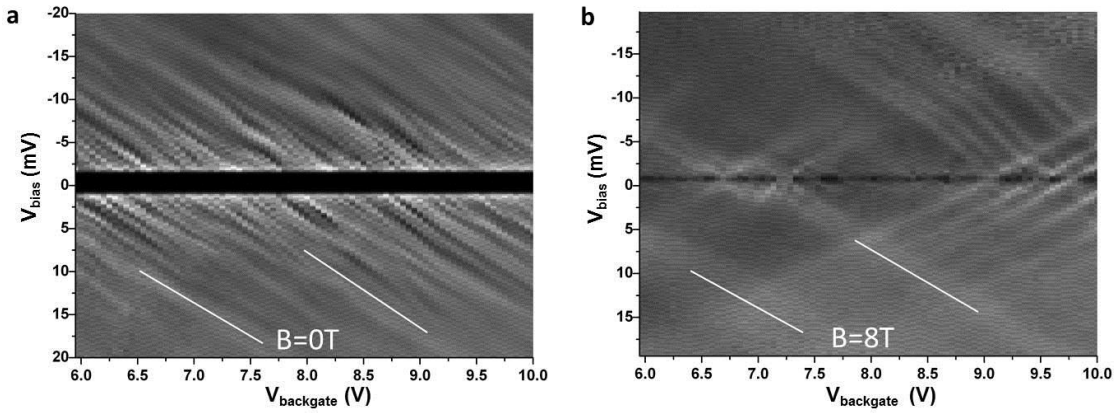

Figure 3.8. Back gate and magnetic-field dependence of tunneling spectra of sample-081212 Device A, measured from probe 7 to contact 6. (a) Two-dimensional (2D) map of differential conductance versus dc bias voltage V_{bias} and back gate voltage $V_{backgate}$ from probe to end. (b) Similar 2D map taken on the same back gate voltage except with an 8 T magnetic field perpendicular to the plane of substrate. Arrows point to fine oscillations that disappear with applied magnetic field. White lines are guides to the eye showing broader resonances which persist with magnetic field.

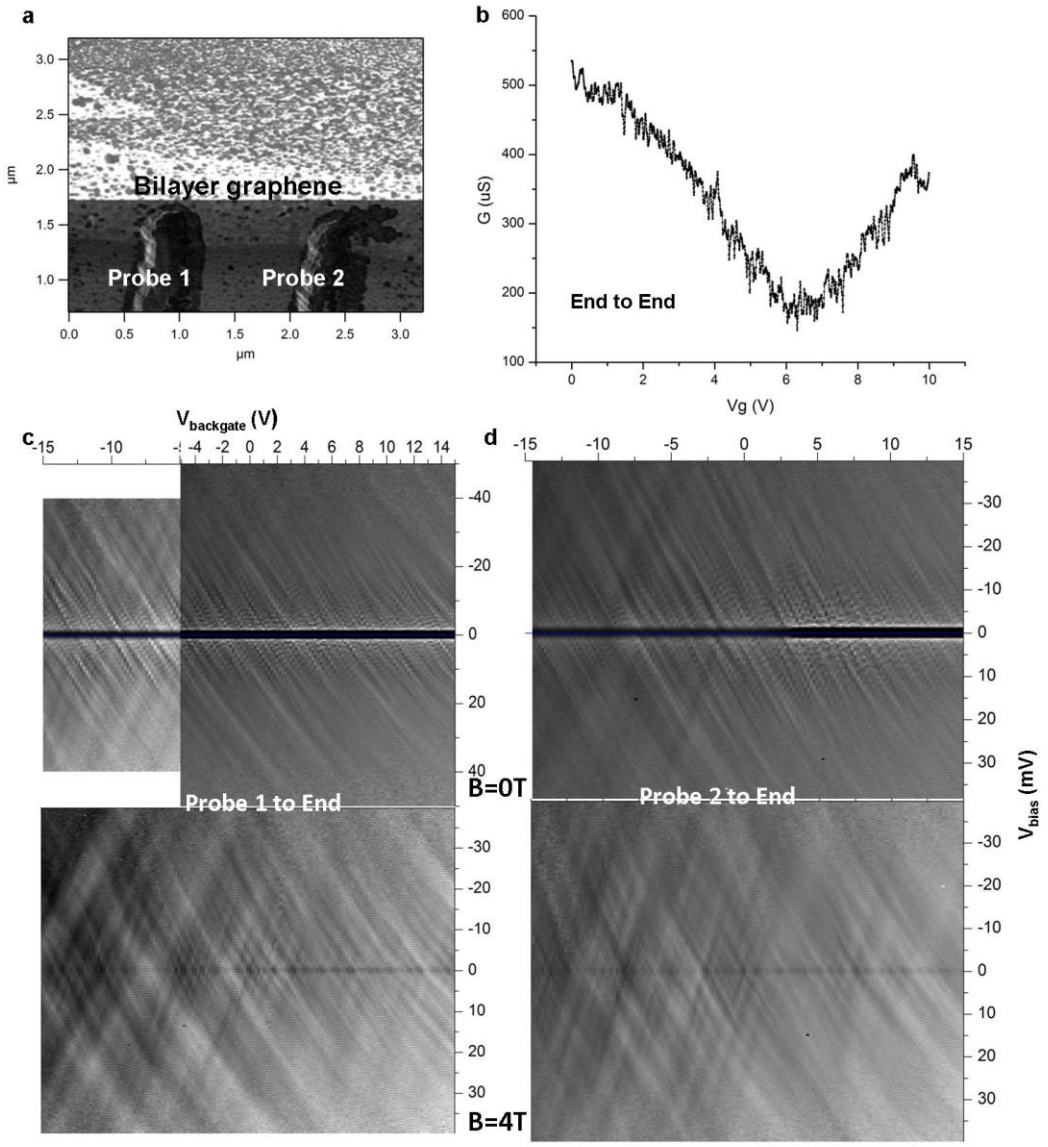

Figure 3.9. Surface characterization, back gate characterization and magnetic-field dependence of tunneling spectra of sample-050613. (a) AFM image of the device. (b) Differential conductance vs. back gate voltage measured from end to end contacts. (c) 2D map of differential conductance versus dc bias voltage V_{bias} and backgate voltage $V_{backgate}$, measured from probe 1 to end contact. The lower map is taken on the same back gate range as the upper one except with a magnetic field 4 T perpendicular to the plane of the sample. (d) Similar 2D map as (c) except taken from probe 2 to end contact.

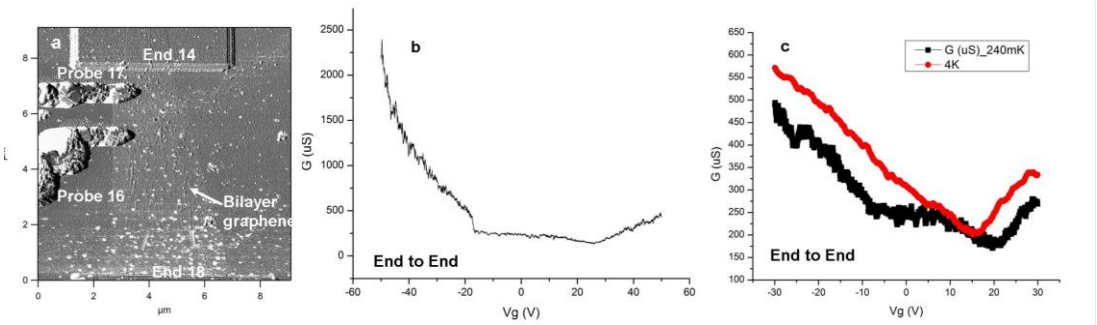

Figure 3.10. Surface characterization, back gate characterization and magnetic-field dependence of tunneling spectra of sample-100812. (a) AFM image of the device. (b) Differential conductance vs. back gate voltage measured from end to end contacts. (c) Similar back gate characterization as (b) except on a smaller back gate range and with a comparison between two different temperatures 4 K and 240 mK.

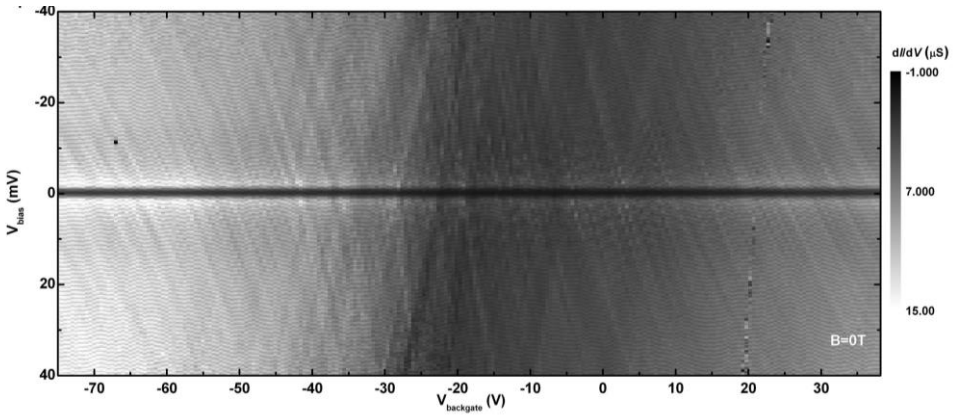

Figure 3.11. Tunneling spectra of sample-100812 without magnetic field. 2D map of differential conductance versus dc bias voltage V_{bias} and back gate voltage $V_{backgate}$, taken from probe 16 to end contact 14.

One difference in the spectra shown in Fig 3.11 compared to others is that near the Dirac point, the conductance is significantly lower, shown as the dark band in Fig 3.11. This low conductance is also seen in the same backgate range in the end to end transport as shown in Fig 3.10b and 3.10c and could be related to the 'Coulomb diamonds' feature which we will discuss later. Other than that, the broader resonances observed in different samples are very similar in terms of the bias range they could be observed (40 meV), the peak broadening as the magnetic field increases and the slope change with the backgate voltage. The broadening in resonance width with increasing

magnetic field could be related to the quantum dot formation in high magnetic field which we will discuss later. The slope change with the backgate voltage is a sign that these resonances could be graphene-derived states.

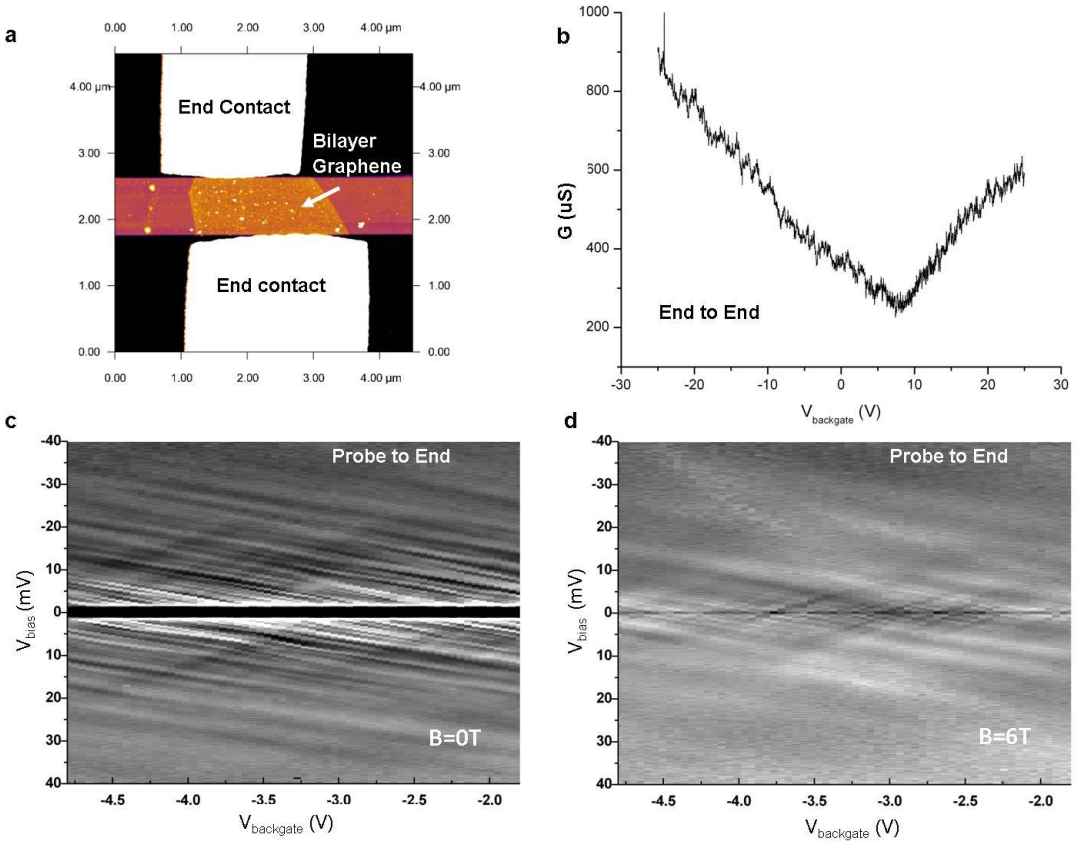

Figure 3.12. Surface characterization, back gate characterization and magnetic-field dependence of tunneling spectra of sample-052712_3. (a) AFM image of the device. (b) Differential conductance vs. back gate voltage measured from end to end contacts. (c) 2D map of differential conductance versus dc bias voltage V_{bias} and backgate voltage $V_{backgate}$, measured from probe to end contact. Note the oscillation peaks become not as intense and dense when the bias range is larger. (d) Similar 2D map as (c) taken on the same back gate range except with a magnetic field 6T. Fine oscillation features near low bias (< 10 mV) go away compare to (c), while the boarder resonances still exist.

3.3.1 Magnetic field dependence

In the tunneling spectra taken with high magnetic field as shown in Fig 3.13, these resonant peaks show a staircase-like back gate dependence, a characteristic feature of Landau levels[104-106]. Another trend qualitatively consistent with the Landau level picture

is that with increasing magnetic field the spacing between these resonances is also increasing. However, quantitatively the spacing between these resonances does not agree with the Landau levels predictions. Although Landau levels are expected in the spectroscopy when a magnetic field is applied to a 2D material[28, 107-109], the low mobility in our sample, which are likely due to the charge impurities on the substrate, could prevent the observation of Landau levels[23]. Yet still, the similarities between these resonances and Landau levels features such as the staircase-like trend and the increasing spacing with the increasing magnetic field indicate that these resonances originate from the graphene-based states. The slope change with the back gate voltage, which is evident in Fig 3.9c and 3.9d, Fig 3.13, also supports this idea.

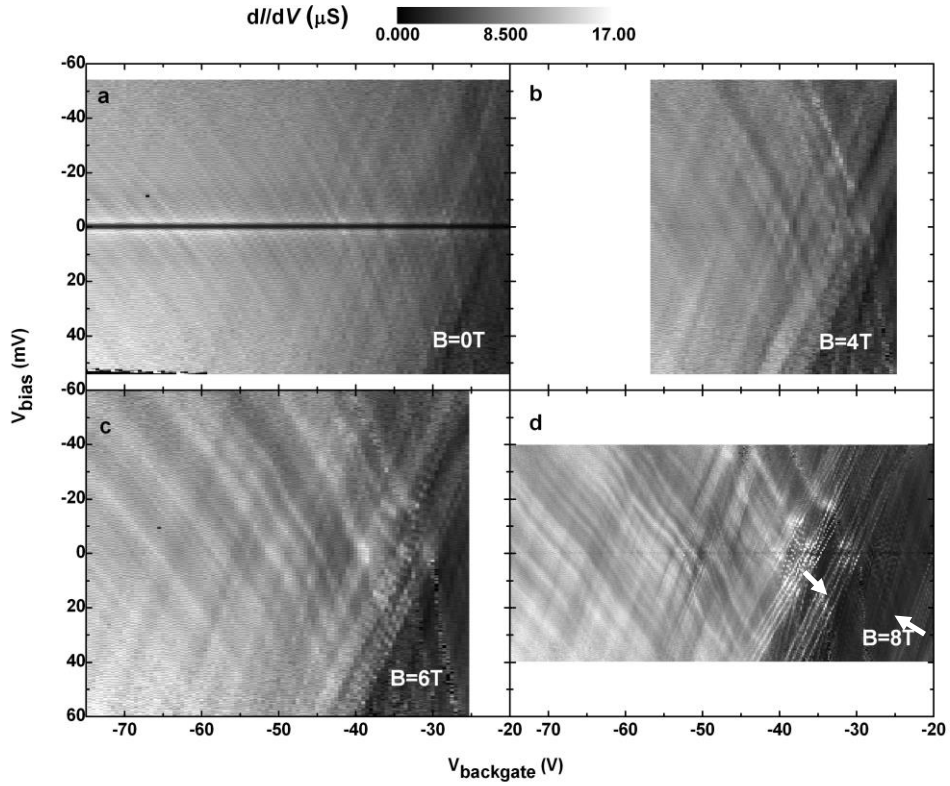

Figure 3.13. Magnetic-field dependence of tunneling spectra of sample-100812. 2D map of differential conductance versus dc bias voltage V_{bias} and back gate voltage $V_{backgate}$, measured from probe 17 to end contact 18 with a magnetic field perpendicular to the plane of the sample: (a) B = 0 T (b) B = 4 T (c) B = 6 T (d) B = 8 T.

Besides the broader resonances, resonance peaks with a negative slope which cross the broader resonances appear at high magnetic field, as pointed out by white arrows in Fig 3.13d. These resonances show up as a group of four and are very similar to the Coulomb blockade features seen in the STS studies[7] (compare Fig 3.13d and Fig 3.16c), which are attributed to weakly localized states in graphene created by impurity scattering or substrate-induced disorder potentials. The four-fold degeneracy can be attributed to two valley-degenerate quantum states accommodating two electrons each (spin-up and spin-down). We will discuss more in details about this localization in the next section. In the STS observations, these blockade features always intersect with the Landau levels at zero bias, which again suggests that the broader resonances we observed, although are not Landau levels, could come from graphene-based states.

More insight can be obtained from the back gate dependence of the tunneling spectra (2D map of differential conductance versus bias voltage and magnetic field), which also supports the idea that they could be graphene-derived states. In tunneling spectra taken with different back gate voltages, shown in Fig 3.14: in the positive back gate range, V_{backgate} = 15V, 8.69V, 0V, the broader resonances appear as the line features with a positive slope; at V_{backgate} = -15V, the 2D map is almost symmetric with respect to zero bias and the line features have a relative small slope; at V_{backgate} = -30V, line features with a negative slope is visible. These line features are not well defined and too irregular compared to Landau levels. However, the fact that the resonances (line features) have a backgate-dependent slope again agrees with the Landau level behavior of graphene.

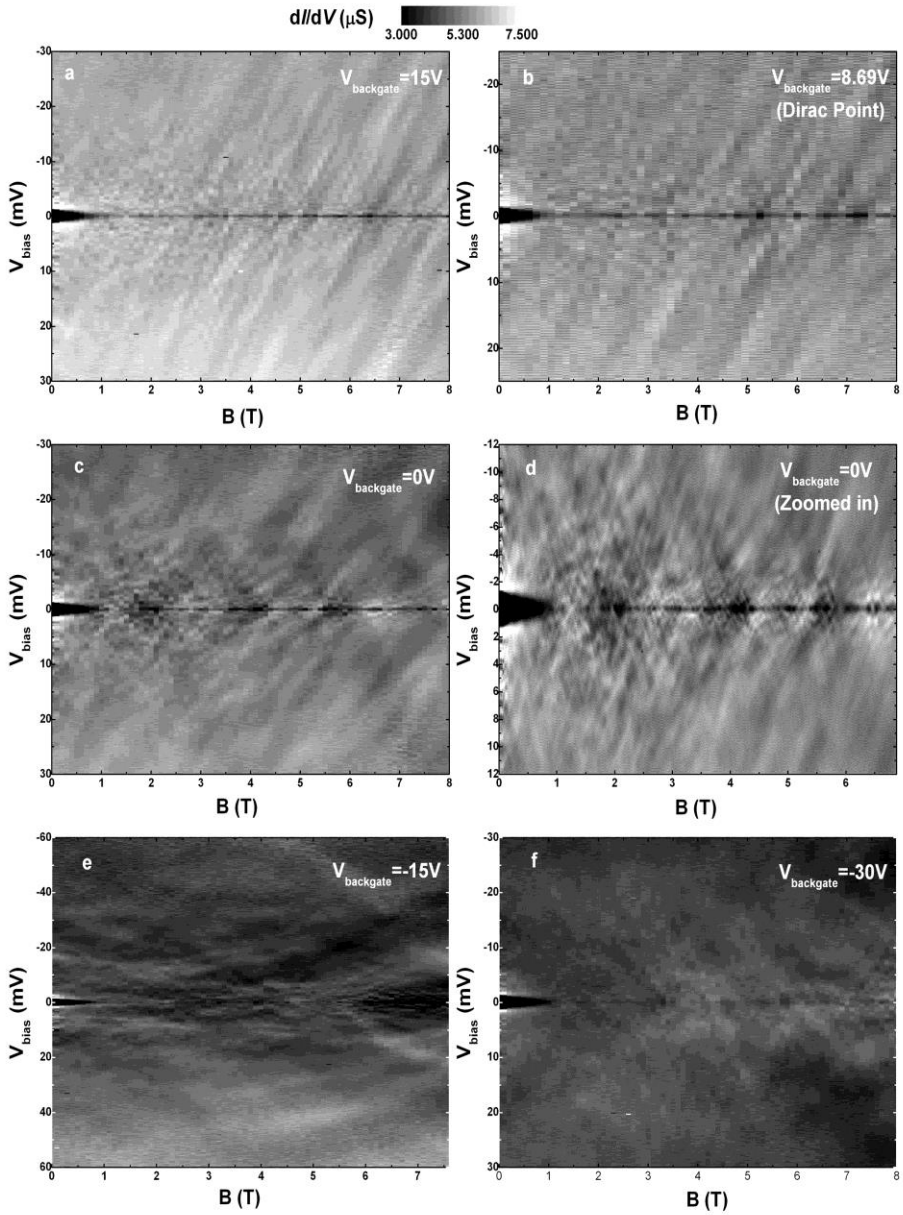

Figure 3.14. Back gate and magnetic-field dependence of tunneling spectra of sample-052712_3. 2D map of differential conductance versus dc bias voltage V_{bias} and magnetic field B, taken on different back gate voltage: (a) $V_{backgate}$ = 15 V; (b) $V_{backgate}$ = 8.69 V; (c) $V_{backgate}$ = 0 V; (e) $V_{backgate}$ = -15 V; (f) $V_{backgate}$ = -30 V. (d) is a zoomed-in (higher resolution as well) version of (c).

The fact that Landau levels behavior is observed but the energy spacing does not match could be due to the electronic orbital being disturbed by the strong disorder. In the STS studies, where quantum dot formation in high magnetic field is observed[7], Landau

levels are still be clearly visible—which tells us the presence of quantum dots/confined regions may not affect the observation of Landau levels. However, Landau levels would be broadened in the presence of disorder. We also note that, in the studies on etched graphene quantum dot[110], where an evolution from Coulomb blockade peaks to Landau levels is shown, the level spacing could have fluctuations due to the structural defects in the quantum dot. No etched dot exists in our sample; however, we think disorder such as structural defects could still cause fluctuations in the energy level spacing, resulting in the observation of Landau-levels-like behavior.

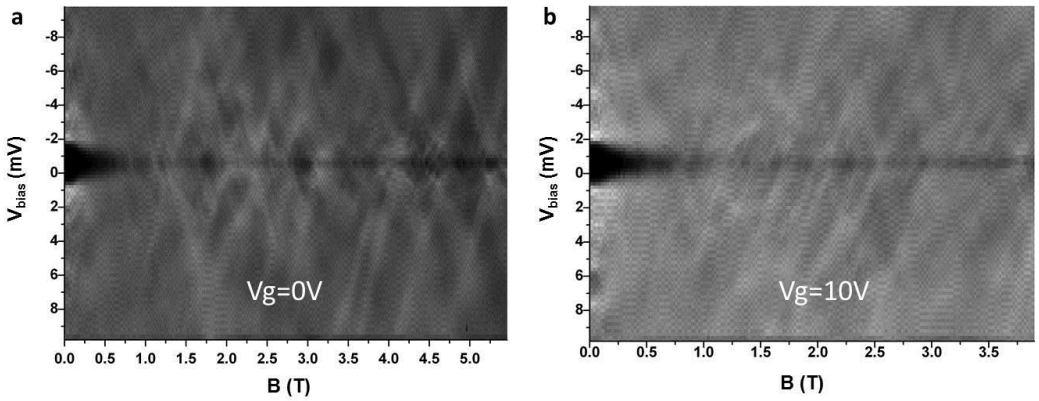

Figure 3.15. Back gate and magnetic-field dependence of tunneling spectra of sample-081212 Device A, measured from probe 7 to contact 6. 2D map of differential conductance versus dc bias voltage V_{bias} and magnetic field B, taken on different back gate voltage: (a) $V_{backgate}$ = 0 V; (b) $V_{backgate}$ = 10 V.

However, mechanism other than defects in the quantum dot should not be ruled out to explain the observed graphene-derived states. Although no strong Coulomb blockade is observed in the back gate characteristic, near zero-bias, Coulomb charging behavior is evident by diamond-like structures (in the region near zero bias in in Fig 3.8b and Fig 3.12d); in this case, the localization may occur due to interference between random scattering events within a phase coherence length[7, 111]. Another sign of localization is the crossing patterns which appear in the low bias range at zero back gate

as better shown in a higher resolution 2D plot in Fig 3.14d. Similar crossing patterns are observed in another sample as well (Fig 3.15). Similar energy levels crossing has been observed in an etched graphene quantum dot[56].

3.3.2 Localization in high magnetic field

It is instructive to compare our results to results from the STS study of exfoliated graphene on a SiO_2 substrate, for a comparison to the features we observed in Fig 3.13. These results again confirm that we can perform tunnel spectroscopy of graphene using the planar Pb tunnel probe, as the STS spectra look very similar to our data. The broader resonances are similar to the features which follow the evolution of the Dirac point at low magnetic field; in high magnetic field, the broader resonances are crossed by groups of four resonance peaks at zero bias, which come from quantum dot formed at high magnetic field. In zero magnetic field, weakly localized states are created by the substrate induced disorder potential. In strong magnetic fields, the two-dimensional electron gas breaks into a network of interacting quantum dots formed at the potential hills and valleys of the disorder potential (Fig 3.20c). The charging energy extracted from Fig 3.13d gives ~ 4.1meV and ~ 5.6 meV for two different groups. These gives a quantum dot size of ~ 150 nm in radium, comparable to the area covered by the probe. Actually many more sets of such resonance peaks show up with the increasing backgate voltage, however, the spacing between them are much smaller than 4.1 meV which indicates that localization on larger scale also exists.

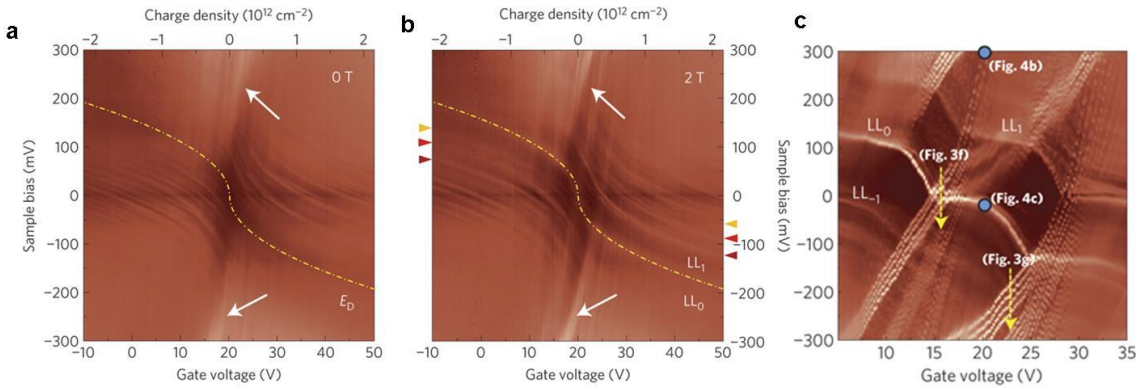

Figure 3.16 (a)(b) d*I*/d*V* gate maps taken at a fixed location as a function of sample bias and gate voltage at 0 T and 2 T, respectively. The yellow dash–dotted lines show the evolution of the Dirac point at 0 T (Landau Level peak at 2 T) as a function of gate voltage. The scattering resonances (white lines) follow the variation of the Dirac point. Broad d*I*/d*V* bands marked with white arrows in a and b are from the confinement by p–n junctions at lower magnetic fields and are evolving into a quartet of charging peaks at higher fields, as seen in c. (c) High-resolution d*I*/d*V* gate maps obtained at 8 T at the same location. This location corresponds to disorder potential minima. Those broad bands at low field have developed into sets of four peaks, which are Coulomb blockade peaks. Adapted from reference[7].

3.4 The 'Coulomb diamonds'

A triangular feature which is obviously different from the fine oscillations or the broader resonances discussed in the previous two sections appears in two different samples, as shown in Fig 3.17a, and Fig 3.19. In Fig 3.17, the feature only shows up at a particular backgate voltage, while in Fig 3.19, a series of such triangular features appear over the entire backgate voltage range of measurement. As for the bias range, it extends over 40 mV for the device shown in Fig 3.17 and about 60 mV for the other device. The outline of triangular feature is defined by a line of high conductance; inside the region defined by the triangular outline, conductance is slightly higher than the regions outside and has oscillations.

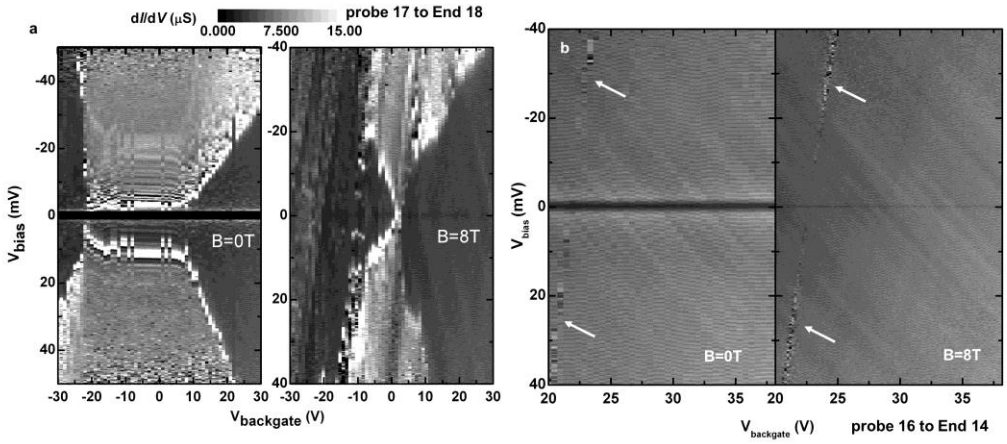

Figure 3.17. Magnetic-field dependence of tunneling spectra of sample-100812. (a) 2D map of differential conductance versus dc bias voltage V_{bias} and back gate voltage $V_{backgate}$, measured from probe 17 to end contact 18. The plot on the left (right) is taken with (without) a magnetic field of 8 T perpendicular to the plane of the sample. (b) Similar 2D maps as (b) except taken from probe 16 to end contact 14. White arrows mark the similar 'Coulomb diamonds'. (c) 2D map of differential conductance versus dc bias voltage V_{bias} and back gate voltage $V_{backgate}$, taken from probe 16 to end contact 14.

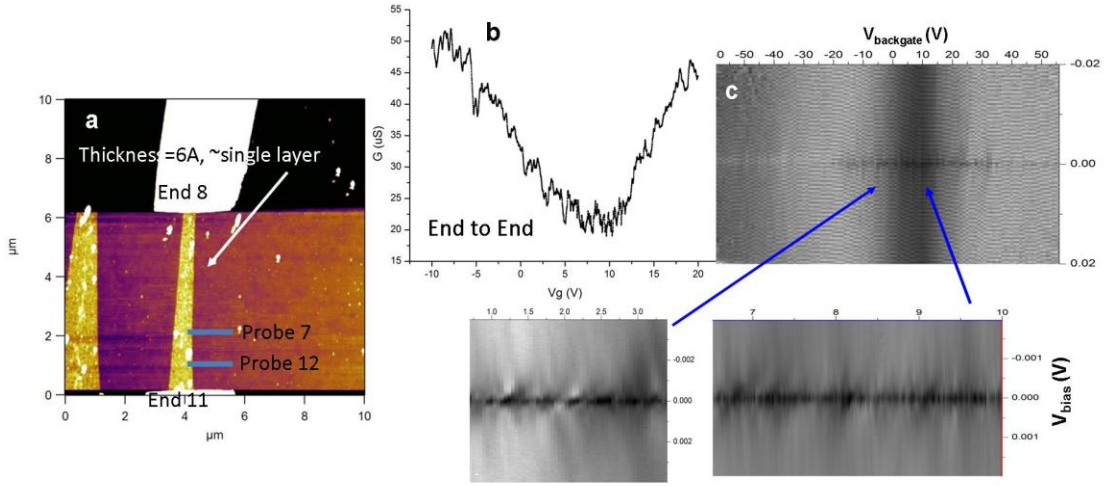

Figure 3.18. Surface characterization, back gate characterization of sample-011613. (a) AFM image of the device. (b) Differential conductance vs. back gate voltage measured from end to end contacts. (c) 2D map of differential conductance versus dc bias voltage V_{bias} and backgate voltage $V_{backgate}$, measured from end contact to end contact. The lower two 2D maps are higher resolution versions of the 2D map in regions where the back gate range is at and near Dirac point.

From the first look, especially in Fig 3.19, it is tempting to think that these are just Coulomb diamonds, which comes from quantum dot in graphene. Actually in the transport properties measured from one normal contact to other, Coulomb blockade does

show up as can be seen in the 2D conductance map, Fig 3.18c. If these are Coulomb diamonds, the charging energy is roughly 60 meV (Fig 3.19), that would correspond to a quantum dot of size ~ 15 nm in radium. For the device shown in Fig 3.17a, it is a little hard to extract the charging energy, since no complete Coulomb diamonds can be found. In this device, these 'diamonds' could extend to a much larger bias and backgate range, which is beyond our measurement regime, suggesting a much smaller size of quantum dot if the Coulomb blockade picture is applicable.

However, if we compare these 'Coulomb diamonds' taken with different magnetic fields in Fig 3.19, we find some 'diamonds' start to show a curved outline as the magnetic field increases. In addition, the line features inside the 'diamond', which correspond to the excited states in the Coulomb blockade picture and start as straight lines at zero magnetic field, become staircase-like curves as the magnetic field increases as well. These changes are not expected; in fact, it has been observed in etched graphene quantum dot that the Coulomb diamonds stay well preserved for high magnetic field (no such change of shape in either the diamond outline or the excited states, as shown in Fig 3.20)[98]. The charging energy in our 'diamond' is about twice as much as the etched graphene dot, which indicates that the size of localized region should be about one half. The electronic orbits should be more confined in our cases and thus Landau level behavior should have a lower probability to form.

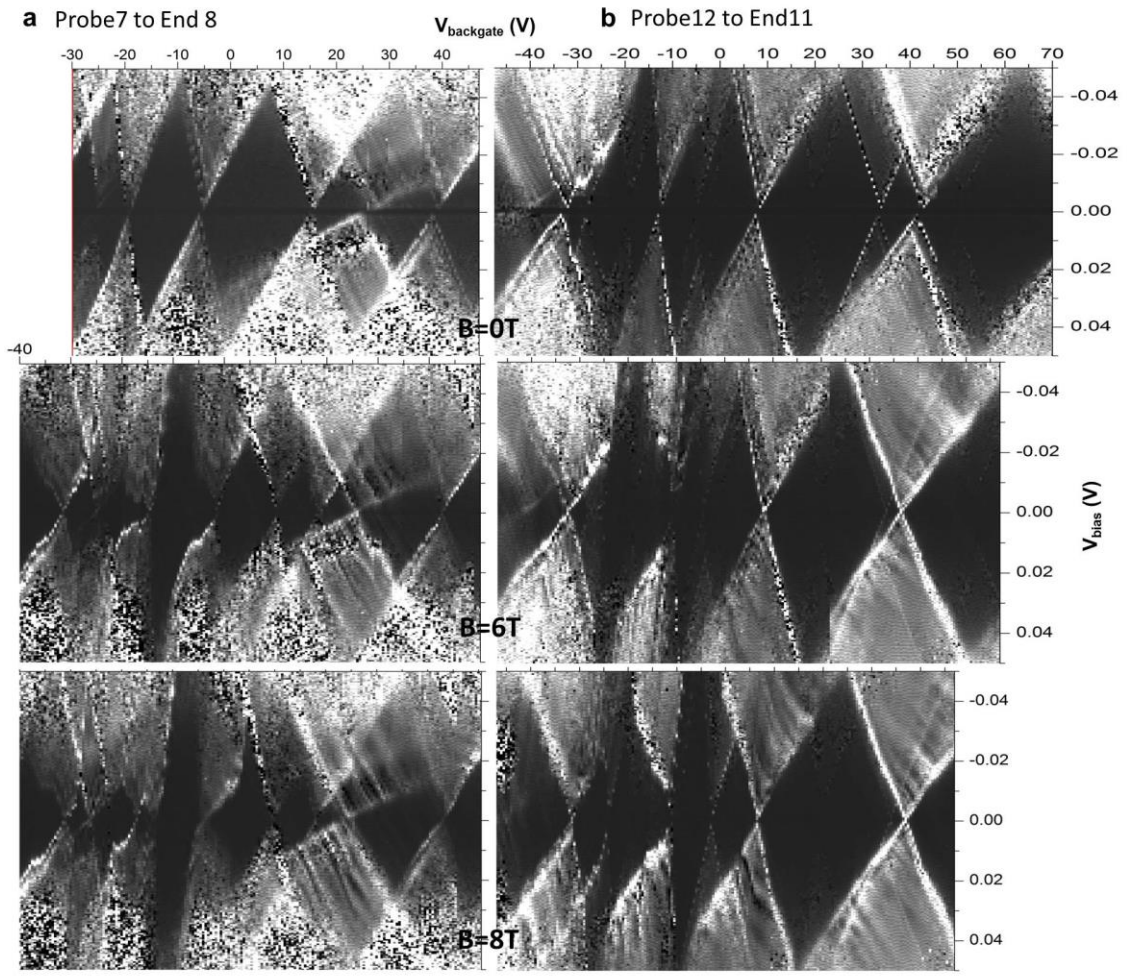

Figure 3.19. Magnetic-field dependence of tunneling spectra of sample-011613. (a) Magnetic field dependence of 2D map of differential conductance versus dc bias voltage V_{bias} and backgate voltage $V_{backgate}$, measured from probe 7 to end contact 8. The first row is taken without magnetic field, the second row with a magnetic field B = 6 T and third row with B = 8 T. The B field is perpendicular to the plane of the sample. (b) Similar 2D map as (a) except taken from probe 12 to end contact 11.

Another observation against the Coulomb blockade picture is that these triangles always appear as a set of two which have symmetry with respect to the point where the triangle meets at zero bias. Also, different sets of such diamonds can overlap and do not interfere with each other. In the Coulomb blockade picture, however, one diamond would not appear inside the blockaded region of another. If there are multiple quantum dots in series, diamonds can overlap but the blockaded regions would dominate; if one dot in

series is very well coupled to the contacts, it can interact with other dot to form beat pattern[70]. None of these is consistent with the 'diamond' features we observed here.

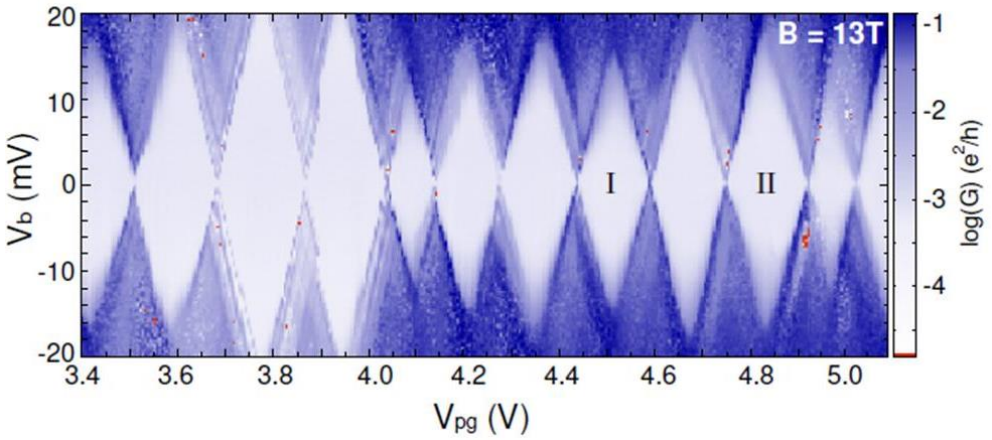

Fig 3.20 Coulomb blockade resonances of a 50 nm wide and 80 nm long quantum dot in graphene at B = 13 T. These measurements are taken at constant back gate voltage and show single dot signatures at high magnetic field. The Coulomb diamonds are well preserved at high magnetic field. Adapted from reference[98].

As we mentioned earlier, inside these triangles, the conductance is not only high but also has a strong oscillation. This observation actually leads us to think that the two lines marked by white arrows in Fig 3.17be are of the same origin due to the similar conductance oscillation and the symmetry. The triangular features in Fig 3.17a and 3.17b are not as regular as those 'diamonds' in Fig 3.19 and could be just a sample-dependent special case. We find the relative flat region, as if the diamond is stretched, can be related to the platform region in the back gate characteristic from V_{backgate} -20V ~ 20V shown in Fig 3.10b.

Based on the discussions above, although we do not have a good idea of what these 'diamonds' are, we do find some clues which support that they are not Coulomb diamonds, at least not from a quantum dot formed in etched graphene nanostructures.

3.5 Conclusion and discussion

We summarize the signatures of these features observed in the tunneling spectrum of graphene via a planar Pb probe in Table 3.1. The fine oscillations could be superconductivity-related, originating from quasiparticle interference or phonons. In the broader resonances, we observe Landau level like behavior, likely due to the electron orbital being confined by disorder-induced puddles. The four-fold resonance peaks, similar to what has been observed in STS studies, indicates localization in high magnetic field and are also consistent with the disorder potential picture. This observation also supports the fact that the planar probes are in the tunnel regime and can perform tunneling spectroscopy. In addition, with (out) a magnetic field (~ 1T), we can perform tunnel spectroscopy in the normal (superconducting) regime. The 'Coulomb diamond' we observed is different from the quantum dot behavior observed in etched quantum dot, which leaves whether they are really quantum dot-related or not an open question. Although the pictures we have about these features are not clear, these analyses are a starting point. Further surface characterization of the interface between graphene and the Pb probe, such as transmission electron microcopy, could provide useful information.

	Devices	Bias Range	Slope	Symmetry	Backgate dependence	Magnetic field dependence
The Fine oscillations	All devices measured	0~5mV, mostly; 0~10mV for some	Negative	Asymmetry due to asymmetric coupling of the two contact	Irregularities only depend on the probe; slope has no significant dependence	Disappear @0.2T
The Broader Resonances	All devices measured	0~40mV	Negative	Same as above	Slope value decreases as the Fermi level moves away from the Dirac point in some devices	As B increases, staircase like curve start to show; the distance between resonances increases
The 'Coulomb Diamonds'	Two devices	0~60mV (could be even higher)	Both negative and positive	Symmetric with respect to the crossing point at zero bias	in one devices, only appear near Dirac point; in the other device, appear in a large backgate range	A conductance suppressed band near the Dirac point appear; for some 'diamond', the outlines and the resonances peaks inside the 'diamond' turn from straight lines to staircase like curve

Table 3.1 Summary of features observed in the tunneling spectra (the 2D map of differential conductance as a function of backgate voltage and bias voltage) of seven graphene devices using planar Pb probe

Chapter 4: Andreev Bound States in Graphene Nanostructures

4.1 Introduction

4.1.1 ABS in graphene-based devices

Andreev bound states have been observed in hybrid system(s) made from a planar superconductor probe and either graphene,[32] carbon nanotubes[112], or semiconductor quantum dots[50]. Transport measurements of sharp, gate-tunable ABS formed in a superconductor–quantum dot–normal metal system was previously realized in our group on an exfoliated graphene sheet. Figure 4.1c shows a two-dimensional map of conductance versus bias and gate voltage for the graphene-Pb probe device shown in Fig 4.1a. The lowest-energy subgap peaks show a striking gate- and bias-voltage-dependent pattern. This pattern can be qualitatively explained as resonant transport through ABS levels (see Fig. 4.1b for a schematic diagram); the levels can be calculated from a simple phenomenological model and quantitatively fitted with detailed transport calculations, as shown in Fig. 4.1b. The subgap peaks in tunneling conductance are the signatures of ABS in a quantum dot.

The appearance of subgap conductance peaks requires the domination of the charging energy (U) compared to the effective superconducting pairing (Δ_{eff}). If $U << \Delta_{eff}$, Cooper pairs form on levels within gap and conductance are suppressed. When $U >> \Delta_{eff}$, the spin-up and down states are widely split in energy, and ABS are formed from the discrete quantum dot states, owing to Andreev reflections at the

superconductor–quantum dot interface. A phenomenological model that considers the effect of the superconducting proximity coupling on a single pair of spin-split quantum dot states explains the lowest-energy ABS physics. The effective Hamiltonian for a proximity-coupled quantum dot is

$$H = (\varepsilon_{\uparrow} - E_{\text{shift}})c_{\uparrow}^{\dagger}c_{\uparrow} + (\varepsilon_{\uparrow} + U - E_{\text{shift}})c_{\downarrow}^{\dagger}c_{\downarrow} + \Delta_{\text{eff}}c_{\downarrow}^{\dagger}c_{\uparrow}^{\dagger} + \Delta_{\text{eff}}{}^{*}c_{\uparrow}c_{\downarrow} \quad (7)$$

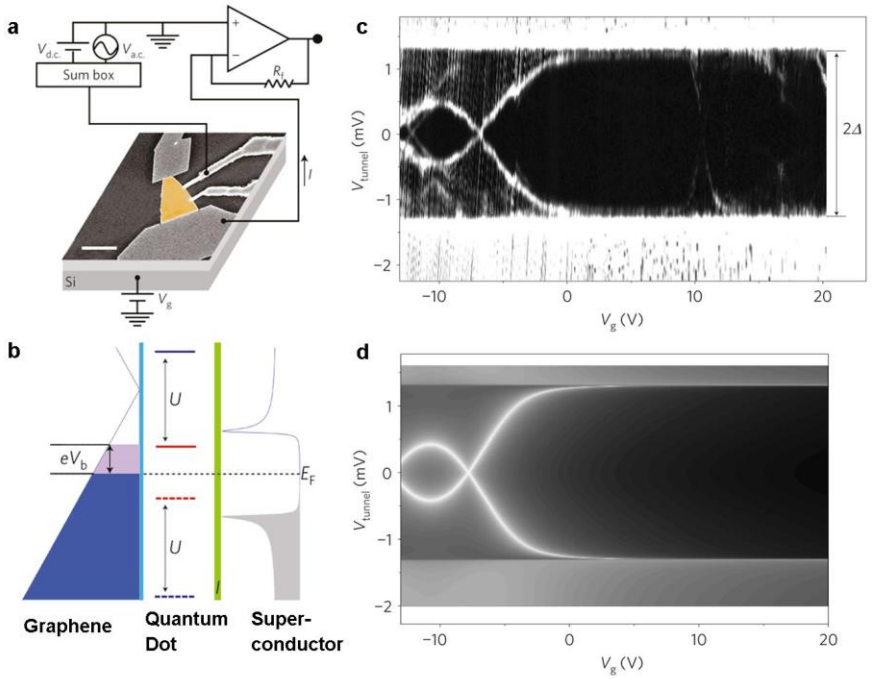

Figure 4.1 ABS observed in graphene-superconductor hybrid device. (a) Scanning electron micrograph of a device with an overlaid measurement circuit. Graphene is false coloured orange, large end contacts are Cr/Au and middle tunnel probes are Pb/In. The scale bar is 5 μm. (b) Schematic energy-level diagram of the graphene–quantum dot–superconductor system. The density of states of graphene and superconductor tunnel probe is shown on the left and right, respectively, with filled states indicated. The tunnel barrier is indicated in green on the right and the other tunnel barrier is indicated in light blue on the left. Blue/red energy levels refer to Andreev bound states. The solid (dashed) lines represent states that have dominant particle (hole) character. The bias voltage, V_b, is shown tuned to enable resonant subgap conduction. (c) Two-dimensional map of tunnelling differential conductance versus back-gate voltage (x axis) and bias voltage (y axis) on a log scale for the single-layer device. Bright white lines inside the gap (marked as 2Δ) are subgap peaks, or ABS, which are symmetric about zero bias and gate dependent. (d) A fit of the conductance data from the detailed transport calculations for a quantum dot with two levels, a finite charging energy and couplings to normal-metal and superconducting leads. Adapted from reference[32].

where E_{shift} represents the shift of the quantum dot energy levels by the gate voltage, $\varepsilon_{\uparrow}$,$\varepsilon_{\uparrow}+U$ are the energies of the spin-split levels (we could equivalently choose $\varepsilon_{\downarrow}$,$\varepsilon_{\downarrow}+U$) and c_{σ} ($c_{\sigma}^{\dagger}$) are creation (annihilation) fermionic operators having spin $\sigma=\uparrow,\downarrow$. Resonant transport through the ABS levels leads to the observed subgap conductance peaks. ABS energy depends on charging energy U, single particle energy e, gate voltage E_{gate}: $E_{\pm}=1/2\left(\pm U+\sqrt{4\Delta_{\text{eff}}{}^{2}+\left(2\varepsilon_{\uparrow}-2E_{\text{shift}}+U\right)^{2}}\right)$. We will use the simulation[‡] based on this model when we discuss under what condition ABS can be observed in graphene nanostructure.

ABS have been observed in the tunneling spectroscopy of graphene-Pb hybrid devices[32]. However, the absence of ABS in most devices studied in chapter 3 raises the question of the condition under which Andreev bound states can be observed in the graphene-based devices, which we will try to answer in this chapter.

4.1.2 ABS in graphene nanostructure devices

As we discussed in the previous section, spin-split energy levels are needed to support ABS in a quantum dot system. Nanostructures in graphene have shown quantum dot behavior which can be controlled by gating and confinement[53]. As a matter of fact, much more can be expected in hybrid nanostructures: hybrid devices of quantum dots and superconductors exhibit rich physics, such as Coulomb blockade[113], the Kondo effect[114-116], the Josephson effect[117, 118] and Andreev bound states (ABS)[32, 42, 50, 112], due to the competition between the single electron transport typical of quantum dots, and the electronic pairing interactions of superconductors. The different behaviors of these hybrid

[‡] See appendix for more details. Source code, courtesy of Taylor Hughes

devices are known to depend on the device geometry and the coupling between the quantum dot and the superconductor, yet questions remain about the conditions under which each behavior appears.

In this chapter, we discuss the conditions under which Coulomb blockade, proximity effects, and ABS appear in superconductor-graphene nanostructures. We put superconductor probes on top of graphene nano-constrictions of two different widths (200 nm and 10 nm). Different transport gaps, bias gaps and transparency[119] have been observed in nano-constrictions of different widths; however, how they interact with a superconducting tunnel probe hasn't been explored. We measure the transport properties through the constriction as well as the tunneling spectroscopy from the probe to the constriction and observe strong Coulomb blockade in the transport through the wide constriction (200 nm wide) while not fully-suppressed blockade in the narrow one (10 nm wide). In contrast, ABS features are seen in the tunneling spectroscopy only in the narrow constriction, not in the wider one. This behavior can be explained by the difference in the coupling strength between constrictions of different widths and the normal leads (compared to contact coupling at the Pb-graphene constriction interface): the localized states in the narrow constriction have a better coupling to the normal leads than the wide constriction. This relative difference in coupling could be further explained within the picture of quantum dots formed in the disorder potential, where the narrow constriction size is smaller than the characteristic disorder length and thus allows better coupling. Our findings stress the importance of the relative coupling between quantum dots and contacts for the observation of ABS.

4.2 Device fabrication and characterization

Graphene nano-constrictions are fabricated using commercially available crystals of graphite, from which thin layers were mechanically exfoliated[2] onto a Si substrate with 300nm SiO_2, which serves as the back gate capacitor. The devices described in the chapter are made from multi-layer graphene. The sample is patterned into nano-constrictions of two different widths (200 nm and 10 nm), as can be seen in Fig 4.2a and Fig 4.2b, using electron beam lithography and reactive ion etching with oxygen. Source and drain leads (4 nm Ti/50 nm Au) are fabricated via one electron beam lithography step while the Pb probe (200 nm Pb/30 nm In) is made via another. In terms of contact transparency, the Pb probe can act as a tunneling probe because an oxide layer can form at the interface[120]. However, the coupling between the nano-constriction and the Pb probe studied in this chapter are not oxidized for a long time, which means the barrier is not in the strong tunnel regime and thus Andreev reflection can happen. Micrographs of the nano-constrictions and the final devices are shown in Fig 4.2a and Fig 4.2b respectively.

We need to point out that when we first try to make these graphene nano-contrictions, the most narrow and thus weakest part in the constriction always breaks. We think it could be due to the fact that we were using large pieces (~ 20 μm) of graphene, and the two large pieces left on each side of the constriction (used as the connecting leads) tend to tear apart the weak link. After we switched to using smaller pieces, this problem was solved. For graphene grown by chemical vapor deposition, the situation could be different, as there the surface adhesion is not as strong as in the exfoliated case due to the wet transfer process.

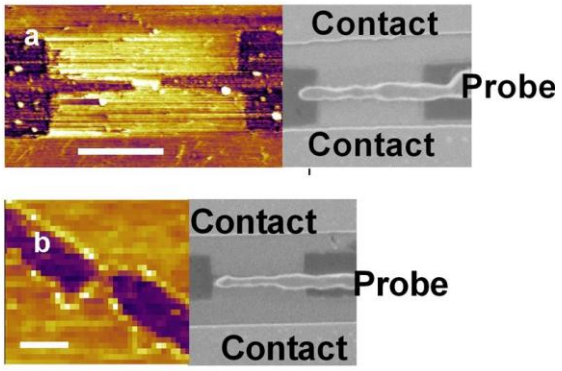

Figure 4.2. Surface characterization of the 10 nm and the 200 nm wide graphene nano-constriction. (a) Left: an AFM image in height of the 200nm wide nano-constriction, scale bar is 1 μm. Right: an SEM image of finished device with source and drain contacts and a Pb probe on top the constriction. (b) Left: an AFM image in height of the 10nm wide nano-constriction, scale bar is 10nm. Right: an SEM image of the finished device with source and drain contacts and Pb probe on top of the constriction.

4.3 Coulomb blockade and superconducting proximity effect in graphene nano-constriction

Coulomb blockade, a signature feature of quantum dot behavior previously reported in graphene nanoribbons[121-123] and nano-constrictions[124-126], which could originate from the disordered potential or the edge roughness, is observed in our 200 nm wide constriction. In the transport measurement from one normal contact to the other, Coulomb blockade is evident by the suppressed conductance and the conductance oscillations as shown in Fig 4.3 and the Coulomb diamonds in Fig 4.3. We also notice the complete suppression of the conductance through the 200 nm wide constriction without a magnetic field as can be seen in Fig 4.4a: without the magnetic field, there is a zero conductance gap region coming from the superconducting density of states of Pb, with the expected gap $2\Delta=2.6$ meV, which breaks the Coulomb diamonds into two parts. With a 0.5 T magnetic field applied perpendicular to plane of the device, the zero conductance

gap goes away and complete Coulomb diamonds are clearly visible as shown in Fig 4.4b. This zero conductance gap is due to an energy gap induced in the graphene[31] constriction by the Pb probe on top and is a manifest of the superconducting proximity effect.

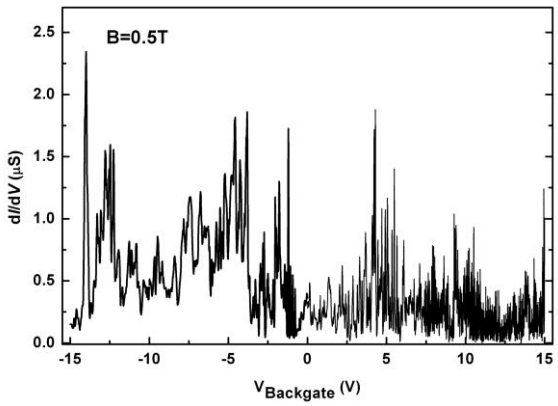

Figure 4.3. Coulomb blockade in the 200 nm wide graphene nano-constriction: differential conductance (measured from contact to contact with an ac bias 0.02 mV) versus back gate voltage.

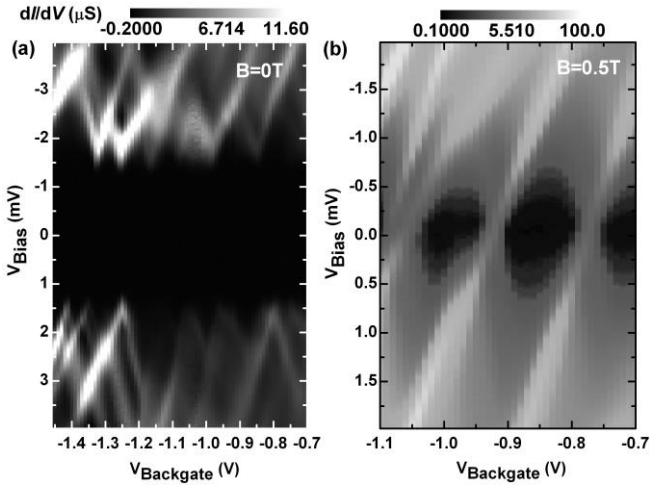

Figure 4.4. Coulomb blockade in the 200 nm wide Graphene nano-constriction: (a) 2D map of differential conductance (measured from contact to contact) versus backgate and bias voltage with zero magnetic field. Coulomb diamonds are separated by a superconducting gap induced by the Pb probe on top. (b) Similar 2D map as (a) except with a magnetic field 0.5 T to lift the superconducting proximity effect.

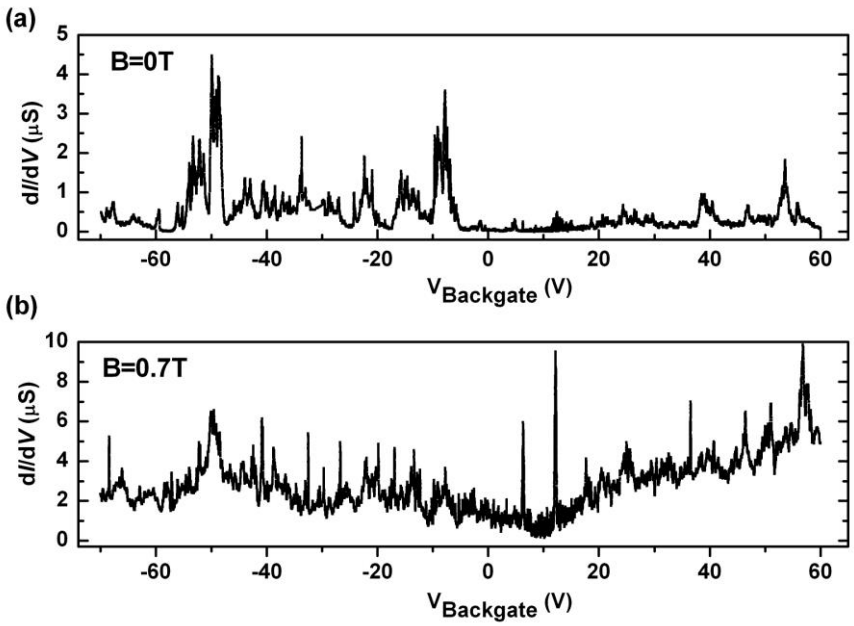

Figure 4.5. Backgate characterization of the 10 nm wide graphene nano-constriction: (a) Differential conductance (measured from contact to contact) versus back gate voltage. (b) Similar to (a) except with a magnetic field 0.7 T.

Proximity effect is also observed in the 10 nm wide constriction. It is evident by the conductance suppression in the back gate characteristic without a magnetic field compared to the one with a magnetic field (Fig 4.5a and Fig 4.5b). However, the suppression is not as complete as in the 200 nm wide constriction, which is evident by the non-zero conductance in Fig 4.5a. This difference in the strength of the proximity effect could have something to do with the different coupling between the constriction and the normal leads, which exist in constrictions with different widths as we will discuss later in detail in this chapter. However, the fact that Coulomb blockade peaks in a carbon nanotube quantum dot are not affected by the Pb probe on top[113] indicates that bad coupling is not sufficient to explain the zero conductance gap only observed in the 200 nm wide constriction. In the carbon nanotube quantum dot, the coupling between the quantum dot and the normal contact is bad, evident by the strong Coulomb blockade, but transport through the quantum dot is not completely suppressed, evident by the Coulomb

peaks. Intuitively we think it is because the wider constriction has a larger contact area with the superconductor probe and thus it is likely to have a stronger proximity effect.

Coulomb blockade behavior in the 10 nm wide constriction is also different from the 200 nm wide one: there is no fully-suppressed conductance region in the back gate characteristic as can be seen by comparing Fig 4.3 and Fig 4.5b. As a matter of fact, the 10 nm constriction has a higher conductance through than the wide one overall, which suggests a better coupling to the leads in the 10 nm wide constriction. Although a large confinement energy gap is expected for a narrow constriction, better coupling between the constriction and the leads could arise if the size of the constriction is smaller than the disorder characteristic length. Given that the typical electron-hole puddle size is 30 nm[11], the 10 nm wide constriction is closer to an open rather than isolated quantum dot(s). This is consistent with previous findings that short constriction can act as a tunable tunneling barrier[124]. Although the conductance is suppressed not as strongly as in the wide constriction, Coulomb diamonds are still visible in the 10 nm constriction near the Dirac point where V_{backgate} ~ 10 V in Fig 4.6d. When the Fermi level moves away from the Dirac point, the conductance is even less suppressed, which indicates the coupling between the constriction and the leads increases[124] (Fig 4.6a,c). These changes in the Coulomb blockade behavior with the Femi level support the picture of quantum dots formed due to the disorder potential, where the localization behavior is stronger near the Dirac point.

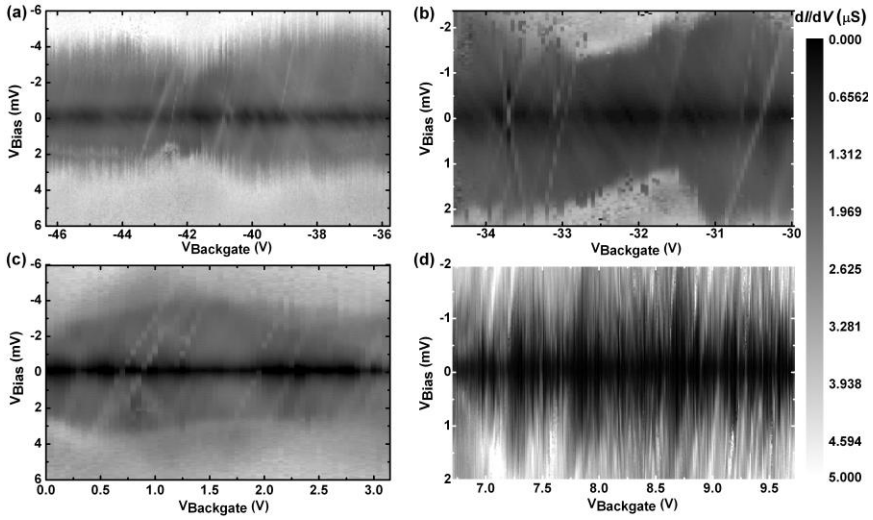

Figure 4.6. Coulomb blockade in the 10 nm wide graphene nano-constriction: 2D map of differential conductance (transport through contact to contact) versus backgate and bias voltage with no magnetic field at four different backgate ranges. (a)(b)(c) in the hole-doped region, Coulomb blockade with not-fully-suppressed conductance inside the diamonds. (d) Stronger blockaded Coulomb diamonds near the Dirac point.

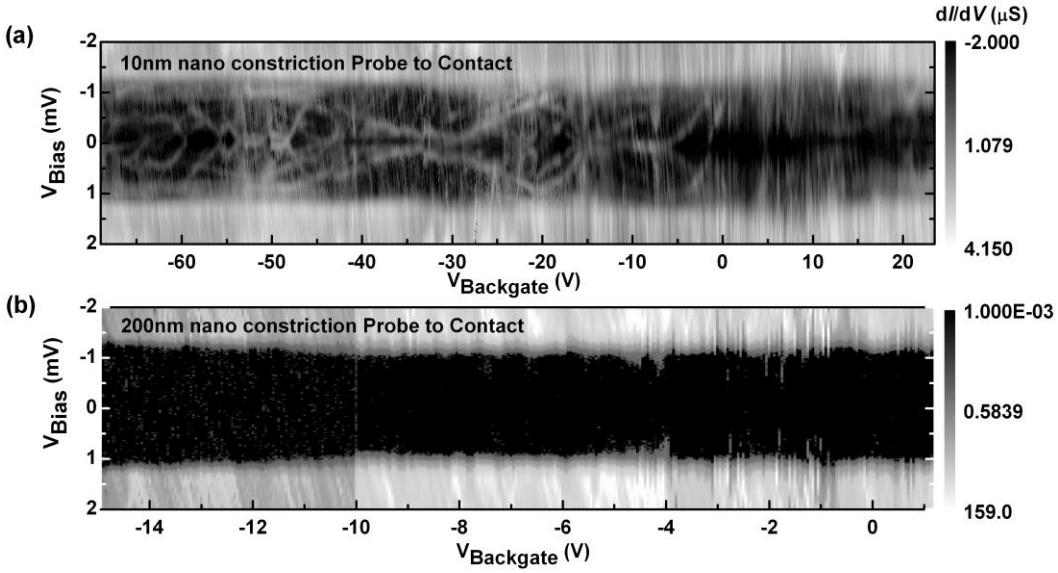

Figure 4.7. Andreev bound states observed in the 10 nm wide nano-constriction, not in the 200 nm wide constriction. (a) 2D map of differential conductance (measured from probe to contact) versus backgate and bias voltage for the 10nm-wide constriction. Features inside the superconducting gap come from ABS. (b) Similar 2D map as (a) for the 200 nm wide constriction.

In the tunneling spectrum measured from the Pb probe to the normal contact as shown in Fig 4.7, ABS is only observed in the 10 nm wide constriction while no features

appear inside the superconducting gap in the 200 nm wide constriction. This could also be understood by the difference in the coupling between the constriction and the normal leads.

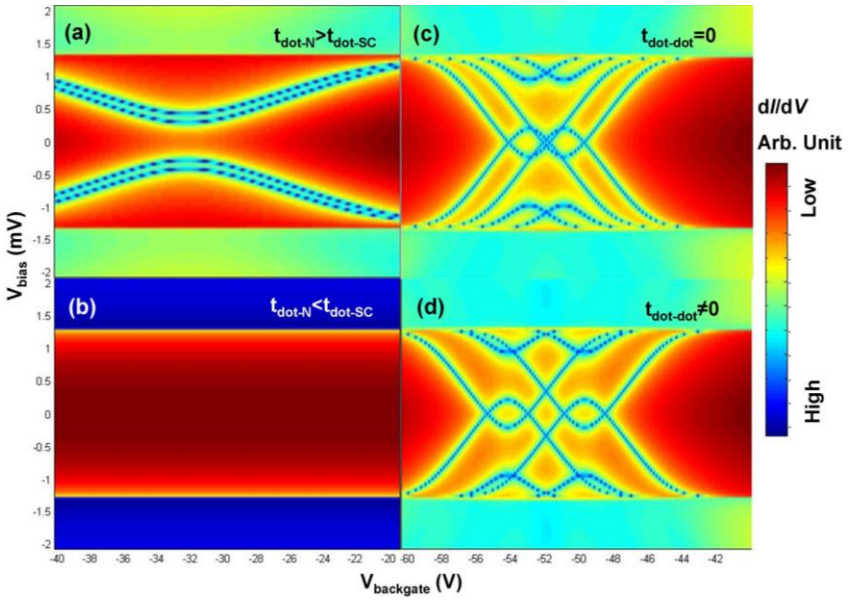

Figure 4.8. Simulated 2D maps of differential conductance (from the Pb probe to the normal lead) versus bias and back gate voltage based on a normal lead-quantum dot-superconductor lead model. (a) Single quantum dot with the coupling between the superconducting lead and the dot level bigger than the coupling between the normal lead and the dot. Features inside the superconducting gap come from Andreev Bound states. (b) Similar simulation as (a) except the values of the two coupling parameters t_{dot-SC}, t_{dot-N} are exchanged. No ABS feature shows up inside the superconducting gap. (c) Simulation with two quantum dots with no coupling between these two dots. It basically is equivalent to the simple superposition of ABS from two single quantum dot. (d) Similar simulation as (c) except the coupling between these two quantum dot levels is turned on. Compared to (c), the ABS features become more spread out.

This point is confirmed by a comparison of simulations (see details of the simulation in the supplementary material of ref[32] and see the source code in the appendix) using different coupling strength between the quantum dot energy levels and the normal leads (denoted by t_{dot-N}) and between the quantum dot energy levels and the superconductor (denoted by t_{dot-SC}). The simulated data is shown in Fig 4.8a and 4.8b, the values of two coupling strength (t_{dot-N}, t_{dot-SC}) is switched while all the other parameters

are kept the same in the calculation. As can be clearly seen in this simulation, when $t_{dot-N} > t_{dot-SC}$, ABS is observable while when $t_{dot-SC} > t_{dot-N}$, ABS is not seen. We need to point out that different coupling at the two interfaces of the quantum dot is not the only factor which could affect the observation of ABS. However, from our observations, this is consistent with the difference in the Coulomb blockade behaviors of constrictions with different widths.

4.4 ABS in graphene nano-constriction

Compared to the previously reported ABS features which are based on one set of spin split energy levels[32], the features observed in the 10 nm wide graphene nano-constriction are more complicated. As can be seen in Fig 5, near the Dirac point, $V_{backgate}$ ~ 10 V, the ABS peaks are barely observable and the peak intensity (which reflects the conductance value) is low. In the hole-doped gate region, the ABS peaks become more clear and profound. Weak coupling to the normal lead can make ABS features less visible, which again can be seen from the comparison of simulated data with different coupling parameters in Fig 6a and 6b. This is consistent with the different Coulomb blockade behaviors seen in the transport through the constriction in the corresponding back gate ranges (strong blockade near the Dirac point, Fig 4d, and not as suppressed away from Dirac point, Fig 4a,b,c). In addition, there are multiple sets of ABS, coming from multiple localized states, which appear in different back gate ranges and thus could be spread out in the energy space. Some sets of the ABS features expand over a large gate range, while others only a small range, which indicates that these localized states have different capacitance environments and thus could be distributed at different physical

locations as well. Some sets of ABS features overlap, while some try to avoid each other (near $V_{\text{backgate}} \sim 55$ V). This difference comes from the interaction between different quantum dots: the ABS features can overlap if there is no or very weak coupling between the localized states while with the strong coupling ABS tend to avoid each other. A comparison of the simulated ABS data based on two quantum dots with different coupling between them is shown in Fig 4.8c and 4.8d.

4.5 Conclusion and discussion

In conclusion, we have measured the transport properties through graphene nano-constrictions of two different widths and the tunneling spectroscopy via a superconducting probe on top of these constrictions. Coulomb blockade and superconducting proximity effect are observed in both constrictions, with a difference in strength. However, ABS is observed only in the narrow (10 nm wide) constriction, which is due to the better coupling between the narrow constriction and the normal leads compared to the wide constriction. This can be understood by the localization induced by the disorder potential, where the better coupling in the narrow constriction originates from the size of the constriction being smaller than the characteristic length of potential disorder. Within this picture, the observation of ABS in the narrow constriction is consistent with the difference in the Coulomb blockade behaviors. We also discuss the complex ABS features observed in the narrow constrictions, which may help better understand the localization behavior in these nanostructures. Our observations stress the importance of the coupling at the interfaces for the observation of ABS in graphene

nanostructures, which may be helpful in making quantum computation devices based on these hybrid structures.

As confirmed by the results in this chapter, experimentally, observation of ABS needs the support of localized energy states, which is supplied by the quantum dot formed in disorder potential in graphene nanostructure. The absence of ABS in the wide constriction tells us that the discrete energy levels needs to have a stronger coupling to the normal contact compared to superconductor. Missing one of these conditions results in the absence of ABS. This is helpful in understanding the situation of graphene-Pb devices. We note two differences in the fabrication process which could give rise to the formation of the quantum dot. One is atomic layer deposition (ALD) which results in Al_2O_3 nanoparticles deposited along edges and at defect sites of graphene[89]. Nanoparticles may hybridize with graphene edges or defects, forming localized quantum dots. Our initial graphene-superconductor devices had an ALD layer, and thus typically exhibited ABS, even for large samples having no constrictions. However, since we realized Pb could form oxide at the Pb-graphene interface, the ALD grown oxide is not necessary for making a tunnel barrier and thus stopped using this fabrication process. The other difference is that previously ozone etching was used to clean the graphene surface before metalizing the probe in most device fabrication. This process was removed as well in our later studies because ozone etching causes damage to graphene. It is a reasonable explanation that ozone etching creates some defects which can supply the localized states to support ABS.

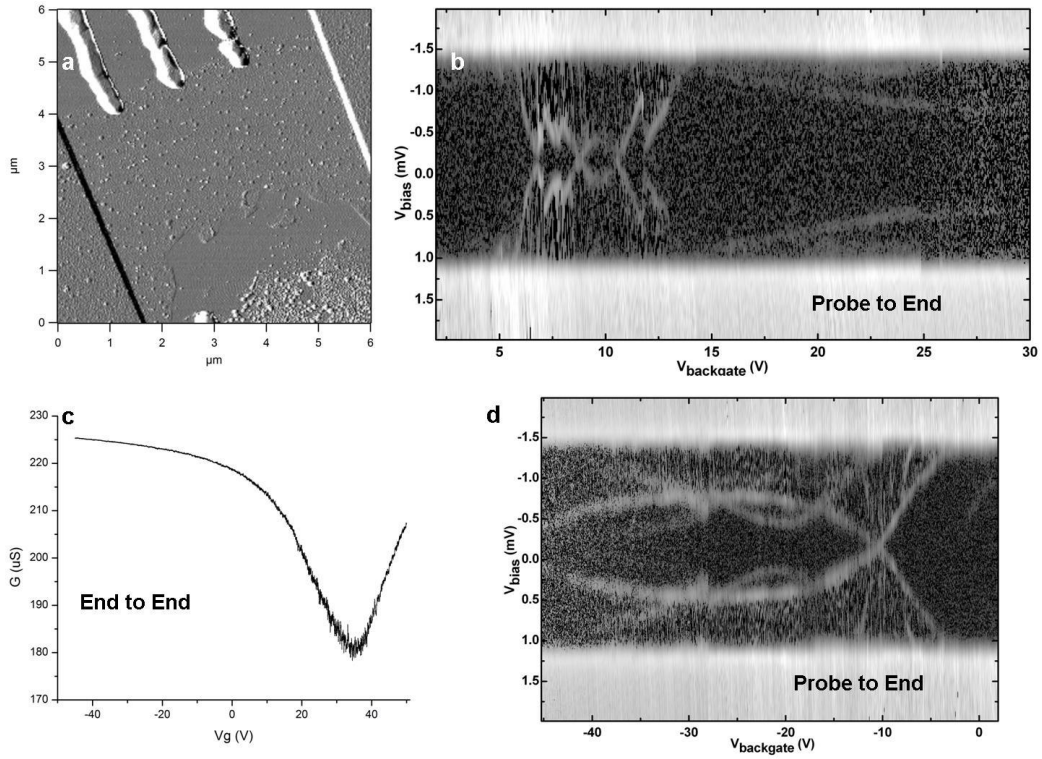

Figure 4.9. Tunneling spectra of Sample_060711_1. (a) SEM image of the sample where the graphene piece connecting to the right lead is electrically shocked by current leaving only a ribbon connecting the probe to the left lead (the probe measured is at the bottom). (b) 2D map of differential conductance vs backgate and bias measured from probe to end. ABS features are observable as the white curves inside the superconducting gap. (c) Backgate characteristic of end to end conductance showing the Dirac point near backgate voltage 35V. (d) Similar 2D map as (b) showing a different backgate range.

We need to point out that in one particular sample, which was not cleaned via ozone etching (Fig 3.11) or processed via atomic layer deposition, ABS was observed after a thermal cycle. Defects could be developed in the Pb tunnel barrier after thermal cycles, which can support localized states. We have also included data taken from a graphene sample which is electrically shocked into a nanoribbon geometry, where ABS is also observed as shown in Fig 4.9. The signatures of ABS are not as complex as those observed in the etched nano-constriction; however, this way of making nanostructure is not repeatable or controllable.

Chapter 5: Transport in a MoS_2 nanostructure

5.1 Introduction

We extend our study of nanostructures from graphene to MoS_2, which can be exfoliated into two-dimensional layers of single unit cell thickness as well. As we mentioned in the introduction, although the transition metal dichalcogenide molybdenum disulfide (MoS_2) has been studied for decades[127, 128], thin layer MoS_2 has been extensively studied only recently and little has been explored in its nanostructures. By making materials not only thinner but also narrower, significant confinement effects as well as other quantum properties are expected to appear. For example, samples with confinement on a mesoscopic scale may exhibit Coulomb blockade or Fabry-Perot oscillations, which depend on the contact transparency and mean free path, and which provide information about coherent transport that could be useful in quantum device applications[129]. In addition to ballistic transport properties, disorder-induced localization plays an important role in materials having confinement on a mesoscopic scale[130]; thus, understanding the effect of disorder on transport is crucial to scaling down and utilizing nanodevices. An advantage of studying nanoribbons is accessing this interplay between phase coherence, environmental disorder and mean free path. Beyond this, rich physics and applications have been predicted specifically for MoS_2 nanoribbons, such as band gap modification, ferromagnetism, and metal-insulator transition tuning with a transverse electric field[131]. However, while the electronic properties of thin layers of MoS_2[132] have

been studied via transport, the properties of MoS_2 with geometry confinement have not been well-studied, particularly at low temperatures where quantum effects are relevant. Here, for the first time, we demonstrate the transport properties of a MoS_2 nanoribbon device at low temperature. We observe a gate-tunable transition from Coulomb blockade to resonant transmission, where the transition point occurs when the entire nanoribbon acts as a quantum dot. Our observations show that mesoscopic confinement effects can dominate transport in these small structures. The results also reveal the length and energy scales at which quasi-ballistic versus disorder-scattering behavior determines the transport.

5.2 Device fabrication and characterization

MoS_2 nanoribbons were fabricated using commercially available crystals of molybdenite (SPI Supplies Brand Moly Disulfide), from which thin layers of MoS_2 were mechanically exfoliated[2] onto a Si substrate with 300 nm SiO_2, which serves as the back gate capacitor. The device described in this chapter has a thickness of 1.1 nm, which corresponds to a bilayer[78]. The sample is patterned into a nanoribbon (500 nm length and 200 nm width, as can be seen in Fig. 5.1a) and a sidegate, using electron beam lithography and reactive ion etching (RIE) with oxygen. Although there are multiple methods for making nanostructures in MoS_2[133, 134], we find that oxygen-based RIE does not etch the substrate and thus avoids the problem of gate leakage[135]. Source and drain leads (35 nm Ti/10 nm Au) are fabricated via another electron beam lithography and evaporation step. Micrographs of the constriction and the final device are shown in Fig. 5.1.

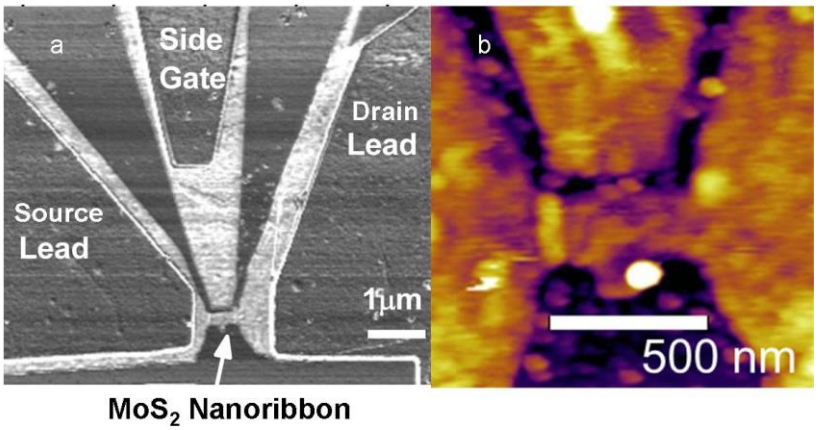

Figure 5.1 AFM images of the MoS_2 nanoribbon. (a) AFM phase image of the device, showing the MoS_2 nanoribbon, source and drain leads, and the side gate. (b) AFM height image of the nanoribbon.

The recipe to etch MoS_2 is almost the same as that for graphene, except adding one to two seconds for each layer. Here the experimental difficulty is making Ohmic contacts. We have tried several different materials as the contact. Ti/Au can make contacts relatively consistent but with high contact resistance (~ 100 MΩ) not usable for low temperature measurement. Au contact is the only one which can give a resistance on the order of a few MΩ. We need to point out that keeping samples in vacuum (which is the way most transistor studies are done) could make a big difference in terms of increasing mobility and lower disorder scattering.

5.3 Coulomb blockade in the MoS_2 nanoribbon

The dc conductance of the nanoribbon, as a function of backgate potential at room temperature, shows characteristic behavior of an *n*-doped semiconductor, as shown in Fig 5.2. If we assume Ohmic contacts (which allows us to estimate a lower-bound for mobility), we find that the nanoribbon has a field effect mobility ~ 0.127 cm^2/Vs, using $\mu = [dI_{ds}/dV_{backgate}] \times [L/(WC_gV_{ds})]$, where I_{ds} is the drain current, $V_{backgate}$ is the gate

voltage, C_g is capacitance per unit area of 300 nm thick SiO_2 (12 nF/cm^2), V_{ds} is the drain voltage, and L and W are the length and width of sample, respectively. This is consistent with typical mobility in MoS_2 of 0.1 ~ 10 cm^2/Vs [78, 136, 137], although high temperature annealing and keeping the sample in high vacuum can yield much higher mobility (60 ~ 500 cm^2/Vs)[138, 139]. The mobility for the nanoribbon is thus reasonable—given that it is unencapsulated, not annealed and exposed to ambient—and can be considered a lower bound (given the likely contribution from contact resistance).

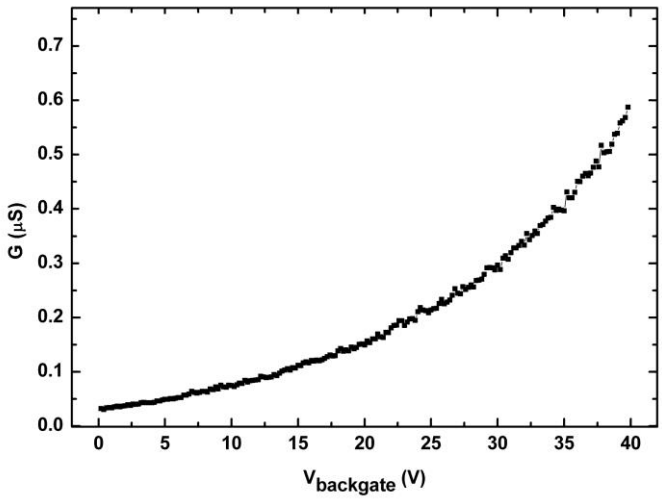

Figure 5.2. Room temperature characterization of the MoS_2 nanoribbon: DC conductance versus backgate voltage taken with a dc bias of 0.5 V.

Figure 5.3a shows the differential conductance versus backgate at 1.7 K: the conductance is strongly suppressed compared to room temperature, and has a threshold voltage at a much more positive value. These observations are consistent with the insulating behavior seen in these materials at low temperature[132]. A large conductance gap is evident for 0 V < $V_{backgate}$ < 40 V and persists to large bias (50 mV), as can be seen in Fig 5.3a. (The gap is also evident in the negative backgate regime, up to – 60 V). However, at backgate voltages above ~ 40 V, the conductance varies strongly with gate and bias: the 2D map of Fig 5.3b shows a gap that rapidly decreases with increasing bias

and backgate voltages. Just above 40 V the gap edges begin to exhibit Coulomb diamond-like features, as can be seen more clearly in the zoomed-in 2D conductance map of Fig 5.3a.

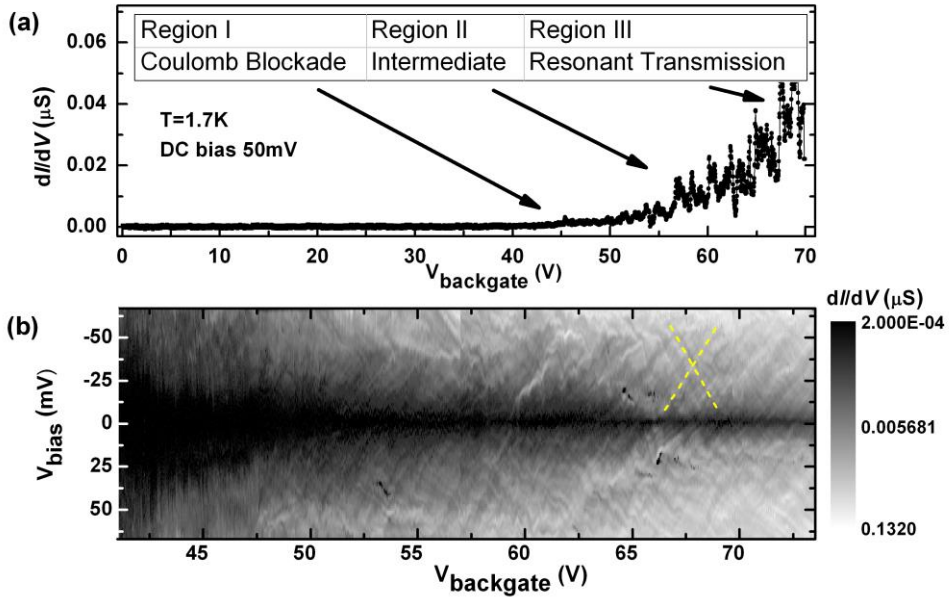

Figure 5.3. Low-temperature transport regimes: (a) Differential conductance versus backgate voltage at 1.7K with a dc bias of 50 mV and an ac excitation of 0.5 mV. (b) Two-dimensional map of differential conductance versus dc bias voltage V_{bias} and backgate voltage $V_{backgate}$, with the side gate floated. Yellow dashed lines are guides to the eye showing the crossed resonance features, used to estimate the backgate efficiency. Note that (a) corresponds a line cut at V_{bias} = 50mV in (b), for a larger backgate range.

The data in Fig 5.3 might initially seem to indicate that the band gap suppresses conductance for gate voltages below ~ 40 V. However, a closer analysis of the data demonstrates that the band gap alone may not be sufficient to account for this large gap, and that Coulomb blockade likely plays a role as well. We find a backgate efficiency $\alpha = \Delta V_{bias} / \Delta V_{backgate} = 0.02$ from the resonant transmission line features marked in yellow in Fig 5.3b (discussed in more detail later in the chapter). This allows us estimate that a gap persisting up to $\Delta V_{backgate} = 100$ V is equivalent to an energy (bias) gap of $\alpha \times \Delta V_{backgate} = 2$ V. However, for bilayer MoS_2 the band gap is only 1.6 eV [140], i.e., smaller than the observed gap. In nanoribbons, the band gap could be even smaller, depending on the edge

configuration[141, 142]. This suggests that the gap in this region can be dominated by other effects, in this case likely Coulomb blockade due to multiple weakly-coupled quantum dots in series.

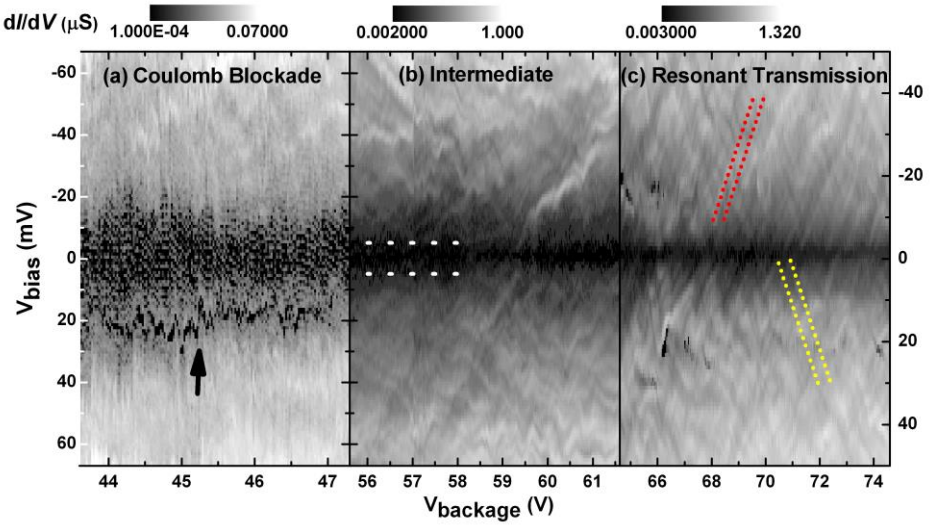

Figure 5.4. Zoom-in of regions transitioning from Coulomb blockade to resonant transmission. Each panel shows a two-dimensional map of differential conductance versus dc bias voltage V_{bias} for different ranges of backgate voltage $V_{backgate}$. (a) Irregular Coulomb blockade diamonds, with black arrow marking edge of a diamond. (b) Coulomb blockade region having approximately constant charging energy ~ 5 meV. White dotted lines mark where V_{bias} ($\pm$ 5 meV) is equivalent to the charging energy of a quantum dot size comparable to the entire ribbon. (c) Resonant transmission region of crossed conductance patterns; typical resonances are marked by yellow and red dotted lines. The spacings between the dotted lines are used to estimate the typical energy spacing between resonant transmission energy levels.

Coulomb blockade is evident in the 2D conductance as irregular diamond patterns that vary with bias and backgate (e.g., Fig 5.4a), where the average size of the diamonds corresponds to an average charging energy. At $V_{backgate}$ ~ 40 V, the charging energy (gap in bias) is ~ 50 meV. From this charging energy, the quantum dot size can be estimated as ~ 18 nm, using $E_{charging} = e^2/(8\varepsilon_0\varepsilon_r r)$, where the relative permittivity $\varepsilon_r = \left(\left(\varepsilon_{Air} + \varepsilon_{SiO_2}\right)/2\right)$ and r is the radius of quantum dot. This gives an upper-bound on the size of the small dots that suppress conductance for $V_{backgate}$ < 40 V. In Fig 5.4b, it can

be seen that as the backgate voltage increases from 40 V to 50 V, the size of the bias gap decreases, indicating that the quantum dot size increases; for example, for $V_{backgate}$ ~ 45 V, Fig 5.4a shows that the average charging energy is ~ 25 meV, corresponding to a dot size of ~ 37 nm. Near $V_{backgate}$ ~ 50 V, the dot size increases to ~ 69 nm. The Coulomb diamonds near $V_{backgate}$ ~ 50 V can be further examined by tuning the sidegate voltage, as can be seen in Fig 5.5. In this case, the charging energy is ~ 13.3 meV, which is consistent with the backgate data. As $V_{backgate}$ increases above 50 V, the charging energy decreases—implying that the size of the quantum dot increases—until it saturates at ~ 5 meV for the backgate range 55 V ~ 66 V, as shown in Fig 5.3b and marked by the white dotted line in Fig 5.4b. In this regime ($V_{backgate}$ > 50 V), the quantum dot size approaches the oxide thickness (300 nm), so the capacitance geometry changes from an isolated disk approximation to a parallel plate approximation, and the charging energy must be calculated by interpolating between $E_{charging}= e^2/(8\varepsilon_0\varepsilon_r r)$ and $E_{charging}= e^2/(C_g \times A)$. This allows us to estimate the quantum dot size in the saturated regime as between 0.106 μm^2 and 0.267 μm^2, which is comparable to the ribbon size (~ 0.1 μm^2), suggesting that at this point the entire ribbon acts a quantum dot. The fact that the charging energy is relatively constant over a large gate range in this regime is also consistent with the dot size being fixed at the device length. This implies that it is possible to have resonant quantum transport across the entire length of the nanoribbon.

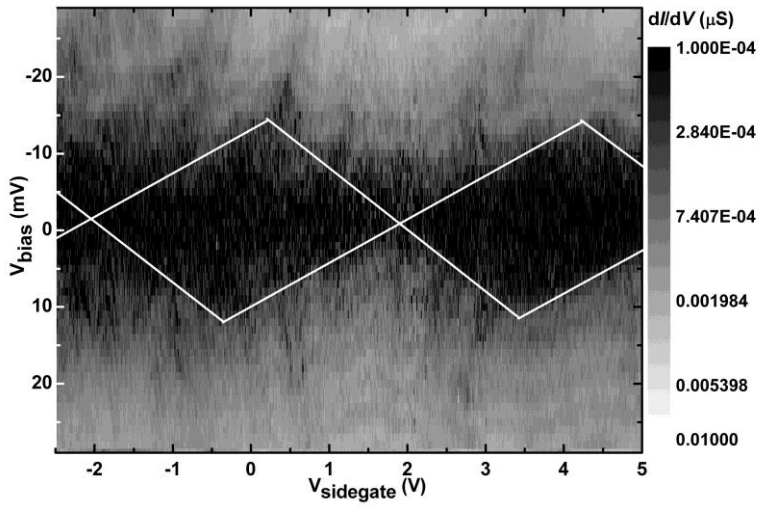

Figure 5.5. Coulomb blockade evident in two-dimensional map of differential conductance versus V_{bias} and sidegate voltage $V_{sidegate}$ with the backgate voltage at $V_{backgate}$ = 50V. The dotted lines outline the diamonds and the dashed line marks the charging energy at 13.3 meV.

The likely cause of the Coulomb blockade is charge impurities[130, 132], which modulate the local conduction band gap position (E_C) to create quantum dots. Figure 5.6 shows a schematic of how tuning the Fermi energy with respect to the underlying impurity potential affects the size of the quantum dots. At low $V_{backgate}$, the Fermi level is sitting deep inside the disorder potential and multiple small quantum dots form. When the Fermi level moves up and out of the potential dips, the quantum dots grow and can extend to the entire nanoribbon area. While resonant tunneling at localized sites have been observed in the larger MoS_2 samples (~a few μm^2)[132], here we see a complete blockade likely due to the geometric confinement of the nanoribbon.

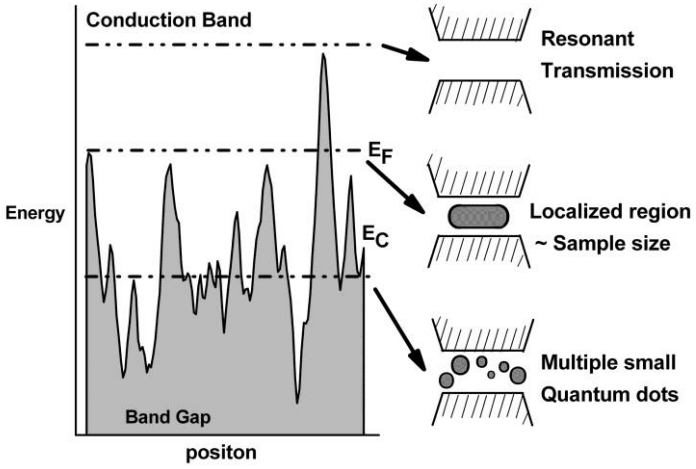

Figure 5.6. Schematic of transition from multiple dots to resonant transmission, showing how the quantum dots change in size as the Fermi level is tuned by the backgate voltage, in the presence of a disorder potential. Solid line denoted by E_C shows a jagged conduction band edge modified by local disorder. The dot-dash lines denoted by E_F indicate the Fermi level. When the Fermi level is deep inside the potential wells, the nanoribbon is broken into multiple small quantum dots; when the Fermi level is just above the potential wells, a quantum dot comparable to the ribbon in size emerges; when the Fermi level is further lifted up, resonant transmission can occur due to the scattering from the potential profiles. backgate voltage at $V_{backgate}$ = 50V. The dotted lines outline the diamonds and the dashed line marks the charging energy at 13.3 meV.

5.4 Resonant transmission

As the backgate voltage is increased above 65 V, crossing line features resembling Fabry-Perot oscillations appear in the 2D conductance map (yellow dashed lines in Fig 5.2b and Fig 5.3c). However, it is not likely that these are due to Fabry-Perot type transport: the conductance is too small ($G_{max} \sim 0.02e^2/h$) and the expected mean free path of ~ 20 nm[143, 144] too short for ballistic transport across the entire nanoribbon. In addition, it can be calculated from the slope of the lines that the resonances do not arise from states inside the conduction band[145]: transport inside the conduction band for a 2D system with a quadratic energy dispersion relationship predicts a slope of α_{band} =

$\Delta V_{bias} / \Delta V_{backgate} = 2C_g/(e^2 \times D) = 4.6e\text{-}4$, where D is the density of states given by $D = gm^*/2\pi\hbar^2$ (we use effective mass $m^* = 0.39m_0$ [140] and degeneracy g = 4). The calculated slope is thus 44 times smaller than the slope extracted from the data of $\alpha = 0.02$. While the actual capacitance could be larger due to charge traps, the density of states of these traps would have to be 100 times larger than what is usually found for the MoS_2-SiO_2 interface[146] to match the data. Similarly, the geometric confinement in the nanoribbon is not likely to change the density of states by a factor of 44.

We argue that the crossing patterns arise from resonant transmission through the disordered potential profiles; for this higher Fermi-level range, the carriers are no longer confined by the quantum dot defined by the nanoribbon size, but are still susceptible to effects of smaller disorder potentials. The disorder-induced single particle energy levels can be inferred from the crossing patterns, and are consistent with the charging energy of the Coulomb blockade in the backgate range 44 V ~ 47 V. The single particle energy levels can be calculated by measuring the distance between two adjacent resonance lines in the backgate range 66 V ~ 74 V (examples are shown in Fig 5.4c, for sets of yellow and red dotted lines). Typical energy spacings are ~ 0.3 meV, 0.6 meV and 0.9 meV. Using $\Delta E \sim \pi\hbar^2/(m^* r^2)$, the energy level spacings correspond to confinement in quantum dots of size 45 nm, 32 nm and 26 nm. These quantum dot sizes are comparable to what we found earlier at $V_{backgate}$ ~ 45 V of ~ 37 nm. We note that the resonant transmission seems to occur through length scales comparable to the predicted mean free path in MoS_2 of ~ 20 nm [143, 144], which is consistent with coherent, ballistic transport occurring at the scale of the mean free path. Resonant transmission through a quantum well can be understood by considering that an incoming particle with energy above the potential well

still undergoes scattering from the well; at certain particle energies, resonant transmission occurs and backscattering will be minimized. Alignment of the energy levels with the source/drain leads potential gives rise to crossing positively/negatively sloped resonance lines. Both Coulomb blockade and resonant transmission are observed in the intermediate regime, as shown in the backgate range 56 V ~ 61 V in Fig 5.4b. Here there are still some regions showing zero conductance at low bias, which come from Coulomb blockade in quantum dot of the ribbon size, while the crossing line features which are the signature of resonant transmission show up at higher bias.

We need to point out that resonant transmission we talk about here is different from the resonant transmission through quantum dot levels, where the resonance refers to when the dot level aligns with the source/drain potential. We also point out that intuitively resonant transmission is not likely to happen as in the ideal case given the complex scattering from the disorder potential.

5.5 Discussion and conclusion

The origin of the disorder may be trapped charges at the MoS_2-substrate interface, as suggested for larger MoS_2 samples[132]. In graphene, trapped molecules at the graphene-substrate interface have been found to be the key factor contributing to charge inhomgeneity[17]. The fact that annealed and vacuum-sealed MoS_2 shows a band like transport (mobility relatively constant with temperature) at low temperature suggests that adsorbents from the ambient could induce significant scattering and should be considered in the picture of disorder as well[147]. Similarly, rough edges may also play a role[67] : results on graphene nanoribbons—such as gaps observed in suspended devices[148] and in those on

hexagonal boron nitride[149]—suggest that rough edges can contribute to conductance gaps observed in nanostructures in two-dimensional materials[150, 151].

In conclusion, we have fabricated a MoS_2 nanoribbon and measured its transport properties at low temperature. We observed a gate-tuned transition from Coulomb blockade to transmission, determining the formation of quantum dots that range in size from < 20 nm to the extent of the entire 500 nm-long nanoribbon as gate voltage is increased. The transition can be understood in terms of an interplay between the gate-tuned Fermi energy and quantum dots created by an underlying disordered potential: as the Fermi level moves up, the barriers that isolated the quantum dots become weaker and allow resonant conduction. Mesoscopic effects and resonant transmission are evident in MoS_2 having a length-scale up to 200 nm, although ballistic transport and well-defined quantum dot behavior—potentially useful for quantum information devices—should be appear in even smaller nanoribbons (< 50 nm width, < 100 nm length). Our findings shed light on the length scales of quasi-ballistic transport and disorder in MoS_2 and can help explain related physics in these two-dimensional semiconductors, improving device performances and enabling further applications.

Chapter 6: Conclusion

First we demonstrated a robust new technique for probing graphene while enabling a greater understanding of the contact between graphene and various materials. We not only demonstrated the fabrication of simple Pb probes, but elucidated the behavior of the contact resistance between graphene and various materials. We then showed that planar tunneling has energy resolution similar to what has been seen via STS, but with much greater configurability (e.g.,ultra-low temperature, high magnetic field, finite gate voltage, insulating substrate). The features we observe—such as scattering resonances, graphene-derived localized states—demonstrate that we are probing the microscopic electronics of graphene.

Next, we used the tunneling spectroscopy technique on graphene nano-constrictions of two different widths. Coulomb blockade and superconducting proximity effect is observed in the transport measurement of both constrictions with different strengths. However, ABS is observed in tunneling measurement of the narrow (10 nm wide) constriction only, which can be attributed to the better coupling between the narrow constriction and the normal leads. This suggests the size of the narrow constriction is smaller than the characteristic length of potential disorder. This finding also stresses the importance of coupling for the observation of ABS.

We then extended the study of nanostructures from graphene to MoS_2. A gate-tunable transition from Coulomb blockade to resonant transmission was observed in a bilayer MoS_2 nanoribbon at low temperature, where the transition point occurs when the

entire nanoribbon acts as a quantum dot. Our work shows the first evidence of Coulomb blockade in MoS_2, the first evidence of coherent quantum transport across the entire nanoribbon, and evidence of resonant-transmission across smaller localized regions. It is advantageous to study small samples (< 200 nm) because the mean free path, phase coherence length and disorder-induced localized regions are on this order and thus the interplay between ballistic transport, phase coherence and disordered are enhanced. The transport properties we show are the tip of the iceberg; future MoS_2 nanoribbons of various lengths and widths should reveal even richer physics and may open the door to applications in quantum devices.

Appendix: Code for the Transport Calculation of Andreev Bound States

A.1 Single quantum dot

```
clear all;
tic
%Example fit tL=1.0;tR=0.095;Uc=24.9;e1down=158.3;!

eta=1e-8;%small eta
GL=1.0;%tunnelling rate at Left lead
GR=1.0;%tunnelling rate at Right lead
sLsR=0;%1 if sc on left and right, 0 if nm on left and sc on right
Ec=0.5;%conduction band edge

%Parameters for Leads
DD=0.0013;%SC order parameter 0.0013 for fit
tL=0.19;%hopping from Left lead to dot 0.19 for fit
tR=0.0215;%hopping from Right lead to dot 0.0215 was the fitting value

%Parameters for quantum Dot
Uc=(1e-3)*(7.7);%was 7.7 for fit
e1down=-(1e-3)*(32.4);%%32.4 was the fitting value
e1up=e1down+Uc;%

GateScale=1/990;% example 1 eV of energy per 990 applied gate volts

%Sweep Parameters
dOm=30;%grid spacing
window=1.6;%omega window in units of DD
omArray=[-window*DD:DD/dOm:window*DD];%array of omegas

VgArray=[-(2.0*6200*DD):400*DD/(dOm):0*2.0*7700*DD];

numOm=length(omArray);
rhoLUp(1:numOm)=0.0;
rhoRUp(1:numOm)=0.0;
rhoLDown(1:numOm)=0.0;
rhoRDown(1:numOm)=0.0;

numVg=length(VgArray);

specUp(1:numVg,1:2)=0.0;
specDown(1:numVg,1:2)=0.0;
trans(1:numVg,1:numOm)=0.0;

VgScale=1.0;
Vshift=17.5;
spec1(1:numVg,1:numOm,1:2)=0.0;
```

```
spec2(1:numVg,1:numOm,1:2)=0.0;
for jj=1:numVg
Vg=VgArray(jj);

hup=[e1up-GateScale*(Vg-Vshift) 0 ; 0 -e1down+GateScale*(Vg-Vshift)];
hdown=[e1down-GateScale*(Vg-Vshift) 0 ; 0 -e1up+GateScale*(Vg-Vshift)];

%hup=[e1up+(1/31.3381)*sqrt(abs(Vg-Vshift)) 0 ; 0 -e1down-(1/31.3381)*sqrt(abs(Vg-Vshift))];
%hdown=[e1down+(1/31.3381)*sqrt(abs(Vg-Vshift)) 0 ; 0 -e1up-(1/31.3381)*sqrt(abs(Vg-Vshift))];

specUp(jj,:)=eig(hup);
specDown(jj,:)=eig(hdown);

for ii=1:numOm

   if sLsR==0
   om=omArray(ii);
   ff=DD/sqrt(DD^2-(om+i*eta)^2);
   gg=-(om+i*eta)*ff/DD;
   sigEEL=(1/20)*(tL^2)*(-i*pi*(abs(sqrt(om^2+1.2*0.0005^2))));%*(-i*pi/100);
   sigHHL=(1/20)*(tL^2)*(-i*pi*abs(sqrt(om^2+1.2*0.0005^2)));%*(-i*pi/100);
   sigEER=(tR^2)*gg;
   sigEHL=0;
   sigEHR=-(tR^2)*ff;
   DelEff(jj,ii)=sigEHR;

   sigL=[sigEEL sigEHL; sigEHL sigHHL];
   sigR=[sigEER sigEHR; sigEHR sigEER];
   gUp=inv((om+i*eta)*eye(2,2)-hup-sigL-sigR);
   gDown=inv((om+i*eta)*eye(2,2)-hdown-sigL-sigR);
   rhoLUp(ii)=(-1/pi)*imag(gUp(1,1)+gUp(2,2));
   rhoLDown(ii)=(-1/pi)*imag(gDown(1,1)+gDown(2,2));
   rhoRUp(ii)=0;
   rhoRDown(ii)=0;
   %H1mod=hup+real(sigL+sigR);
   %H2mod=hdown+real(sigL+sigR);
   %spec1(jj,ii,:)=eig(H1mod);
   %spec2(jj,ii,:)=eig(H2mod);
   else
   om=omArray(ii);
   ff=DD/sqrt(DD^2-(om+i*eta)^2);
   gg=-(om+i*eta)*ff/DD;
   sigEEL=(tL^2)*gg;
   sigEER=(tR^2)*gg;
   sigEHL=-(tL^2)*ff;
   sigEHR=-(tR^2)*ff;

   sigL=[sigEEL sigEHL; sigEHL sigEEL];
   sigR=[sigEER sigEHR; sigEHR sigEER];
   gUp=inv(om*eye(2,2)-hup-sigL-sigR);
   gDown=inv(om*eye(2,2)-hdown-sigL-sigR);
   rhoLUp(ii)=(-1/pi)*imag(gUp(1,1)+gUp(2,2));
   rhoLDown(ii)=(-1/pi)*imag(gDown(1,1)+gDown(2,2));
   rhoRUp(ii)=0;
```

```
    rhoRDown(ii)=0;

    end

end
trans(jj,:)=GL*(rhoLUp+rhoLDown)+GR*(rhoRUp+rhoRDown);
end

toc

figure;
pcolor(VgArray,omArray,-log(trans)');shading interp;
```

A.2 Multiple (Three) quantum dots

```
clear all;
tic
%Example fit tL=1.0;tR=0.095;Uc=24.9;e1down=158.3;!

%Parameters you probably wont have to adjust

eta=1e-8;%small eta
GL=1.0;%tunnelling rate at Left lead
GR=1.0;%tunnelling rate at Right lead
sLsR=0;%1 if sc on left and right, 0 if nm on left and sc on right
Ec=0.5;%conduction band edge

%Parameters for Leads
DD=0.0013;%SC order parameter 0.0013 for fit

%Now let's consider the parameters for multiple dots
Num_QD=3;
tt(1:Num_QD,1:Num_QD)=0.0;
tL(1:Num_QD)=0.19;
tR(1:Num_QD)=0.0215;

%tL=0.19;%hopping from Left lead to dot 0.19 for fit
%tR=0.0215;%hopping from Right lead to dot 0.0215 was the fitting value

%Parameters for quantum Dot
Uc(1:Num_QD)=[(1e-3)*(1.0) (1e-3)*(0.5) (1e-3)*(1.0)];%was 7.7 for fit
e1down(1:Num_QD)=[-(1e-3)*(10.4) -(1e-3)*(10.4) -(1e-3)*(10.4)];%32.4 was the fitting value
e1up(1:Num_QD)=e1down+Uc;%
tt(1,2)=1.0e-3;
tt(2,1)=1.0e-3;
tt(1,3)=1.0*1e-3;
tt(3,1)=1.0*1e-3;
tt(2,3)=0.0*1e-3;
tt(3,2)=0.0*1e-3;

GateScale=1/7500;% example 1 eV of energy per 990 applied gate volts
```

```
%Sweep Parameters
dOm=30;%grid spacing
window=1.6;%omega window in units of DD
omArray=[-window*DD:DD/dOm:window*DD];%array of omegas

VgArray=[-(2.0*30000*DD):400*DD/(dOm):0*2.0*7700*DD];

numOm=length(omArray);
rhoLUp(1:numOm)=0.0;
rhoRUp(1:numOm)=0.0;
rhoLDown(1:numOm)=0.0;
rhoRDown(1:numOm)=0.0;

numVg=length(VgArray);

specUp(1:numVg,1:2*Num_QD)=0.0;
specDown(1:numVg,1:2*Num_QD)=0.0;
trans(1:numVg,1:numOm)=0.0;

VgScale=1.0;
Vshift=17.5;
spec1(1:numVg,1:numOm,1:2*Num_QD)=0.0;
spec2(1:numVg,1:numOm,1:2*Num_QD)=0.0;

for qq=1:Num_QD
   for pp=1:Num_QD
hup((qq-1)*2+1:(qq-1)*2+2,(pp-1)*2+1:(pp-1)*2+2)=[tt(qq,pp) 0;0 -tt(qq,pp)];
hdown((qq-1)*2+1:(qq-1)*2+2,(pp-1)*2+1:(pp-1)*2+2)=[tt(qq,pp) 0;0 -tt(qq,pp)];

hup((pp-1)*2+1:(pp-1)*2+2,(qq-1)*2+1:(qq-1)*2+2)=[tt(qq,pp) 0;0 -tt(qq,pp)];
hdown((pp-1)*2+1:(pp-1)*2+2,(qq-1)*2+1:(qq-1)*2+2)=[tt(qq,pp) 0;0 -tt(qq,pp)];
end
end

for jj=1:numVg
Vg=VgArray(jj);

for qq=1:Num_QD
hup((qq-1)*2+1:(qq-1)*2+2,(qq-1)*2+1:(qq-1)*2+2)=[e1up(qq)-GateScale*(Vg-Vshift)     0     ;     0     -
e1down(qq)+GateScale*(Vg-Vshift)];
hdown((qq-1)*2+1:(qq-1)*2+2,(qq-1)*2+1:(qq-1)*2+2)=[e1down(qq)-GateScale*(Vg-Vshift)   0   ;   0   -
e1up(qq)+GateScale*(Vg-Vshift)];
end
%hup=[e1up+(1/31.3381)*sqrt(abs(Vg-Vshift)) 0 ; 0 -e1down-(1/31.3381)*sqrt(abs(Vg-Vshift))];
%hdown=[e1down+(1/31.3381)*sqrt(abs(Vg-Vshift)) 0 ; 0 -e1up-(1/31.3381)*sqrt(abs(Vg-Vshift))];

specUp(jj,:)=eig(hup);
specDown(jj,:)=eig(hdown);

for ii=1:numOm
```

```
    om=omArray(ii);
    ff=DD/sqrt(DD^2-(om+i*eta)^2);
    gg=-(om+i*eta)*ff/DD;
    sigEEL=(1/20)*(tL(1)^2)*(-i*pi*(abs(sqrt(om^2+1.2*0.0005^2))));%*(-i*pi/100);
    sigHHL=(1/20)*(tL(1)^2)*(-i*pi*abs(sqrt(om^2+1.2*0.0005^2)));%*(-i*pi/100);
    sigEER=(tR(1)^2)*gg;
    sigEHL=0;
    sigEHR=-(tR(1)^2)*ff;
    DelEff(jj,ii)=sigEHR;

    sigL=[sigEEL sigEHL; sigEHL sigHHL];
    sigR=[sigEER sigEHR; sigEHR sigEER];
    for qq=1:Num_QD
      BigSigL((qq-1)*2+1:(qq-1)*2+2,(qq-1)*2+1:(qq-1)*2+2)=sigL;
      BigSigR((qq-1)*2+1:(qq-1)*2+2,(qq-1)*2+1:(qq-1)*2+2)=sigR;
    end

    gUp=inv((om+i*eta)*eye(2*Num_QD,2*Num_QD)-hup-BigSigL-BigSigR);
    gDown=inv((om+i*eta)*eye(2*Num_QD,2*Num_QD)-hdown-BigSigL-BigSigR);
    rhoLUp(ii)=(-1/pi)*imag(trace(gUp));
    rhoLDown(ii)=(-1/pi)*imag(trace(gDown));
    rhoRUp(ii)=0;
    rhoRDown(ii)=0;
    %H1mod=hup+real(sigL+sigR);
    %H2mod=hdown+real(sigL+sigR);
    %spec1(jj,ii,:)=eig(H1mod);
    %spec2(jj,ii,:)=eig(H2mod);


end
trans(jj,:)=GL*(rhoLUp+rhoLDown)+GR*(rhoRUp+rhoRDown);
end

toc

figure;
pcolor(VgArray,omArray,-log(trans)');shading interp;
```

Reference

1. Geim, A. K.; Novoselov, K. S. *Nat Mater* **2007,** 6, (3), 183-191.
2. Novoselov, K. S.; Geim, A. K.; Morozov, S. V.; Jiang, D.; Zhang, Y.; Dubonos, S. V.; Grigorieva, I. V.; Firsov, A. A. *Science* **2004,** 306, (5696), 666-669.
3. Castro Neto, A. H.; Guinea, F.; Peres, N. M. R.; Novoselov, K. S.; Geim, A. K. *Reviews of Modern Physics* **2009,** 81, (1), 109-162.
4. Das Sarma, S.; Adam, S.; Hwang, E. H.; Rossi, E. *Reviews of Modern Physics* **2011,** 83, (2), 407-470.
5. Beenakker, C. W. J. *Reviews of Modern Physics* **2008,** 80, (4), 1337-1354.
6. Ponomarenko, L. A.; Schedin, F.; Katsnelson, M. I.; Yang, R.; Hill, E. W.; Novoselov, K. S.; Geim, A. K. *Science* **2008,** 320, (5874), 356-358.
7. Jung, S.; Rutter, G. M.; Klimov, N. N.; Newell, D. B.; Calizo, I.; Hight-Walker, A. R.; Zhitenev, N. B.; Stroscio, J. A. *Nat Phys* **2011,** 7, (3), 245-251.
8. Wolf, E. L., *Principles of Electron Tunneling Spectroscopy*. Second Edition ed.; Oxford University Press: New York, 1985.
9. Greene, L. H. Planar Tunneling and Andreev Reflection: Powerful probes of the superconducting order parameter. http://www.icmr.ucsb.edu/programs/documents/Greene1.pdf http://www.icmr.ucsb.edu/programs/documents/Greene2.pdf
10. Tinkham, M., *Introduction to Superconductivity*. 2004.
11. Martin, J.; Akerman, N.; Ulbricht, G.; Lohmann, T.; Smet, J. H.; von Klitzing, K.; Yacoby, A. *Nat Phys* **2008,** 4, (2), 144-148.
12. Zhang, Y.; Brar, V. W.; Girit, C.; Zettl, A.; Crommie, M. F. *Nat Phys* **2009,** 5, (10), 722-726.
13. Tao, C.; Jiao, L.; Yazyev, O. V.; Chen, Y.-C.; Feng, J.; Zhang, X.; Capaz, R. B.; Tour, J. M.; Zettl, A.; Louie, S. G.; Dai, H.; Crommie, M. F. *Nat Phys* **2011,** 7, (8), 616-620.
14. Kobayashi, Y.; Fukui, K.-i.; Enoki, T.; Kusakabe, K. *Physical Review B* **2006,** 73, (12), 125415.
15. Zhang, Y.; Brar, V. W.; Wang, F.; Girit, C.; Yayon, Y.; Panlasigui, M.; Zettl, A.; Crommie, M. F. *Nat Phys* **2008,** 4, (8), 627-630.
16. Morgenstern, M. *physica status solidi (b)* **2011,** 248, (11), 2423-2434.
17. Zhang, Y.; Brar, V. W.; Girit, C.; Zettl, A.; Crommie, M. F. *Nature Physics* **2009,** 5, (10), 722-726.
18. Deshpande, A.; Bao, W.; Miao, F.; Lau, C. N.; LeRoy, B. J. *Physical Review B* **2009,** 79, (20), 205411.
19. Dean, C. R.; Young, A. F.; MericI; LeeC; WangL; SorgenfreiS; WatanabeK; TaniguchiT; KimP; Shepard, K. L.; HoneJ. *Nat Nano* **2010,** 5, (10), 722-726.
20. Song, Y. J.; Otte, A. F.; Kuk, Y.; Hu, Y.; Torrance, D. B.; First, P. N.; de Heer, W. A.; Min, H.; Adam, S.; Stiles, M. D.; MacDonald, A. H.; Stroscio, J. A. *Nature* **2010,** 467, (7312), 185-189.
21. Miller, D. L.; Kubista, K. D.; Rutter, G. M.; Ruan, M.; de Heer, W. A.; First, P. N.; Stroscio, J. A. *Science* **2009,** 324, (5929), 924-927.
22. Li, G.; Luican, A.; Andrei, E. Y. *Physical Review Letters* **2009,** 102, (17), 176804.

23. Luican, A.; Li, G.; Andrei, E. Y. *Physical Review B* **2011,** 83, (4), 041405.
24. Novoselov, K. S.; Geim, A. K.; Morozov, S. V.; Jiang, D.; Katsnelson, M. I.; Grigorieva, I. V.; Dubonos, S. V.; Firsov, A. A. *Nature* **2005,** 438, (7065), 197-200.
25. Zhang, Y.; Tan, Y.-W.; Stormer, H. L.; Kim, P. *Nature* **2005,** 438, (7065), 201-204.
26. Novoselov, K. S.; McCann, E.; Morozov, S. V.; Fal'ko, V. I.; Katsnelson, M. I.; Zeitler, U.; Jiang, D.; Schedin, F.; Geim, A. K. *Nat Phys* **2006,** 2, (3), 177-180.
27. Gusynin, V. P.; Sharapov, S. G. *Physical Review Letters* **2005,** 95, (14), 146801.
28. Li, G.; Andrei, E. Y. *Nat Phys* **2007,** 3, (9), 623-627.
29. Berger, C.; Song, Z.; Li, X.; Wu, X.; Brown, N.; Naud, C.; Mayou, D.; Li, T.; Hass, J.; Marchenkov, A. N.; Conrad, E. H.; First, P. N.; de Heer, W. A. *Science* **2006,** 312, (5777), 1191-1196.
30. Malec, C. E.; DavidoviÄ‡, D. *Physical Review B* **2011,** 84, (12), 121408.
31. Heersche, H. B.; Jarillo-Herrero, P.; Oostinga, J. B.; Vandersypen, L. M. K.; Morpurgo, A. F. *Nature* **2007,** 446, (7131), 56-59.
32. Dirks, T.; Hughes, T. L.; Lal, S.; Uchoa, B.; Chen, Y.-F.; Chialvo, C.; Goldbart, P. M.; Mason, N. *Nat Phys* **2011,** 7, (5), 386-390.
33. Stampfer, C.; Schurtenberger, E.; Molitor, F.; Güttinger, J.; Ihn, T.; Ensslin, K. *Nano Letters* **2008,** 8, (8), 2378-2383.
34. van den Brink, J. *Nat Nano* **2007,** 2, (4), 199-201.
35. Zazunov, A.; Shumeiko, V. S.; Wendin, G.; Bratus', E. N. *Physical Review B* **2005,** 71, (21), 214505.
36. Zazunov, A.; Shumeiko, V. S.; Bratus', E. N.; Lantz, J.; Wendin, G. *Physical Review Letters* **2003,** 90, (8), 087003.
37. Andreev, A. F. *JETP* **1964,** 20, (6), 1490.
38. Deutscher, G. *Reviews of Modern Physics* **2005,** 77, (1), 109-135.
39. Blonder, G. E.; Tinkham, M.; Klapwijk, T. M. *Physical Review B* **1982,** 25, (7), 4515-4532.
40. Beenakker, C. W. J. *Physical Review Letters* **2006,** 97, (6), 067007.
41. Beenakker, C. W. J. In *Transport Phenomena in Mesoscopic Systems*, 1992; Fukuyama, H.; Ando, T., Eds. Springer.
42. Meng, T.; Florens, S.; Simon, P. *Physical Review B* **2009,** 79, (22), 224521.
43. Du, X.; Skachko, I.; Andrei, E. Y. *Physical Review B* **2008,** 77, (18), 184507.
44. Borzenets, I. V.; Coskun, U. C.; Jones, S. J.; Finkelstein, G. *Physical Review Letters* **2011,** 107, (13), 137005.
45. Mizuno, N.; Nielsen, B.; Du, X. *Nat Commun* **2013,** 4.
46. Buitelaar, M. R.; Nussbaumer, T.; SchÃ¶nenberger, C. *Physical Review Letters* **2002,** 89, (25), 256801.
47. Eichler, A.; Weiss, M.; Oberholzer, S.; Schönenberger, C.; Levy Yeyati, A.; Cuevas, J. C.; Martín-Rodero, A. *Physical Review Letters* **2007,** 99, (12), 126602.
48. Sand-Jespersen, T.; Paaske, J.; Andersen, B. M.; Grove-Rasmussen, K.; Jørgensen, H. I.; Aagesen, M.; Sørensen, C. B.; Lindelof, P. E.; Flensberg, K.; Nygård, J. *Physical Review Letters* **2007,** 99, (12), 126603.
49. Doh, Y.-J.; Franceschi, S. D.; Bakkers, E. P. A. M.; Kouwenhoven, L. P. *Nano Letters* **2008,** 8, (12), 4098-4102.

50. Deacon, R. S.; Tanaka, Y.; Oiwa, A.; Sakano, R.; Yoshida, K.; Shibata, K.; Hirakawa, K.; Tarucha, S. *Physical Review Letters* **2010,** 104, (7), 076805.
51. Li, X.; Wang, X.; Zhang, L.; Lee, S.; Dai, H. *Science* **2008,** 319, (5867), 1229-1232.
52. Ritter, K. A.; Lyding, J. W. *Nat Mater* **2009,** 8, (3), 235-242.
53. Stampfer, C.; Güttinger, J.; Molitor, F.; Graf, D.; Ihn, T.; Ensslin, K. *Applied Physics Letters* **2008,** 92, (1), -.
54. Schnez, S.; Molitor, F.; Stampfer, C.; Güttinger, J.; Shorubalko, I.; Ihn, T.; Ensslin, K. *Applied Physics Letters* **2009,** 94, (1), -.
55. Güttinger, J.; Stampfer, C.; Hellmüller, S.; Molitor, F.; Ihn, T.; Ensslin, K. *Applied Physics Letters* **2008,** 93, (21), -.
56. Güttinger, J.; Stampfer, C.; Libisch, F.; Frey, T.; Burgdörfer, J.; Ihn, T.; Ensslin, K. *Physical Review Letters* **2009,** 103, (4), 046810.
57. Todd, K.; Chou, H.-T.; Amasha, S.; Goldhaber-Gordon, D. *Nano Letters* **2008,** 9, (1), 416-421.
58. Stampfer, C.; Güttinger, J.; Hellmüller, S.; Molitor, F.; Ensslin, K.; Ihn, T. *Physical Review Letters* **2009,** 102, (5), 056403.
59. Elzerman, J. M.; Hanson, R.; Willems van Beveren, L. H.; Witkamp, B.; Vandersypen, L. M. K.; Kouwenhoven, L. P. *Nature* **2004,** 430, (6998), 431-435.
60. Petta, J. R.; Johnson, A. C.; Taylor, J. M.; Laird, E. A.; Yacoby, A.; Lukin, M. D.; Marcus, C. M.; Hanson, M. P.; Gossard, A. C. *Science* **2005,** 309, (5744), 2180-2184.
61. Trauzettel, B.; Bulaev, D. V.; Loss, D.; Burkard, G. *Nat Phys* **2007,** 3, (3), 192-196.
62. Liang, W.; Bockrath, M.; Bozovic, D.; Hafner, J. H.; Tinkham, M.; Park, H. *Nature* **2001,** 411, (6838), 665-669.
63. Jarillo-Herrero, P.; Sapmaz, S.; Dekker, C.; Kouwenhoven, L. P.; van der Zant, H. S. J. *Nature* **2004,** 429, (6990), 389-392.
64. Cobden, D. H.; Nygård, J. *Physical Review Letters* **2002,** 89, (4), 046803.
65. Son, Y.-W.; Cohen, M. L.; Louie, S. G. *Physical Review Letters* **2006,** 97, (21), 216803.
66. Han, M. Y.; Özyilmaz, B.; Zhang, Y.; Kim, P. *Physical Review Letters* **2007,** 98, (20), 206805.
67. Han, M. Y.; Brant, J. C.; Kim, P. *Physical Review Letters* **2010,** 104, (5), 056801.
68. Güttinger, J.; Molitor, F.; Stampfer, C.; Schnez, S.; Jacobsen, A.; Dröscher, S.; Ihn, T.; Ensslin, K. *Rep. Prog. Phys.* **2012,** 75, (12), 126502.
69. Martin, I.; Blanter, Y. M. *Physical Review B* **2009,** 79, (23), 235132.
70. Gallagher, P.; Todd, K.; Goldhaber-Gordon, D. *Physical Review B* **2010,** 81, (11), 115409.
71. Cheiwchanchamnangij, T.; Lambrecht, W. R. L. *Physical Review B* **2012,** 85, (20), 205302.
72. RadisavljevicB; RadenovicA; BrivioJ; GiacomettiV; KisA. *Nat Nano* **2011,** 6, (3), 147-150.
73. Lu, W.; Lieber, C. M. *Nat Mater* **2007,** 6, (11), 841-850.
74. Sundaram, R. S.; Engel, M.; Lombardo, A.; Krupke, R.; Ferrari, A. C.; Avouris, P.; Steiner, M. *Nano Letters* **2013,** 13, (4), 1416-1421.

75. Sebenik, R. F.; Burkin, A. R.; Dorfler, R. R.; Laferty, J. M.; Leichtfried, G.; Meyer-Grünow, H.; Mitchell, P. C. H.; Vukasovich, M. S.; Church, D. A.; Van Riper, G. G.; Gilliland, J. C.; Thielke, S. A., Molybdenum and Molybdenum Compounds. In *Ullmann's Encyclopedia of Industrial Chemistry*, Wiley-VCH Verlag GmbH & Co. KGaA: 2000.
76. Wang, Q. H.; Kalantar-Zadeh, K.; Kis, A.; Coleman, J. N.; Strano, M. S. *Nat Nano* **2012,** 7, (11), 699-712.
77. Splendiani, A.; Sun, L.; Zhang, Y.; Li, T.; Kim, J.; Chim, C.-Y.; Galli, G.; Wang, F. *Nano Letters* **2010,** 10, (4), 1271-1275.
78. Radisavljevic, B.; Radenovic, a.; Brivio, J.; Giacometti, V.; Kis, a. *Nature Nanotechnology* **2011,** 6, 147-50.
79. Mak, K. F.; He, K.; Shan, J.; Heinz, T. F. *Nat Nano* **2012,** 7, (8), 494-498.
80. Andrei, E. Y.; Li, G.; Du, X. *Reports on Progress in Physics* **2012,** 75, (5), 056501.
81. Amet, F.; Williams, J. R.; Garcia, A. G. F.; Yankowitz, M.; Watanabe, K.; Taniguchi, T.; Goldhaber-Gordon, D. *Physical Review B* **2012,** 85, (7), 073405.
82. Staley, N.; Wang, H.; Puls, C.; Forster, J.; Jackson, T. N.; McCarthy, K.; Clouser, B.; Liu, Y. *Applied Physics Letters* **2007,** 90, (14), 143518.
83. Zeng, C.; Wang, M.; Zhou, Y.; Lang, M.; Lian, B.; Song, E.; Xu, G.; Tang, J.; Torres, C.; Wang, K. L. *Applied Physics Letters* **2010,** 97, (3), 032104.
84. Vora, H.; Kumaravadivel, P.; Nielsen, B.; Du, X. *Applied Physics Letters* 100, (15), 153507-5.
85. Chen, Y.-F.; Dirks, T.; Al-Zoubi, G.; Birge, N. O.; Mason, N. *Physical Review Letters* **2009,** 102, (3), 036804.
86. Valles, J. M., Jr.; Dynes, R. C.; Cucolo, A. M.; Gurvitch, M.; Schneemeyer, L. F.; Garno, J. P.; Waszczak, J. V. *Physical Review B* **1991,** 44, (21), 11986-11996.
87. Greene, L. H.; Covington, M.; Aprili, M.; Badica, E.; Pugel, D. E. *Physica B: Condensed Matter* **2000,** 280, (1â€“4), 159-164.
88. Lee, B.; Park, S.-Y.; Kim, H.-C.; Cho, K.; Vogel, E. M.; Kim, M. J.; Wallace, R. M.; Kim, J. *Applied Physics Letters* **2008,** 92, (20), 203102.
89. Wang, X.; Tabakman, S. M.; Dai, H. *Journal of the American Chemical Society* **2008,** 130, (26), 8152-8153.
90. Wang, L.; Travis, J. J.; Cavanagh, A. S.; Liu, X.; Koenig, S. P.; Huang, P. Y.; George, S. M.; Bunch, J. S. *Nano letters* **2012,** 12, (7), 3706-3710.
91. Malec, C. E.; Davidović, D. *Journal of Applied Physics* **2011,** 109, (6), 064507.
92. Malec, C. E.; Davidović, D. *Physical Review B* **2011,** 84, (12), 121408.
93. Li, S.-L.; Miyazaki, H.; Kumatani, A.; Kanda, A.; Tsukagoshi, K. *Nano letters* **2010,** 10, (7), 2357-2362.
94. Du, X.; Skachko, I.; Barker, A.; Andrei, E. Y. *Nat. Nanotechnol.* **2008,** 3, (8), 491-495.
95. Bolotin, K. I.; Sikes, K. J.; Jiang, Z.; Klima, M.; Fudenberg, G.; Hone, J.; Kim, P.; Stormer, H. L. *Solid State Communications* **2008,** 146, (9-10), 351-355.
96. Peeters, F.; Slavin, A. J. *Surface Science* **1989,** 214, (1â€“2), 85-96.
97. Tinkham, M., *Introduction to Superconductivity*. 2nd ed.; McGraw-Hill Book Co.: New York, 1996.

98. Güttinger, J.; Stampfer, C.; Frey, T.; Ihn, T.; Ensslin, K. *physica status solidi (b)* **2009,** 246, (11-12), 2553-2557.
99. Güttinger, J.; Stampfer, C.; Frey, T.; Ihn, T.; Ensslin, K. *Nanoscale Research Letters C7 - 253* **2011,** 6, (1), 1-6.
100. Bolotin, K. I.; Sikes, K. J.; Jiang, Z.; Klima, M.; Fudenberg, G.; Hone, J.; Kim, P.; Stormer, H. L. *Solid State Communications* **2008,** 146, (9–10), 351-355.
101. Du, X.; Skachko, I.; Barker, A.; Andrei, E. Y. *Nat Nano* **2008,** 3, (8), 491-495.
102. Rowell, J. M.; McMillan, W. L. *Physical Review Letters* **1966,** 16, (11), 453-456.
103. Nesher, O.; Koren, G. *Physical Review B* **1999,** 60, (13), 9287-9290.
104. Efros, A. L. *Solid State Communications* **1988,** 67, (11), 1019-1022.
105. Dial, O. E.; Ashoori, R. C.; Pfeiffer, L. N.; West, K. W. *Nature* **2007,** 448, (7150), 176-179.
106. Dial, O. E.; Ashoori, R. C.; Pfeiffer, L. N.; West, K. W. *Nature* **2010,** 464, (7288), 566-570.
107. Sadowski, M. L.; Martinez, G.; Potemski, M.; Berger, C.; de Heer, W. A. *Physical Review Letters* **2006,** 97, (26), 266405.
108. Zhang, Y.; Jiang, Z.; Small, J. P.; Purewal, M. S.; Tan, Y. W.; Fazlollahi, M.; Chudow, J. D.; Jaszczak, J. A.; Stormer, H. L.; Kim, P. *Physical Review Letters* **2006,** 96, (13), 136806.
109. Taychatanapat, T.; Watanabe, K.; Taniguchi, T.; Jarillo-Herrero, P. *Nat Phys* **2011,** 7, (8), 621-625.
110. Libisch, F.; Rotter, S.; Güttinger, J.; Stampfer, C.; Burgdörfer, J. *Physical Review B* **2010,** 81, (24), 245411.
111. Rutter, G. M.; Crain, J. N.; Guisinger, N. P.; Li, T.; First, P. N.; Stroscio, J. A. *Science* **2007,** 317, (5835), 219-222.
112. Pillet, J. D.; Quay, C. H. L.; Morfin, P.; Bena, C.; Yeyati, A. L.; Joyez, P. *Nat Phys* **2010,** 6, (12), 965-969.
113. Dirks, T.; Chen, Y.-F.; Birge, N. O.; Mason, N. *Applied Physics Letters* **2009,** 95, 192103.
114. Franke, K. J.; Schulze, G.; Pascual, J. I. *Science* **2011,** 332, (6032), 940-944.
115. Buizert, C.; Oiwa, A.; Shibata, K.; Hirakawa, K.; Tarucha, S. *Physical Review Letters* **2007,** 99, (13), 136806.
116. Kanai, Y.; Deacon, R. S.; Oiwa, A.; Yoshida, K.; Shibata, K.; Hirakawa, K.; Tarucha, S. *Physical Review B* 82, (5), 054512.
117. van Dam, J. A.; Nazarov, Y. V.; Bakkers, E. P. A. M.; De Franceschi, S.; Kouwenhoven, L. P. *Nature* **2006,** 442, (7103), 667-670.
118. Cleuziou, J. P.; WernsdorferW; BouchiatV; OndarcuhuT; MonthiouxM. *Nat Nano* **2006,** 1, (1), 53-59.
119. Stampfer, C.; Schurtenberger, E.; Molitor, F.; Ihn, T.; Ensslin, K.; Transistors, S. E.; Dots, Q. **2009,** 23, 2647-2654.
120. Li, Y.; Mason, N. *Applied Physics Letters* 102, (2), -.
121. Han, M. Y.; Brant, J. C.; Kim, P. *Physical Review Letters* **2010,** 104, 056801.
122. Stampfer, C.; Güttinger, J.; Hellmüller, S.; Molitor, F.; Ensslin, K.; Ihn, T. *Physical Review Letters* **2009,** 102, 056403.
123. Martin, I.; Blanter, Y. *Physical Review B* **2009,** 79, 235132.

124. Terrés, B.; Dauber, J.; Volk, C.; Trellenkamp, S.; Wichmann, U.; Stampfer, C. *Applied Physics Letters* **2011,** 98, 032109.
125. Todd, K.; Chou, H.-T.; Amasha, S.; Goldhaber-Gordon, D. *Nano letters* **2009,** 9, 416-21.
126. Volk, C.; Fringes, S.; Terrés, B.; Dauber, J.; Engels, S.; Trellenkamp, S.; Stampfer, C. *Nano letters* **2011,** 11, 3581-6.
127. Wang, Q. H.; Kalantar-Zadeh, K.; Kis, A.; Coleman, J. N.; Strano, M. S. *Nature Nanotechnology* **2012,** 7, 699-712.
128. Huang, X.; Zeng, Z.; Zhang, H. *Chemical Society Reviews* **2013,** 42, 1934-46.
129. Loss, D.; DiVincenzo, D. P. *Physical Review A* **1998,** 57, (1), 120-126.
130. Gallagher, P.; Todd, K.; Goldhaber-Gordon, D. *Physical Review B* **2010,** 81, 115409.
131. Dolui, K.; Pemmaraju, C. D.; Sanvito, S. *ACS Nano* **2012,** 6, (6), 4823-4834.
132. Ghatak, S.; Pal, A. N.; Ghosh, A. *ACS Nano* **2011,** 5, (10), 7707-7712.
133. Huang, Y.; Wu, J.; Xu, X.; Ho, Y.; Ni, G.; Zou, Q.; Koon, G.; Zhao, W.; Castro Neto, A. H.; Eda, G.; Shen, C.; Özyilmaz, B. *Nano Research* 6, (3), 200-207.
134. Wu, J.; Li, H.; Yin, Z.; Li, H.; Liu, J.; Cao, X.; Zhang, Q.; Zhang, H. *Small* 9, (19), 3314-3319.
135. Liu, H.; Jiangjiang, G.; Ye, P. D. *Electron Device Letters, IEEE* **2012,** 33, (9), 1273-1275.
136. Ayari, A.; Cobas, E.; Ogundadegbe, O.; Fuhrer, M. S. *Journal of Applied Physics* **2007,** 101, 014507.
137. Late, D. J.; Liu, B.; Matte, H. S. S. R.; Dravid, V. P.; Rao, C. N. R. *ACS Nano* **2012,** 6, (6), 5635-5641.
138. Pradhan, N. R.; Rhodes, D.; Zhang, Q.; Talapatra, S.; Terrones, M.; Ajayan, P. M.; Balicas, L. *Applied Physics Letters* **2013,** 102, 123105.
139. Baugher, B. W. H.; Churchill, H. O. H.; Yang, Y.; Jarillo-Herrero, P. *Nano letters* **2013,** 13, 4212-6.
140. Cheiwchanchamnangij, T.; Lambrecht, W. R. L. *Physical Review B* **2012,** 85, 205302.
141. Erdogan, E.; Popov, I. H.; Enyashin, a. N.; Seifert, G. *The European Physical Journal B* **2012,** 85, 33.
142. Pan, H.; Zhang, Y.-W. *Journal of Materials Chemistry* **2012,** 22, 7280.
143. Ganapathi, K.; Yoon, Y.; Salahuddin, S. *69th Device Research Conference* **2011,** 6, 79-80.
144. Sengupta, A.; Mahapatra, S. *Journal of Applied Physics* **2013,** 113, 194502.
145. Cho, S.; Fuhrer, M. *Nano Research* **2011,** 4, 385-392.
146. Na, J.; Joo, M.-K.; Shin, M.; Huh, J.; Kim, J.-S.; Piao, M.; Jin, J.-E.; Jang, H.-K.; Choi, H. J.; Shim, J. H.; Kim, G.-T. *Nanoscale* **2013**.
147. Jariwala, D.; Sangwan, V. K.; Late, D. J.; Johns, J. E.; Dravid, V. P.; Marks, T. J.; Lauhon, L. J.; Hersam, M. C. *Applied Physics Letters* **2013,** 102, 173107.
148. Ki, D.-K.; Morpurgo, A. F. *Physical Review Letters* **2012,** 108, (26), 266601.
149. Bischoff, D.; Krahenmann, T.; Droscher, S.; Gruner, M. A.; Barraud, C.; Ihn, T.; Ensslin, K. *Applied Physics Letters* **2012,** 101, (20), 203103-4.
150. Evaldsson, M.; Zozoulenko, I.; Xu, H.; Heinzel, T. *Physical Review B* **2008,** 78, 161407.

151. Xu, H.; Heinzel, T.; Zozoulenko, I. *Physical Review B* **2009,** 80, 045308.